

Polydisperse Colloid Transport in Fractured Media

by

Scott C. James

A dissertation submitted in partial satisfaction of the
requirements for the degree of
Doctor of Philosophy

in

Engineering

in the

GRADUATE DIVISION

of the

UNIVERSITY of CALIFORNIA at IRVINE

Committee in charge:

Professor Constantinos V. Chrysikopoulos, Chair
Professor Brett F. Sanders
Professor Jan W. S. Scherfig

2001

Polydisperse Colloid Transport in Fractured Media

© 2001

by

Scott C. James

The dissertation of Scott C. James is approved:

Chair

Date

Date

Date

University of California at IRVINE

2001

To my loving grandmother

Helen Marie Murphy Youngs

Contents

Nomenclature	vii
List of Figures	xi
List of Tables	xiv
Acknowledgements	xv
Curriculum Vitae	xvi
1 Introduction	3
1.1 Significance of Research	3
1.2 Research Objectives	5
1.3 Dissertation Overview	6
2 Literature Review	8
2.1 Flow and Transport in Saturated Fractured Media	8
2.1.1 Methods of Analysis	8
2.1.2 Flow in a Fracture	10
2.1.3 Transport Mechanisms	15
2.2 Physicochemical Characteristics of Colloids	17
2.3 Transport and Deposition of Colloids	19
2.4 Boundary Conditions	21
2.5 Particle Tracking	22
3 Effective Parameters for a Colloid Plume	24
3.1 Background	25
3.2 Mathematical Derivations	26
3.2.1 Effective Velocity	26
3.2.2 Effective Dispersion Coefficient	27
3.3 Discussion	32
3.4 Summary	34
4 Analytical Solutions	36
4.1 Background	37
4.2 Development of Models	37
4.2.1 Governing Transport Equations	37
4.2.2 Transport Parameters for Finitely Sized Particle Plumes	38

4.2.2.1	Non-sorbing or Reversibly Sorbing Particles	38
4.2.2.2	Irreversibly Sorbing Particles	39
4.3	Analytical Solutions	41
4.3.1	Instantaneous Injection Without Particle Sorption	41
4.3.1.1	Monodisperse Particle Plume	41
4.3.1.2	Polydisperse Particle Plume	42
4.3.2	Constant Concentration Injection Without Particle Sorption	43
4.3.2.1	Monodisperse Particle Plume	43
4.3.2.2	Polydisperse Particle Plume	44
4.3.3	Constant Concentration Injection with Irreversible Sorption	45
4.3.3.1	Monodisperse Particle Plume	45
4.3.3.2	Polydisperse Particle Plume	46
4.3.4	Constant Concentration Injection with Reversible Sorption	47
4.3.4.1	Monodisperse Particle Plume	47
4.3.4.2	Polydisperse Particle Plume	48
4.4	Discussion	51
4.5	Comparison with Experimental Data	56
4.6	Summary	56
5	A New Particle Tracking Equation	58
5.1	Introduction	58
5.2	Model Development	60
5.2.1	Traditional Particle Tracking Equation	60
5.2.2	New Particle Tracking Equation	62
5.3	Verification	68
5.3.1	Traditional Particle Tracking Algorithm	69
5.3.2	New Particle Tracking Algorithm	70
5.3.3	Comparisons	71
5.4	Summary	72
6	Transport in a Uniform Aperture Fracture	74
6.1	Introduction	74
6.2	Model Development	75
6.2.1	Flow and Transport	75
6.3	Matrix Diffusion	77
6.4	Colloid Deposition	77
6.4.1	Perfect Sink Approximation	77
6.4.2	Kinetic Relationship	79
6.5	Particle Tracking	81
6.6	Numerical Procedures	82
6.6.1	Transport	82
6.6.2	Matrix Diffusion	83
6.6.3	Deposition	85
6.7	Simulations and Discussion	86
6.7.1	Model Parameters	86
6.7.2	Comparison with an Analytical Solution	86
6.7.3	Effects on Spreading	88
6.7.4	Effects of Matrix Diffusion	90
6.7.5	Colloid Deposition	91
6.7.5.1	Perfect Sink Sorption	91
6.7.5.2	Kinetic Sorption	92
6.7.6	Effect of Varied Fracture Aperture	94

6.8	Summary and Conclusions	95
7	Transport in a Variable Aperture Fracture	97
7.1	Introduction	97
7.2	Fracture Generation	97
7.3	Flow in a Fracture	99
	7.3.1 Mathematical Model	99
	7.3.2 Numerical Formulation	100
7.4	Algorithm Development	102
	7.4.1 Particle Tracking	102
	7.4.2 Numerical Methods	103
7.5	Particle Deposition	104
7.6	Model Simulations	105
7.7	Summary	111
8	Application and Engineering Significance of Results	112
9	Summary, Conclusions and Future Research	114
9.1	Summary	114
9.2	Conclusions	116
9.3	Recommendations for Future Research	117
A	Governing Equations for Poiseuille Fluid Flow	119
B	Derivation of the Parabolic Velocity Profile	121
C	Effective Parameters for Irreversible Sorption	123
D	Derivation of the Harmonic Mean	127
E	Conformal Mapping	129
F	Bifurcating Flow Equations	136

Nomenclature

A	cross-sectional area per unit depth, $A = \Delta z$, L.
\mathbf{A}	absolute forcing vector for particle tracking, L/t.
A_p	cross-sectional area of a sorbed colloid, L ² .
b	uniform fracture aperture, L.
\bar{b}	mean aperture of a variable aperture fracture, L.
$b(x, y)$	local fracture aperture, L.
\mathbf{B}	deterministic scaling tensor for particle tracking, L ² /t.
C	integration constant, 1/L ⁴ .
d_p	colloid particle diameter, L.
D_{d_p}	molecular diffusion coefficient of a colloid particle, L ² /t.
D_{eff}	effective dispersion coefficient of a particle plume, L ² /t.
D_{Taylor}	Taylor dispersion coefficient of a solute plume, L ² /t.
Da	dimensionless Damköhler number.
f	log-normal probability density function.
\mathbf{F}	three-dimensional force vector, ML/t ² .
$F(n_{d_p}^*)$	dynamic blocking function.
g	gravitational acceleration, L/t ² .
h	piezometric head, L.
i	element number of a variable aperture fracture in the x -direction.
j	element number of a variable aperture fracture in the y -direction.
J	flux of colloid at the fracture surface (Chapter 6), 1/L ² t.
J_z	flux of colloids entering the control volume normal to z , 1/L ² t.
\bar{J}	average axial flux of particles relative to the moving coordinate ξ , 1/L ² t.
k	Boltzmann's constant, ML ² /Tt ² .
k_f	forward sorption rate coefficient, L/t.
k_r	reverse sorption rate coefficient, L.
K	saturated hydraulic conductivity, L/t.
K_{eff}	effective decay coefficient for an irreversibly sorbing colloid plume, 1/t.
m	numerical step number in the particle tracking equation.
n	local monodisperse colloid concentration in the fracture, 1/L ³ .
\bar{n}	average monodisperse colloid concentration across the fracture, 1/L ³ .
n_{cl}	centerline colloid number concentration, 1/L ³ .
n_{d_p}	local polydisperse colloid concentration in the fracture, 1/L ³ .
$n_{d_p}^*$	number of sorbed particle per unit fracture surface area, 1/L ² or 1/L.
\bar{n}_{d_p}	average polydisperse colloid concentration across the fracture, 1/L ³ or 1/L ² .
n_o	initial number concentration of monodisperse particles, 1/L ³ or 1/L ² .
$n_{o_{d_p}}$	initial number concentration of polydisperse particles, 1/L ³ or 1/L ² .
$n_o(d_p)$	initial number concentration of discretely sized polydisperse particles, 1/L ³ .
n_{pdf}	probability density function for concentration of polydisperse particles, 1/L ⁴ .
\dot{N}	number of colloids exiting a fracture.
\dot{N}	time rate of change of colloid number, 1/t.
N^*	total number of sorbed colloids.
N_o	total number of monodisperse particles in a plume.
$N_{o_{d_p}}$	total number of polydisperse particles in a plume.
N_{pdf}	probability density function for the number of polydisperse particles, 1/L.
p	probability of particle attachment per wall encounter.
P	local fluid pressure, M/Lt ² .
\mathcal{P}	reduced pressure, equal to $P + \rho gz$, M/Lt ² .

$P(z)$	probability of particle entering the fracture at location z .
Pe	dimensionless Peclet number.
q	volumetric flow rate per unit fracture width, L^2/t .
R	retardation coefficient.
$Rn(0, 1)$	uniformly distributed random number between 0 and 1.
Sh	dimensionless Sherwood number.
t	time, t .
Δt	time step for a particle tracking algorithm, t .
T	absolute temperature of the interstitial fluid, T .
\mathbf{u}	three-dimensional velocity vector, equal to u_x, u_y, u_z , L/t .
u_x	local Poiseuille fluid velocity in the x -direction, L/t .
\bar{u}_x	mean fluid velocity in the x -direction, L/t .
u_y	local fluid velocity in the y -direction for a variable aperture fracture, L/t .
\bar{u}_y	mean fluid velocity in the y -direction for a variable aperture fracture, L/t .
u_z	local fluid velocity in the z -direction, L/t .
u_ξ	velocity defect, equal to $x - u_x(z)t$ L/t .
$U_{\mathcal{D}}$	deterministic velocity due to a diffusivity gradient, L/t .
U_{eff}	effective velocity of a particle plume, L/t .
U_{max}	maximum velocity at the fracture centerline, L/t .
U_θ	deterministic velocity due to a porosity gradient, L/t .
V	control volume per unit depth, equal to $\Delta x \Delta z$, L^2 .
x	coordinate along the fracture length, L .
\mathbf{X}	three-dimensional position vector, L .
y	coordinate along the fracture width, L .
z	coordinate normal to the fracture surface, L .
Δz	spatial step for the new particle tracking algorithm, L .
Z	a standard normally distributed random number.
\mathbf{Z}	vector of three standard normally distributed random numbers.

Subscripts

cl	centerline colloid number concentration.
eff	effective parameter.
DBF	dynamic blocking function.
i	index indicating the element in the y -direction.
in	colloids entering the control volume.
j	index indicating the element in the x -direction.
max	maximum value.
out	colloids exiting the control volume.
pdf	probability density function.

Greek Letters

α	slope of the linear least squares fit for mean log–travel time.
β	y -intercept of the linear least squares fit for mean log–travel time, $\log t$.
γ	fluid specific weight, M/L^2t^2 .
ϵ	coefficient of surface coverage by colloids, equal to $A_p n_{d_p}^*(x, t)$.
ϵ_{\max}	maximum coefficient of surface coverage by colloids.
ζ^2	variance of particle log–diameters.
θ	matrix porosity.
κ	bulk or volume viscosity, M/Lt .
λ	mean of the particle log–diameters.
μ	fluid dynamic viscosity, M/Lt .
μ_{d_p}	mean particle diameter, L .
μ_τ	mean of the log–travel times.
ν	factor accounting for blocked area not directly covered by a colloid.
ρ	fluid density, M/L^3 .
ϕ	repulsive interaction energy between a particle and the fracture surface, ML^2/t^3 .
ξ	coordinate transformation, equal to $x - U_{\text{eff}}t$, L .
ξ_b	correlation length of the fracture aperture fluctuations, L .
σ_{d_p}	standard deviation of particle diameters, L .
$\sigma_{\ln b}^2$	variance of the log–fracture aperture fluctuations.
σ_τ^2	variance of the log–travel times.
τ	log–travel time, equal to $\ln \Sigma \Delta t$.
Ω	velocity coefficient for irreversibly sorbing colloids, equal to $(U_{\text{eff}}^2 + 4K_{\text{eff}}D_{\text{eff}})^{1/2}$, L/t .

Appendices E and F

f	arbitrary function.
g	gravitational acceleration.
i	node number in the x -direction.
j	node number the y -direction.
J	Jacobian transformation.
M	number of elements in the x -direction.
N	number of elements in the y -direction.
P	term in the Laplace equation controlling grid spacing, equal to zero.
\mathcal{P}	pressure.
Q	term in the Laplace equation controlling grid spacing, equal to zero.
r	bifurcating fracture dimension parameter.
s	bifurcating fracture dimension parameter.
t	bifurcating fracture dimension parameter or time.
u	bifurcating fracture dimension parameter or y -direction velocity.
x	coordinate location.
y	coordinate location.

Appendices E and F (Greek)

α	mapping constant.
β	mapping constant.
γ	mapping constant.
η	transformed y coordinate.
μ	fluid dynamic viscosity.
ξ	transformed x coordinate.
ρ	fluid density.
ϱ	grid spacing parameter.
ς	grid spacing parameter.
τ	factor included in the locally optimized overrelaxation parameter.
ψ	stream function.
ω	vorticity.
Ω	locally optimized overrelaxation parameter.

List of Figures

2.1	Idealization of a natural fracture as two parallel plates with constant aperture b and a Poiseuille flow profile.	11
3.1	Schematic illustration of the fracture considered in this study.	27
3.2	Schematic illustration of the ‘velocity defect’ represented by the shaded areas. Filled arrows indicate axial advection of particles and open arrows indicate transverse molecular diffusion of particles.	30
3.3	Effective parameters for finitely sized particles of diameter, d_p . The effective and mean velocities are compared in (a); and (b) compares the effective and Taylor dispersion coefficients as a function of particle size (here $b = 1 \times 10^{-4}$ m, $U_{\max} = 1 \times 10^{-6}$ m/s, and $T = 288.15$ K).	34
4.1	Particle concentration (a) snapshots and (b) breakthrough curves generated from (4.12) and (4.16) for 10,000 particles instantaneously injected at $t = 0$ into an aperture with $U_{\max} = 1 \times 10^{-6}$ m/s and $b = 1 \times 10^{-4}$ m. Three of the plumes are polydisperse and consist of particles with log-normally distributed diameters of $\mu_{d_p} = 1 \mu\text{m}$ and $\sigma_{d_p} = 0.3, 0.6,$ and $0.9 \mu\text{m}$, respectively, while the fourth plume is monodisperse and consists of particles with diameter $1 \mu\text{m}$. The snapshots of particle concentrations were evaluated 5,000 hours after injection and breakthrough curves were determined 12 m downstream from the particle injection location.	52
4.2	Normalized particle concentration (a) snapshots and (b) breakthrough curves evaluated by (4.20) and (4.21) for a constant concentration inlet boundary condition (here $U_{\max} = 1 \times 10^{-6}$ m/s, $b = 1 \times 10^{-4}$ m, $t = 5,000$ hr, and $x = 12$ m).	53
4.3	Normalized particle concentration (a) snapshots and (b) breakthrough curves evaluated by (4.29) and (4.31) for a constant concentration inlet boundary condition accounting for irreversible particle–wall reaction (here $U_{\max} = 1 \times 10^{-6}$ m/s, $b = 1 \times 10^{-4}$ m, $Da = 1 \times 10^{-3}$, $t = 5,000$ hr, and $x = 12$ m).	54
4.4	Normalized particle concentration (a) snapshots and (b) breakthrough curves evaluated by (4.37) and (4.38) for a constant concentration inlet boundary condition accounting for reversible particle–wall reaction (here $U_{\max} = 1 \times 10^{-6}$ m/s, $b = 1 \times 10^{-4}$ m, $k_r = 1 \times 10^{-5}$, $t = 5,000$ hr, and $x = 12$ m).	55
4.5	Comparison of experimental data from <i>Bales et al.</i> [1989] and the analytical solution (4.20) for <i>f2</i> coliphage (monodisperse particle) transport in a natural fracture in the absence of particle–wall reaction (here $b = 1.33 \times 10^{-4}$ m, $d_p = 2.3 \times 10^{-8}$ m, $\bar{U} = 2/3U_{\max} = 1.83 \times 10^{-5}$ m/s, and $x = 0.19$ m).	57

5.1	Pathline projected at (a) the x, y -plane; and (b) the x, z -plane of the Brownian motion for a particle of size $d_p = 1 \times 10^{-6}$ m released at the origin of a spherical volume of water of radius 5×10^{-5} m.	62
5.2	Histograms of travel times for monodisperse plumes of 500,000 particles of size (a) $d_p = 1 \times 10^{-7}$ m; (b) $d_p = 1 \times 10^{-6}$ m; and (c) $d_p = 1 \times 10^{-5}$ m, traveling a distance of $\Delta z = \pm 1 \times 10^{-5}$ m.	64
5.3	Probability distributions of log-travel times for the same monodisperse plumes used to generate Figure 5.2. The solid lines are obtained from the normal probability distribution function with parameters (a) $\mu_\tau = 5.588$ and $\sigma_\tau = 0.786$; (b) $\mu_\tau = 7.848$ and $\sigma_\tau = 0.787$; and (c) $\mu_\tau = 10.133$ and $\sigma_\tau = 0.787$	65
5.4	Variation of the mean log-travel time, μ_τ , as a function of the log of the ratio $(\Delta z)^2/\mathcal{D}_{d_p}$. The equation for the least squares fit (solid line) of the numerically determined values (open circles) and the corresponding correlation coefficient are shown.	67
5.5	Cumulative normalized particle breakthrough curves determined by the traditional and new particle tracking algorithms (dashed lines) as well as by the analytical solution (solid line).	71
6.1	Monodisperse colloid transport in a uniform aperture fracture at simulation times of (a) 5×10^9 seconds, (b) 10×10^9 seconds, and (c) 15×10^9 seconds (here $d_p = 1 \times 10^{-6}$ m, $U_{\max} = 1 \times 10^{-9}$ m/s, and $b = 1 \times 10^{-4}$ m).	76
6.2	Illustration of three log-normal distributions of colloid diameters with $\mu_{d_p} = 1 \times 10^{-6}$ m and $\sigma_{d_p} = 0.3, 0.6,$ and $0.9 \mu\text{m}$	87
6.3	Comparison of the analytical solution (solid lines) and the particle tracking simulations for a monodisperse colloid plume (circles) and the three polydisperse colloid plumes with $\mu_{d_p} = 1 \times 10^{-6}$ m and $\sigma_{d_p} = 0.3 \mu\text{m}$ (triangles), $\sigma_{d_p} = 0.6 \mu\text{m}$ (squares), and $\sigma_{d_p} = 0.9 \mu\text{m}$ (diamonds). Due to the two-dimensional nature of the fracture considered, areal colloid concentrations are presented (here $t = 5,000$ days).	88
6.4	Number of colloids with a given diameter for plumes of colloids with log-normal diameter distributions with $\mu_{d_p} = 1 \times 10^{-6}$ m and (a) $\sigma_{d_p} = 0.3 \mu\text{m}$, (b) $\sigma_{d_p} = 0.6 \mu\text{m}$, and (c) $\sigma_{d_p} = 0.9 \mu\text{m}$ (here $t = 5,000$ h). The colloids have been divided into thirds based on their travel distances. The squares represent the fastest third, the closed circles the middle third, and the open circles the slowest third (closest to the inlet).	89
6.5	Normalized cumulative breakthrough curves for plumes of colloids having different log-normal distribution of particle diameters in a fracture with uniform aperture and (a) 1% and (b) 10% solid matrix porosity (here $x = 5$ m).	90
6.6	Sorbed colloid concentrations under perfect sink conditions as a function of fracture length for colloid plumes having log-normal diameter distribution with $\mu_{d_p} = 1 \times 10^{-6}$ m and (a) $\sigma_{d_p} = 0.3 \mu\text{m}$, (b) $\sigma_{d_p} = 0.6 \mu\text{m}$, and (c) $\sigma_{d_p} = 0.9 \mu\text{m}$. The colloids have been divided into thirds based on their diameter. The open circles represent the smallest third, the closed circles the middle third, and the squares the largest third (here $t = 5,000$ h).	92
6.7	Overall sorbed colloid concentrations under linear DBF kinetic sorption conditions as a function of fracture length for the three polydisperse colloid plumes (here $t = 5,000$ h and $\phi = 10kT$). Due to the two-dimensional nature of the fracture considered, sorbed colloid concentrations per unit length are presented.	93
6.8	Sorbed colloid concentrations under linear kinetic sorption conditions as a function of fracture length for colloid plumes having log-normal diameter distributions with $\mu_{d_p} = 1 \times 10^{-6}$ m and (a) $\sigma_{d_p} = 0.3 \mu\text{m}$; (b) $\sigma_{d_p} = 0.6 \mu\text{m}$; and (c) $\sigma_{d_p} = 0.9 \mu\text{m}$. The colloids have been divided into thirds based on their diameter size (here $t = 5,000$ h and $\phi = 10kT$).	94

6.9	Effect of linear (open diamonds) and nonlinear (closed diamonds) DBFs on sorbed colloid concentrations along the fracture for colloid plumes having log-normal diameter distribution with $\mu_{d_p} = 1 \times 10^{-6}$ m and (a) $\sigma_{d_p} = 0.3 \mu\text{m}$; (b) $\sigma_{d_p} = 0.6 \mu\text{m}$; and (c) $\sigma_{d_p} = 0.9 \mu\text{m}$	95
6.10	Total number of sorbed colloids from a monodisperse suspension ($d_p = 1 \times 10^{-6}$ m) as a function of time for several different fracture apertures (here $x = 5$ m).	96
7.1	Schematic illustration of a quasi-three-dimensional fracture with spatially variable aperture $b(x, y)$ and a migrating plume of polydisperse colloids undergoing surface sorption. Note that $z = 0$ at the center of the fracture.	98
7.2	A realization of the aperture spatial distribution in the fracture plane. The fracture is partitioned into 80×40 equal-size elements. The varied shades illustrate apertures between 0.01 and 0.15 mm (here $x = 8$ m, $y = 4$ m, $\bar{b} = 1 \times 10^{-4}$ m, $\sigma_{\ln b}^2 = 0.15$, and $\xi_b = 1$ m).	99
7.3	Five-point finite difference stencil.	101
7.4	The velocity field in the variable aperture fracture shown in Figure 7.3. Arrow lengths are tangential and proportional to the local mean velocities.	102
7.5	Snapshots of colloid positions (flow from left to right) for (a) a monodisperse colloid plume in a uniform aperture fracture; (b) a polydisperse colloid plume in a uniform aperture fracture; (c) a polydisperse colloid plume in a variable aperture fracture; and (d) a polydisperse colloid plume undergoing sorption in a variable aperture fracture. The polydisperse colloid plumes are split into thirds based on particle size with triangles being the smallest third, squares the middle third, and circles the largest third (here $t = 17.5$ hr).	106
7.6	Normalized cumulative colloid breakthrough curves for a monodisperse and three polydisperse colloid plumes with mean diameter $\mu_{d_p} = 1 \mu\text{m}$ in a uniform fracture with aperture $b = 1 \times 10^{-4}$ m.	107
7.7	Normalized cumulative colloid breakthrough curves for a polydisperse colloid plume in variable aperture fractures with four different $\sigma_{\ln b}^2$ values (here $\bar{b} = 1 \times 10^{-4}$ m, $\sigma_{d_p} = 0.9 \mu\text{m}$, $\mu_{d_p} = 1 \mu\text{m}$, $\xi_b = 1$ m).	108
7.8	Normalized cumulative colloid breakthrough curves for a polydisperse colloid plume in variable aperture fractures with three different correlation lengths of the aperture fluctuations (here $\bar{b} = 1 \times 10^{-4}$ m, $\sigma_{\ln b}^2 = 0.037$, $\mu_{d_p} = 1 \mu\text{m}$, $\sigma_{d_p} = 0.9 \mu\text{m}$).	109
7.9	Normalized cumulative colloid breakthrough curves for an irreversibly sorbing polydisperse colloid plume in variable aperture fractures with four different $\sigma_{\ln b}^2$ values (here $\bar{b} = 1 \times 10^{-4}$ m, $\sigma_{d_p} = 0.6 \mu\text{m}$, $\mu_{d_p} = 1 \mu\text{m}$, $\xi_b = 1$ m, $\phi = 10kT$, $\nu = 15$).	110
E.1	Coordinate mapping of the bifurcating fracture considered in this study.	133
E.2	Nodal mapping of the bifurcating fracture considered in this study. Here, $M_I = 40$, $M_{II} = 20$, $M_{III} = 20$, $M_{IV} = 40$, and $N = 20$	135
F.1	Contour plot of the streamlines in a bifurcating fracture.	140

List of Tables

4.1	Analytical solutions for monodisperse particle transport in saturated fractures. . . .	49
4.2	Analytical solutions for polydisperse particle transport in saturated fractures. . . .	50
6.1	Model parameters for simulations.	86

Acknowledgements

I am indebted to my wonderful grandmother, Helen Marie Youngs, who aided in my financial support as I pursued my doctorate. My graduate experience has been greatly enriched because of her generous gifting. I wish to express my sincere gratitude and appreciation to my advisor Dr. Constantinos Chrysikopoulos; without his guidance this dissertation would not have been possible. I would like to thank my committee member Dr. Brett Sanders for his thoughtful comments, understanding, and genuine interest in my welfare. I am also indebted to my other committee member Dr. Jan Scherfig for his participation and support. Appreciation is extended to Dr. Stanley Grant for many stimulating discussions. My highest regards go to Dr. De Gallow who was instrumental in my development as a teacher. In addition, I would like to acknowledge my current office mates Tanya Bilezikjian and Eric Vogler, and my former office mates, Dr. T.-J. Kim, Dr. Ken Lee, Dr. Youn Sim, and Mike Tatalovich.

So many people have impacted and enhanced my life during my tenure at UCI. Special thanks must be extended to my best friend, Derrick DiNucci, whose continued support, advice, guidance, and generosity measurably increased my productivity and immeasurably influenced and fostered many fond memories. From one black sheep to another, Kevin Nichols, I am proud to be your friend. Many others deserve special mention for sharing the highs with me and lending an ear or a shoulder through the lows, particularly Laura Chaney, Nancy Blake, and Nicole Mye. The support, friendship, and love of my family and extended family including my brother Monty James, my loving mother, Joe Williams, Uncle Johnny Scott, Mark and Tiffany Boyd, and Ron and Kimmi Newlin are neither underestimated nor under appreciated. My sweetheart Trina Giordano, I am honored by your companionship and love; much more awaits us. You all have my deepest thanks.

I sincerely appreciate the help and support I received from the Department of Civil and Environmental Engineering and from the UCI Regents' Dissertation Fellowship.

CURRICULUM VITAE

Scott C. James

Department of Civil & Environmental Engineering
 UNIVERSITY OF CALIFORNIA, IRVINE, CA 92697-2175
 (949) 824-7711 [phone] — (949) 824-3672 [fax]
 sjames@eng.uci.edu
<http://www.eng.uci.edu/~sjames>

EDUCATION

Doctor of Philosophy: Engineering, June, 2001
 UNIVERSITY OF CALIFORNIA, IRVINE

Master of Science: Mechanical Engineering, June, 1994
 UNIVERSITY OF CALIFORNIA, SAN DIEGO

Bachelor of Science: Engineering Science, June, 1993
 UNIVERSITY OF CALIFORNIA, SAN DIEGO

AWARDS, HONORS, AND CERTIFICATIONS

UCI Regents' Dissertation Fellowship, Spring 2001
 UCI Graduate representative to the Council on Research, Computing, and Library Resources, 2000-2001
 UCI Teaching Excellence Award, 1999-2000 and 2000-2001
 UCI School of Engineering Outstanding TA Award, 1999-2000
 UCI Regents' Fellow
 UCI and UCSD Honor Roll
 UCSD Regents' Scholar
 Engineer-in-Training certification, November, 1994
 National Merit Scholar

EMPLOYMENT

(5/99-present) TEACHING ASSISTANT CONSULTANT, School of Engineering, University of California, Irvine

(1/97-present) INSTRUCTOR, The Princeton Review, Physics for the MCAT, Irvine, California

(9/96-present) TEACHING ASSOCIATE, Department of Civil and Environmental Engineering, University of California, Irvine

(9/95-present) TEACHING and RESEARCH ASSISTANT, Department of Civil and Environmental Engineering, University of California, Irvine

(6/00-7/00) COSMOS INSTRUCTOR, California State Summer School for Mathematics and Science, University of California, Irvine

(9/94-9/95) SAIC PROCESS TECHNOLOGY DIVISION, San Diego, California

(9/93-6/94) TEACHING ASSISTANT, Department of Applied Mechanics and Engineering Science, University of California, San Diego

(6/93-9/93) RESEARCH ASSISTANT, Naval Research and Development Center, Point Loma

TEACHING EXPERIENCE[†]

Computational Methods in Engineering — Lower Division (F95, SS96, F96[†], SS97[†])
 Numerical Methods in Engineering — Lower Division (F97, SS98[†], F98, SS99[†], F99)
 Thermodynamics — Lower Division (S96, S97)
 Introduction to Fluid Mechanics — Upper Division (W96, W97[†], W98, W99)
 Hydraulics Laboratory — Upper Division (S 98, S99)
 Wastewater Engineering — Upper Division (W99)
 Linear Algebra — Lower Division (F00)
 Computation Methods in Electrical and Computer Engineering — Lower Division (W01[†])

[†] Teaching portfolio available upon request.

[†] Teaching Associate (Instructor).

PUBLICATIONS

Peer Review Journal Articles

- JAMES, S. C. and C. V. CHRYSIKOPOULOS, An efficient particle tracking equation with specified spatial step for the solution of the diffusion equation, *Chemical Engineering Science*, submitted, 2001.
- JAMES, S. C. and C. V. CHRYSIKOPOULOS, Effective velocity and effective dispersion coefficient for finitely sized particles flowing in a uniform fracture, *Water Resources Research*, submitted, 2001.
- JAMES, S. C. and C. V. CHRYSIKOPOULOS, Analytical solutions for the transport of monodisperse and polydisperse particle suspensions in a uniform fracture, *Proceedings of the Royal Society of London Series A: Mathematical and Physical Sciences*, submitted, 2000.
- JAMES, S. C. and C. V. CHRYSIKOPOULOS, Transport of polydisperse colloids in a saturated fracture with spatially variable aperture, *Water Resources Research*, 36(3), 1457–1466, 2000.
- JAMES, S. C. and C. V. CHRYSIKOPOULOS, Transport of polydisperse colloid suspensions in a single fracture, *Water Resources Research*, 35(3), 707–718, 1999.

Conference Proceedings

- JAMES, S. C. and C. V. CHRYSIKOPOULOS, Transport of polydisperse colloid suspensions in a variable aperture fracture (Extended Abstract), *Abstracts of Papers of the American Chemical Society*, 217: 206–ENVR(1), 1999.
- JAMES, S. C. and C. V. CHRYSIKOPOULOS, Transport of polydisperse colloid suspensions in a single fracture (Abstract), *EOS, Transactions, American Geophysical Union*, 79(47), 325, 1998.

Poster Presentations

- BILEZIKJIAN, T. K., S. C. JAMES, and C. V. CHRYSIKOPOULOS, Colloid and contaminant co-transport in a variable aperture fracture (Abstract), *EOS, Transactions, American Geophysical Union*, 81(48), 431, 2000.
- CHRYSIKOPOULOS, C. V. and S. C. JAMES, A diffusive particle tracking equation with a specified spatial step (Abstract), *EOS, Transactions, American Geophysical Union*, 81(48), 468, 2000.
- JAMES, S. C. and C. V. CHRYSIKOPOULOS, Analytical solutions for polydisperse particle transport in a uniform fracture (Abstract), *EOS, Transactions, American Geophysical Union*, 81(48), 469, 2000.
- JAMES, S. C. and C. V. CHRYSIKOPOULOS, The effect of polydispersity on colloid transport in a saturated fracture with spatially variable aperture, *AIChE Annual Meeting*, 2000.
- JAMES, S. C. and C. V. CHRYSIKOPOULOS, Effect of polydispersity on colloid transport in a variable aperture fracture, *22nd Biennial Groundwater Conference*, 104, 1999.
- JAMES, S. C. and C. V. CHRYSIKOPOULOS, Transport of polydisperse colloid suspensions in a variable aperture fracture, *American Chemical Society, Division of Environmental Chemistry*, 394–396, 1999.
- JAMES, S. C. and C. V. CHRYSIKOPOULOS, Transport of variably sized colloids in a single fracture, *Seventeenth Annual American Geophysical Union Hydrology Days*, 141–150, 1997.
- JAMES, S. C. and C. V. CHRYSIKOPOULOS, Effect of colloidal size on colloid transport in fractured media (Abstract), *EOS, Transactions, American Geophysical Union*, 77(46), 213, 1996.

SCIENTIFIC AND PROFESSIONAL SOCIETY MEMBERSHIPS

American Geophysical Union (AGU)
 American Institute of Chemical Engineering (AIChE)
 American Chemical Society (ACS)
 American Society of Civil Engineers (ASCE)
 American Society of Mechanical Engineers (ASME)
 Golden Key National Honors Society

Abstract

Polydisperse Colloid Transport in Fractured Media

by

Scott C. James

Doctor of Philosophy in Engineering

University of California at IRVINE

Professor Constantinos V. Chrysikopoulos, Chair

The initial phase of the study will analytically solve for the transport characteristics of a finitely sized particle in a uniform aperture fracture. Results show that the larger the constituents of a colloid plume, the greater the mean plume velocity and the lesser the plume dispersion. Incorporating these parameters into analytical solutions for the transport of polydisperse colloid plumes in a uniform aperture fracture shows that not only does the size of the constituents affect the transport of the plume, but that a distribution of particle sizes further increases the spreading of the plume.

Next, a new constant spatial step particle tracking equation is developed to solve for the transport characteristics of both monodisperse and polydisperse reactive colloids in a single fracture. Using both the traditional and the new particle tracking algorithms, the transport characteristics of colloid plumes in a uniform aperture fracture are investigated. Matrix diffusion and surface sorption characteristics are incorporated into the model. Both perfect sink and kinetic colloid sorption onto fracture surfaces are investigated. The finite size of a colloid particle as well as the size distribution of the colloid plume will implicitly change the transport parameters of a plume as its constituents travel through a fracture, sorbs onto the fracture surface, or diffuses through the rock matrix.

As an extension to this, the parallel plate model is generalized to the more realistic case of polydisperse colloid transport in a fracture with spatially variable aperture. The fracture aperture spatial variability is considered a stochastic variable and finite differencing techniques are used to develop the flow field in each variable aperture fracture. These flow fields are used as input data for the new particle tracking algorithm. Normalized cumulative breakthrough curves of polydisperse colloid plumes are produced by repeatedly tracking a plume of particles through unique realizations of stochastically generated fractures and incorporated into an ensemble average. Further, the effects of kinetic sorption of colloids onto the walls of a variable aperture fracture are studied. It is shown that not only does the variability in size of the polydisperse colloids affect their transport, but also that the variability of the fracture aperture has a significant influence as well.

Professor Constantinos V. Chrysikopoulos
Dissertation Committee Chair

Chapter 1

Introduction

1.1 Significance of Research

Hazardous wastes, especially radioactive materials, are often disposed in canisters and buried in deep, fractured, low-permeability rock formations (e.g., granites, slates, gneisses, and clays). In the United States, the first federally funded disposal site of this type, opening in 2004, is the Geologic Repository for the Disposal of Spent Nuclear Fuel and High-Level Radioactive Waste at Yucca Mountain, in Nye County, Nevada. Research activities surrounding the design and construction of this site have stimulated a great deal of interest in characterizing subsurface colloid and contaminant migration in fractured media, and in investigating the capacity of natural barriers to retard the movement of leaked contaminants [e.g., *Neretnieks et al.*, 1982; *Abelin*, 1986; *Raven et al.*, 1988; *Haldeman et al.*, 1991; *Johns and Roberts*, 1991; *Krishnamoorthy et al.*, 1992]. Although the diffusion of contaminants and colloids through rock medium is often negligible, fractures, ubiquitous in these formations, have been shown to provide preferential flow paths. Unlike transport phenomena observed in porous media, contaminants do not disperse through fractured media as a plume, instead fingering through the fracture network, often resulting in contamination at great distances from the source.

Transport of colloids in subsurface formations has increasingly captured the attention of many researchers, because of the potential impact of colloids in facilitating the transport of pollutants and toxic elements [e.g., *McDowell-Boyer et al.*, 1986; *Torok et al.*, 1990; *Puls and Powell*, 1992; *Grindrod*, 1993]. Several experimental and field studies indicate that contaminants can migrate adsorbed on the surface of colloid particles thereby assuming transport characteristics of colloids that may vary significantly from their own [e.g., *Buddemeier and Hunt*, 1988; *Champ and Schroeter*, 1988; *Toran and Palumbo*, 1992; *Moulin and Ouzounian*, 1992]. The results of these studies suggest that colloids may not only enhance the mobility of contaminants, but may also inhibit the retardation and dilution of contaminant plumes by reducing the extent of sorption onto fracture surfaces and diffusion into the rock matrix. Unfortunately, conceptual models that describe fractured systems usually do not account for the finite size and polydisperse characteristics of a natural colloid plume.

In modeling colloid transport in fractured rocks, a common simplification/assumption employed by researchers is of infinitely small particles traveling in a single fracture separated by a constant aperture, known as the parallel plate model [e.g., *Grisak and Pickens*, 1981; *Tang et al.*, 1981; *Neretnieks et al.*, 1982; *Novakowski et al.*, 1985; *Raven et al.*, 1988; *Shapiro and Nicholas*, 1989; *Johns and Roberts*, 1991; *Ibaraki and Sudicky*, 1995; *Cormenzana*, 2000]. Flow in a single fracture is often described by the cubic law, where the flow rate is proportional to the cube of the fracture aperture [*Neuzil and Tracy*, 1981; *Abdel-Salam*, 1995]. Colloid transport in a fracture is then coupled with diffusion into or sorption onto the host rock matrix through source/sink terms governing the interaction between these two systems. Because the simplifying assumptions associated with the derivation of the cubic law do not represent the actual geometric conditions of a rock fracture, several modifications to the parallel plate fracture model have been proposed. The shape of the void is primarily influenced by the mechanical properties of the rock, the geometric characteristics of the fracture surfaces, the relative displacement of the two surfaces, and the stress to which the rock is subjected [*Abelin*, 1986]. A correction term is often included in the cubic law to account for surface roughness (roughness perturbations in the fracture surface), existence of asperities or contact points,

and/or the tortuosity of the flow system [e.g., *Witherspoon et al.*, 1980; *Neuzil and Tracy*, 1981]. *Zimmerman and Bodvarsson* [1996] indicated that a correction for roughness alone is not adequate for fractures with surfaces highly in contact (i.e., very small apertures), wherein preferential flow paths may exist. This phenomenon has been observed in several field and laboratory experiments [*Neretnieks*, 1983; *Abelin*, 1986; *Haldeman et al.*, 1991]. Several conceptual models have been proposed to simulate preferential flow, including two- and quasi-three-dimensional variable aperture fractures [*Tsang and Tsang*, 1987; *Moreno et al.*, 1988; *James and Chrysikopoulos*, 2000].

In this dissertation analytical and theoretical investigations are undertaken to gain a better understanding of transport of finitely sized polydisperse colloids in single saturated fractures. Initially, analytical solutions to the mathematical model describing the transport of finitely sized colloids in a one-dimensional semi-infinite fracture subject to several different boundary conditions are developed. Then a novel particle tracking algorithm is developed and verified through comparison with the analytical solutions. This particle tracking algorithm is then used to examine more general transport in a uniform aperture fracture. Finally, because natural fractures have variable apertures along their length, the particle tracking algorithm is extended to examine polydisperse colloid transport within a quasi-three-dimensional spatially variable aperture fracture.

1.2 Research Objectives

This research focuses on polydisperse colloid transport in single saturated fractured media. As a first step, colloid and contaminant transport are studied within the framework of a single fracture conceptualized as a pair of parallel plates. The finite size of the colloid particles are found to affect their transport properties. Analytical solutions are derived that model the transport of finitely sized polydisperse particle plumes in uniform aperture fractures. Next, a novel particle tracking algorithm is developed and validated upon comparison to analytical solutions for colloid transport in a uniform aperture fracture. Then, assuming that the aperture of a two-dimensional

fracture is a stochastic variable, the effect of colloid size on colloid transport is examined. The specific objectives of this research are to:

- specify the size effect of finitely sized colloids on their transport properties;
- develop analytical solutions for the transport of polydisperse colloids in a one-dimensional semi-infinite fracture subject to several sets of boundary and initial conditions without penetration into the rock matrix, but accounting for both irreversible and reversible reaction with the fracture walls;
- derive and verify a novel particle tracking algorithm through comparison with the analytical solution;
- investigate the effect of polydispersity on colloid transport in a single fracture idealized as two parallel plates where the effects of matrix diffusion and surface sorption are included; and
- model polydisperse colloid transport in a two-dimensional spatially variable aperture fracture and investigate the effects of finite size and aperture variation on colloid transport.

1.3 Dissertation Overview

This dissertation is divided into nine chapters. Chapter 1 is an introduction with an outline of the specific objectives of this study. Chapter 2 provides the background material and literature review.

Chapter 3 derives the effective velocity and dispersion coefficient for a plume of finitely sized particles traveling in a water saturated uniform aperture fracture.

Chapter 4 develops models describing the transport of colloids in a one-dimensional semi-infinite fracture. Several analytical solutions are constructed for both instantaneous particle injection and constant concentration particle injection boundary conditions as well as for cases of reversible and irreversible sorption onto the fracture walls.

In Chapter 5, a new particle tracking algorithm is presented. In this new equation, instead of a constant time step, a constant spatial step is specified. The time for a particle to move this specified distance is selected from a distribution of random numbers that is a function of the particle diameter and the distance traveled. This algorithm is verified against previously derived analytical solutions.

In Chapter 6, a more general particle tracking model describing the transport of a polydisperse colloids in a uniform aperture fracture is developed. Colloids are allowed to either diffuse into the surrounding rock matrix or sorb onto the fracture surfaces.

In Chapter 7, the polydisperse colloid particle tracking algorithm presented in Chapter 6 is extended to quasi-three-dimensional fractures with spatially variable aperture. The system is investigated using the new particle tracking algorithm with a specified spatial step and variable time step. The effect of size exclusion and variable aperture on colloid transport is examined. Moreover, the influence of colloid attachment onto the wall is taken into account.

Finally, the implications and the significance of the results of this research is outlined along with the possible applications are discussed in Chapter 8. Then, Chapter 9 summarizes and presents the major conclusions of this research with recommendations for future research.

Chapter 2

Literature Review

2.1 Flow and Transport in Saturated Fractured Media

The term fracture is a general one referring to various types of discontinuities (joints, fracture zones, and shear zones) that can break a subsurface medium into blocks [Drever, 1985]. Fractures are found in almost all types of rocks: sedimentary (e.g., sandstone), metamorphic (e.g., limestone), and igneous or crystalline (e.g., granite). Naturally fractured systems contain extreme and abrupt changes in porosity and permeability, and can be characterized by two distinct components, fractures and matrix blocks. Fractures are the primary transmission conduits for fluids, colloids, and contaminants and have permeabilities several orders of magnitude greater than the permeability of the surrounding rock matrix [Abdel-Salam, 1995].

2.1.1 Methods of Analysis

Fractured media are complex, heterogeneous, and anisotropic systems necessitating certain idealizations when modeling flow and transport. Three different approaches are commonly used that depend on the number and location of fractures, size of the study area, and purpose of the study: the equivalent porous medium approach [e.g., Bear, 1972; Grisak and Cherry, 1975; Bear

and Verruijt, 1987; Rubin *et al.*, 1999]; the discrete fracture approach [e.g., Gringarten *et al.*, 1974; Neuzil and Tracy, 1981; Schwartz *et al.*, 1983; Long and Witherspoon, 1985; Cacas *et al.*, 1990a, b; Grindrod, 1993; Grindrod and Lee, 1997; James and Chrysikopoulos, 1999, 2000]; and the dual porosity approach [e.g., Tang *et al.*, 1981; Sudicky and Frind, 1984; Johns and Roberts, 1991; Ibaraki and Sudicky, 1995; Cormenzana, 2000].

- (1) The equivalent porous medium (or the single-continuum) approach assumes that the fractured medium behaves as a porous medium and is appropriate when the medium of interest contains many interconnecting fractures, i.e. the local effects of fractures may be incorporated into the parameters describing the system. In this approach, concepts and laws describing flow and transport in porous media are employed. To be able to use this approach, effective values for the important parameters (e.g., hydraulic conductivity for fluid flow and dispersivity for solute transport) need to be defined; however, obtaining estimates of these parameters is often difficult.
- (2) When fractures are sparse, it is not a good approximation to define the entire fractured medium by averaged quantities, therefore the discrete fracture approach is employed. In this approach each fracture is regarded as a separate entity and its detailed geometry is incorporated into the modeling process, deterministically or stochastically. Discrete fractal or stochastic representations of fractures have been used in the problem of flow [e.g., Robinson, 1983; Long and Witherspoon, 1985; Brown, 1995], and solute transport [e.g., Schwartz *et al.*, 1983; Rasmuson, 1985; Tsang and Tsang, 1987; Moreno *et al.*, 1997]. Based on statistical distributions of fracture aperture, fracture length, fracture spacing, and fracture orientation, a fracture network may be generated.
- (3) For smaller scale problems (e.g., flow to wells) or when the interaction between fractures and the rock matrix is important, a dual porosity model is employed. This conceptual model was first introduced by Barenblatt *et al.* [1960]. In this approach the fractures and the rock matrix

are modeled separately and then coupled by a source/sink term governing their interaction. Because of the difference in conducting properties between fractures and the rock matrix, it is often assumed that flow and transport are primarily generated by the fractures while the rock matrix provides a sink for contaminants. Further, the rock matrix may act as a source for back diffusion after the bulk of a contaminant pulse has traveled down the fracture.

In a fractured subsurface medium, a fracture network generally controls flow and transport [Lowell, 1989]. The basic constructive unit in fractured media is a single fracture, and a single fracture is often used as a starting point to represent a medium consisting of a series of parallel fractures [Tang *et al.*, 1981; van der Lee *et al.*, 1992; Robinson *et al.*, 1998]. Furthermore, a single fracture may significantly influence overall fluid, contaminant, and colloid movement within a fracture network. Therefore, to study contaminant and colloid transport in fractured networks, it is important to understand the transport mechanisms in a single fracture. Significant efforts have been directed toward modeling flow and contaminant transport in single fractures [e.g., Neuzil and Tracy, 1981; Neretnieks *et al.*, 1982; Neretnieks, 1983; Novakowski *et al.*, 1985; Tsang and Tsang, 1987; Moreno *et al.*, 1988; Raven *et al.*, 1988; Shapiro and Nicholas, 1989; Abdel-Salam, 1995; Brown *et al.*, 1995; James and Chrysikopoulos, 1999, 2000].

2.1.2 Flow in a Fracture

In many geological formations with low matrix permeability, fluid flow takes place through a single fracture or fault, while in other cases the flow occurs through a network of fractures. In either case, an understanding of flow through a single rock fracture is needed. A single fracture may be regarded as a void enclosed by two surfaces [Abdel-Salam, 1995]. The shape of the void is primarily influenced by the mechanical properties of the rock, the geometric characteristics of the fracture surfaces, the relative displacement of the two surfaces, and the stress (overburden) applied to the rock. The fracture void may be subjected to weathering by the flowing water due to dissolution, precipitation or clogging with small particles (e.g., colloidal particles). Typically, the fracture void (aperture) decreases with depth because of increasing overburden pressure [Abdel-Salam, 1995].

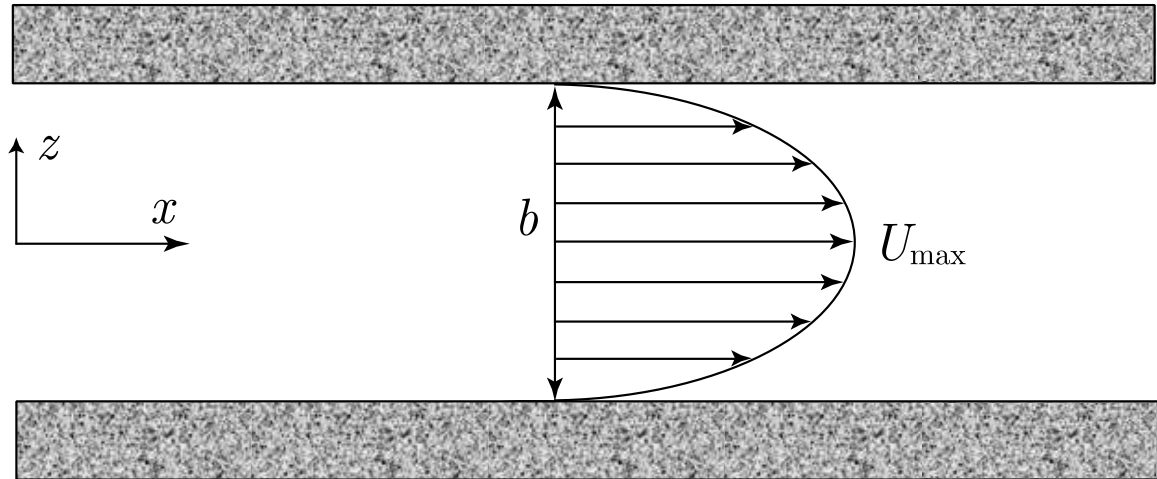


Figure 2.1: Idealization of a natural fracture as two parallel plates with constant aperture b and a Poiseuille flow profile.

Early studies of fracture hydrology idealized single fractures as a pair of smooth parallel plates separated by a constant aperture. This simplification, motivated by the observation that parallel plate geometry resembles the general geometry of a fracture allows flow rate and other transport properties in the fracture to be described by a parallel plate model [Abdel-Salam, 1995; James and Chrysikopoulos, 1999].

Figure 2.1 displays an idealization of a natural fracture as two parallel plates. Surrounding the two fracture plates is the host rock matrix that is assumed to be a very tight porous medium. Although various methods have been devised for specifying the flow field in a single rough walled fracture [e.g., Kirkpatrick, 1973; Ge, 1997; di Federico, 1998; Gavrilenko and Guéguen, 1998; Skjetne *et al.*, 1999], one technique has emerged as the primary method of solution to flow in a single fracture; solution of the Navier–Stokes equations. Several assumptions and simplifications are applied to the Navier–Stokes equations to make them more amenable to numerical or analytical solution. Initially, the viscous fluid within the fracture (water) is assumed to be Newtonian and incompressible. Further, the ‘no slip’ condition is enforced implying that both the normal and tangential components of velocity vanish at the walls. Fracture flow is generally defined under the assumption of steady–state flow subject to a uniform piezometric head gradient, eliminating the transient term in the Navier–

Stokes equation. Finally, slow, laminar flow is assumed in the fracture and the advective component of acceleration disappears, linearizing the Navier–Stokes equations (see Appendix A). The solution of the linearized Navier–Stokes equations results in fracture flow that varies as the cube of the fracture aperture (see Appendix B). For the ideal case of a parallel plate fracture, the volumetric flow rate per unit fracture width normal to the flow can be expressed as [Fox and McDonald, 1992, p. 330]

$$q = -\frac{b^3\gamma}{12\mu} \left(\frac{dh}{dx} \right), \quad (2.1)$$

where b is the aperture separating the fracture surfaces; μ is the fluid dynamic viscosity; γ is the specific weight of the interstitial fluid; h is the piezometric head; and x is the coordinate along the fracture axis. The preceding equation is well known in the literature as the cubic law or the parallel plate equation, and is valid for laminar flow conditions in a fracture with no surface contact and negligible surface roughness. Equation (2.1) is also a form of Darcy’s law with hydraulic conductivity, K , expressed as

$$K = \frac{b^2\gamma}{12\mu}. \quad (2.2)$$

Schrauf and Evans [1986] indicated that the principle argument against the use of the parallel plate model is that it ignores the roughness, waviness, and tortuosity of natural fracture surfaces, as well as the existence of surface contact between the fracture surfaces, all of which serve to reduce the flow rate. Moreover, at high normal stresses caused by overburden pressure, fracture surfaces tend to close, the contact area between these surfaces increases, and consequently, the fracture aperture takes on a range of values rather than one single value [Moreno *et al.*, 1988]. Many laboratory and field studies [e.g., *Novakowski et al.*, 1985; *Rasmuson and Neretnieks*, 1986; *Raven et al.*, 1988; *Novakowski et al.*, 1995] indicate that the classical view of a rock fracture as a pair of smooth, parallel plate is not adequate for the description of flow. Theoretical studies of single–fracture flow [e.g., *Brown*, 1987; *Moreno et al.*, 1988; *Oron and Berkowitz*, 1998]; however, have postulated that the fracture flow field is well described by the Reynolds equation derived by combining the continuity

equation and the Navier–Stokes equations to yield

$$\nabla \cdot [b^3(x, y) \nabla h] = 0, \quad (2.3)$$

where $b(x, y)$ is the local fracture aperture; x and y are the coordinates in the plane of the fracture; and $\nabla \cdot$ denotes divergence ($\nabla \cdot \mathbf{v} = \partial v_x / \partial x + \partial v_y / \partial y$, where \mathbf{v} is an arbitrary two-dimensional vector). *Hasegawa and Izuchi* [1983] concluded that the local cubic law is in general an adequate approximation when applied to a fracture with a sinusoidally varying aperture; however, the applicability of the local cubic law to real fractures remained in question. *Oron and Berkowitz* [1998] performed an order-of-magnitude analysis of the Navier–Stokes equations and concluded that if the local cubic law was applied not on a point-by-point basis, but rather as an average over a certain length, that it was a valid method for determining the fracture flow field. *Dijk et al.* [1999] applied nuclear magnetic resonance imaging to the direct three-dimensional measurement of flow in a rough-walled water-saturated rock fracture. They determined that the velocity profiles are generally parabolic, but often asymmetric. The effects of the measured asymmetry on volumetric flow rates and hydraulic conductivities were found to be insignificant while the overall flow inside rough walled fractures still obeyed the cubic law. Deviations from the cubic law may be expected if there is significant surface roughness or if a large number of asperities exist. It is of note that contact areas within the fracture, $b(x, y) = 0$, eliminate the cubic law as a method for determining the fracture flow field, necessitating alternate solution techniques [*Kumar et al.*, 1990; *Zimmerman and Bodvarsson*, 1996]

Other problems with the application of the local cubic law to flow in a fracture may exist. Field studies of solute migration in single fractures in the Stripa mine in Sweden showed that the flow was very unevenly distributed along fracture planes and that large areas did not carry any water [*Neretnieks*, 1983]. The amount and residence time of non-sorbing tracers collected at sampling points within the same fracture varied significantly, and many aliquots registered no tracer concentration at all. This indicates that the majority of flow took place along a few selected paths, or

flow channels, that make up only a small percentage of the fracture plane. Another field experiment carried out in a single fracture in granitic rock at Cornwall in Wales, demonstrated that the majority of flow in a single fracture also took place in a limited number of channels, occupying a small area of the fracture plane [Abelin, 1986]. These results are strongly indicative of localized channel flow within individual fractures.

Haldeman et al. [1991] performed a laboratory study of fluid flow and solute transport through a fracture embedded in porous tuff. Breakthrough curves and temporal moments analyses show that channeling of flow in the fracture segment probably occurred within at least one preferential flow path. Laboratory experiments have been performed where molten wood's metal was injected into single fractures, at different levels of applied stress. The fractures were opened up when cooled, and direct evidence of the formation of tortuous paths in single fractures was observed. This is an indication that the channels are tortuous, yet may or may not intersect each other. Channeling will lead to earlier initial breakthrough of contaminants than would be found in a uniform aperture fracture with an equivalent fracture volume.

Several conceptual models attempt to replicate channeling phenomenon. For instance, *Neretnieks et al.* [1982] modeled channeling as a bundle of independent channels, each with a constant aperture selected from a representative aperture statistical distribution (e.g., a log-normal distribution). *Tsang and Tsang* [1987] described fluid flow through a system of independent flow channels, each with a variable aperture along its length. The local channel aperture follows a given statistical distribution, and the variation of the aperture along each channel is regulated by a finite spatial correlation length. *Brown* [1987] used a fractal model to generate a mathematical representation of fracture surfaces that emulates channeling. *Moreno et al.* [1988] modeled the channeling phenomenon by superimposing the fracture plane onto a two-dimensional regular grid with a distinct aperture assigned to each element. The apertures are sampled from a log-normal distribution and vary according to an isotropic finite spatial correlation length. *Tsang and Tsang* [1987] extended the model of *Moreno et al.* [1988] to include an anisotropic finite spatial correlation length. Al-

though these studies identify fracture flow phenomena, some contaminant transport characteristics were examined as well. However, the driving force for the contaminants was restricted to advection-dominated dispersion and did not account for the effects of molecular diffusion, sorption, matrix diffusion, and Taylor dispersion.

2.1.3 Transport Mechanisms

The study of contaminant and colloid transport in fractured media has its roots in the pioneering work of Sir Geoffrey *Taylor* [1953]. When a soluble substance is introduced into a fluid flowing slowly through a small-bore tube, it moves under the combined action of molecular diffusion and the variation of velocity over the cross-section. *Taylor* [1953] showed that the distribution of the solute is symmetrically centered about a point moving with the mean solvent velocity; however, the dispersion along the tube is not only a function of the molecular diffusion coefficient, but of the system characteristics as well (i.e., tube radius and maximum or centerline flow velocity). The rate of spreading of the solute is described by the Taylor dispersion coefficient and may be orders of magnitude greater than spreading under the action of molecular diffusion alone. *Aris* [1956] extended *Taylor's* groundbreaking work by employing moment analysis to obtain results in a more generalized manner. These original studies, however, apply only to non-reactive solute transport. *Sankarasubramanian and Gill* [1974] and *Brenner* [1980, 1982] continued the study of internal flow and transport by developing exact solutions for the dispersion of reactive solutes in a tube. Following the *Taylor-Aris* procedures, scientists have examined various aspects of contaminant transport in parallel plate systems. *DeGance and Johns* [1978] and *Shapiro and Brenner* [1986, 1987, 1988] have obtained approximate analytical models for the dispersion of reactive solutes in cylindrical or parallel plate geometries and concluded that the Taylor dispersion coefficient needs to be modified to account for solute flux at the system boundaries due to reactions with the walls.

Analytical solutions for contaminant transport in fractured porous media where contaminants are subject to plug flow advection, dispersion, matrix diffusion, surface and matrix sorption,

and decay have been presented [Tang *et al.*, 1981; Sudicky and Frind, 1982; Cormenzana, 2000]. Abdel-Salam and Chrysikopoulos [1994] derived closed-form analytical solutions for colloid transport in single, uniform rock fractures with and without colloid penetration into the rock matrix for constant concentration as well as constant flux boundary conditions. It was shown that axial advection, transverse diffusion, and penetration into or reaction with the solid matrix govern colloid migration in uniform aperture fractures.

For the more realistic case of a variable aperture fracture, other mechanisms may contribute to the dispersion of contaminants and colloids in a fracture. Dispersion in fractures is strongly dependent on the variability of fracture aperture [Keller *et al.*, 1999]. This type of dispersion is known as ‘channeling dispersion.’ When channeling exists (with no or few interconnections), velocity variations among the different channels due to the differences in channel width and/or flow resistance give rise to dispersion [Neretnieks, 1983]. Large aperture regions result in significant channeling of the fluid flow, accelerating the movement of solutes in a particular direction, that may differ locally with respect to the main flow direction from high to low piezometric head. This often results in earlier breakthrough than predicted by the conventional parallel plate simplification. Johns and Roberts [1991] indicated that diffusion from the channels to neighboring small aperture regions may be an important contaminant retardation mechanism. For a system of channels with few intersections, Rasmuson [1985] showed that the number of mixing points (points where the channels intermix) that is needed to get a Fickian dispersion is dependent on the fracture aperture distribution, i.e., a wider distribution requires more mixing points. Dispersion may also arise because of varied residence times in different fractures of a fracture network.

Sorption reactions (ion exchange, physical and chemical sorption) often occur at fracture surfaces. Because of sorption, contaminant and colloid breakthrough may be affected by the surface area in contact with the interstitial fluid, surface roughness, and interstitial fluid velocity [Abdel-Salam, 1995]. Attachment of particles onto the fracture matrix may be either reversible or irreversible, depending on the shear forces in the fracture, or upon changes in chemical properties of the interstitial fluid [Grolimund and Borkovec, 1999].

2.2 Physicochemical Characteristics of Colloids

Colloids are very fine particles that range in diameter between 10^{-3} μm and 1 μm [Buddemeier and Hunt, 1988]. Stumm [1977] extended the upper limit of colloids size to approximately 10 μm in diameter. Experiments determining the size of colloids in natural waters show that the colloids are roughly spherical and have a log-normal distribution of diameters [Ledin et al., 1994; Atteia and Kozel, 1997; Lartiges et al., 2001]. A wide variety of micro-organisms, organic and inorganic colloidal material has been found in the subsurface environment. These may include, clay minerals, metal oxides, silicic acid, viruses, bacteria, and organic matter (e.g., humic substances) [Lieser et al., 1990]. The composition of colloids is often chemically similar to that of the immobile subsurface material [McCarthy and Zachara, 1989]. Because a colloid has a high surface area per unit mass, it possesses a high sorptive capacity for contaminants [McDowell-Boyer et al., 1986; Enfield and Bengtsson, 1988; Toran and Palumbo, 1992]. Furthermore, liquid-phase colloids may be more accessible to contaminants than solid surfaces. Chemically, colloids behave differently from dissolved contaminants and are not expected to be affected by the same mechanisms that affect contaminants during migration.

Colloids may be formed in groundwater as a result gradients in geochemical parameters such as pH, ion composition, or CO_2 partial pressure that induce supersaturation to readily precipitable solid phases. Further sources of colloid production in groundwater include leachates from the vadose zone, dissolution of inorganic cementing agents that bind colloid sized materials onto solid surfaces, release and movement of viruses and bacteria, and formation of micelles from the agglomeration of humic acids [McCarthy and Zachara, 1989; Puls et al., 1993]. Additionally, well pumping, rising water tables, and replacement of saline water by fresh water may initiate particle mobilization [Corapcioglu and Jiang, 1993]. When ionic metal species are at concentrations above their solubility limit, colloids may be generated [Buddemeier and Hunt, 1988]. Suspended colloids are also subject to aggregation, filtration, and settling, all of which are relatively complex processes dependent on colloid

density, colloid size, surface chemistry, water chemistry, and interstitial fluid flow rates [McCarthy and Zachara, 1989]. Colloids are found in subsurface waters under various geochemical conditions with concentrations ranging from a few milligrams per liter to a few hundred milligrams per liter [Moulin and Ouzounian, 1992]. For instance, high particle concentrations were found in granitic rock fractures at the Nevada test site (63 mg/l) and in Switzerland (10^{10} particles/l) [Buddemeier and Hunt, 1988; Mills *et al.*, 1991].

The transport of colloids is affected by hydrodynamic interactions between colloidal particles, fracture surfaces, and interstitial flow [Goldman *et al.*, 1967]. The stability of colloids is an important consideration in determining their transport and is controlled by van der Waals attractive forces that promote aggregation, and electrostatic repulsive forces that keep particles apart. When electrostatic repulsions are dominant, especially at low ionic strengths, colloidal particles are electrostatically stabilized and remain in a dispersed state [McCarthy and Zachara, 1989]. Conditions of weak electrostatic repulsive forces may promote coagulation but not necessarily lead to immediate particle immobilization. Coagulation is a function of several variables, including particle concentration and particle size, that can influence the extent of particle–particle collisions. Moreover, destabilized colloids can still be transported as aggregates if the aggregates are sufficiently small relative to the interstitial void space between solid surfaces [McCarthy and Zachara, 1989]. Because of their physicochemical properties, colloids may be transported significant distances from where they were introduced.

The surface charge of colloids is important in modeling their transport and it is sensitive to solution pH [Abelin, 1986]. For every type of colloid there is a pH where the surface charge is zero known as the point of zero charge or the isoelectric point. At this pH, the attractive van der Waals forces start to play a role in particle–particle aggregation. Recall that the velocity distribution in the void space between solid surfaces in subsurface formations (e.g., fracture surfaces) is parabolic, with the maximum velocity along the centerline. Zero–charged colloids will randomly sample, by diffusion, this velocity distribution, but they will not reach the solid surface because their dimensions

physically exclude them from the slowest moving portion of the velocity profile [*de Marsily*, 1986; *Mills et al.*, 1991]. Therefore, the average velocity of non-reactive particles is higher than the mean interstitial fluid velocity, particularly for large size colloids [*Brenner and Edwards*, 1993; *James and Chrysikopoulos*, 1999, 2000]. This phenomenon may be further affected by the ionic strength of solution. For colloids and solid surfaces having the same charge, repulsion effects tend to increase the average velocity of the particles by keeping them away from solid surfaces [*de Marsily*, 1986]. The adsorption process of colloids onto solid surfaces is conventionally termed as sorption, filtration, deposition, retention, or attachment, while colloid desorption is known as detachment. However, if the solution ionic strength increases, repulsive forces decrease, and the attractive van der Waals forces begin to play a role in slowing down or retaining the particles through particle-wall interactions [*de Marsily*, 1986]. For colloids and solid surfaces having opposite charge, sorption mechanisms slow down or filter the colloids [*de Marsily*, 1986]. Generally for charged colloids, particles move more slowly than the average interstitial velocity because of reactions with the fracture matrix [*de Marsily*, 1986].

2.3 Transport and Deposition of Colloids

Recent experimental and field studies indicate that contaminants can migrate not only as dissolved species in the liquid phase, but also adsorbed onto the surface of suspended colloidal particles [e.g., *Chiou et al.*, 1986; *Buddemeier and Hunt*, 1988; *Torok et al.*, 1990]. At the Nevada test site, radionuclide analyses for detonation-cavity samples indicated that substantial fractions of selected nuclides are associated with colloid-sized particles. Colloid particles may serve as carriers for contaminants thereby significantly influencing the net rate of contaminant migration. These results spurred researchers to model colloid-facilitated contaminant transport in subsurface environments [*Grindrod*, 1993; *Abdel-Salam and Chrysikopoulos*, 1995a, b]. *Smith and Degueudre* [1993] modeled the co-transport of a radioactive material in the presence of colloids in a single fracture and showed that depending on system conditions, colloids may either enhance or retard contaminant transport.

In addition to enhancing contaminant transport, certain types of colloids are also hazardous to human health (e.g., supersaturated nuclear species, viruses, microorganisms). *Puls and Powell* [1992] concluded from laboratory experiments that iron oxide colloids may be significantly mobile, and under some conditions these colloids may be transported faster than conservative tracers. In heterogeneous porous formations, colloids are expected to travel faster than conservative tracers (e.g., tritiated water), because colloids bypass small size pores [*Bales et al.*, 1989; *Haber and Brenner*, 1993]. A retardation factor < 1 has been observed in several colloid transport studies [e.g., *Champ and Schroeter*, 1988; *Harvey et al.*, 1989; *Toran and Palumbo*, 1992]. Rapid transport of bacterial colloids, relative to conservative tracers, was observed in a laboratory experiment using a natural fracture [*Bales et al.*, 1989] and in a field experiment in crystalline fractured rocks [*Champ and Schroeter*, 1988]. At two separate sites at Los Alamos, New Mexico, plutonium and americium were detected at distances much further than distances predicted by dual porosity modeling techniques [*Corapcioglu and Jiang*, 1993].

As colloids are transported through fractures, they may be deposited onto fracture surfaces. A field experiment in crystalline rock fractures has demonstrated that the primary removal mechanism of bacterial and non-reactive colloids from solution is deposition [*Champ and Schroeter*, 1988]. Deposition of colloidal particles is generally considered to involve two processes: transport of particles to the solid-liquid interface which is primarily controlled by Brownian motion for sub-micron particles; and attachment of particles to fracture surfaces that is mainly affected by the repulsive electric double layer, the attractive van der Waals forces, and viscous interaction [*Bowen and Epstein*, 1979; *Mills et al.*, 1991]. Particle deposition is also affected by particle shape, wall roughness and whether fracture surfaces are clean or if deposition occurs on previously collected particles [*Chrysikopoulos and Abdel-Salam*, 1997]. Comprehensive compilations of particle deposition mechanisms have been presented by *McDowell-Boyer et al.* [1986] and *McCarthy and Zachara* [1989]. The kinetics of local adsorption of colloid particles in parallel plate systems have been studied

in depth [e.g., *Adamczyk and van de Ven*, 1980; *Adamczyk et al.*, 1983, 1991, 1992a, b, 1997]. Particle deposition may be represented mathematically by an empirical coefficient (filter or deposition coefficient), that is often considered an irreversible adsorption term accounting for the mechanisms governing the deposition process [*Schaaf and Talbot*, 1989; *Chrysikopoulos and Abdel-Salam*, 1997]. Because the deposition coefficient depends on the absolute temperature, the viscosity of the aqueous medium, the average particle size, and other parameters accounting for the electric double layer and van der Waals forces, it is usually determined from laboratory columns or field experimental measurements [e.g., *Champ and Schroeter*, 1988; *Toran and Palumbo*, 1992].

Detachment of colloids is not expected in fractured rocks where flow velocities are low, and *Bowen and Epstein* [1979] have shown experimentally that the rate of release of deposited colloids from a smooth parallel plate channel is negligible when the aqueous geochemistry of the interstitial fluid is constant. However, several studies have indicated that high fluid shear or changes in the chemistry of the interstitial fluid may allow for the resuspension of previously deposited colloids [*Grolimund and Borkovec*, 1999; *Lægdsmand et al.*, 1999; *Bergendahl and Grasso*, 2000]. Further, some studies of colloid transport in fractures suggest that colloids do not penetrate low porosity rock matrices [*Bowen and Epstein*, 1979]. For instance, *Bradbury and Green* [1986] reported that particles in the size range of 0.091–0.312 μm do not penetrate a crystalline rock matrix with 0.14 μm micro-fissures. Because the size of colloids ranges between 10^{-3} to 10 μm and the size of matrix micro-fissures ranges between 10^{-2} to 10 μm , the possibility of colloids diffusing into the rock matrix can not be eliminated.

2.4 Boundary Conditions

In any modeling process, boundary conditions are important because they account for effects of the system outside of the region of interest. Usually, contaminant transport models assume that mass is introduced to the system through either a constant concentration (first-type or Dirichlet)

or a constant flux (third-type or Cauchy) inlet boundary condition [van Genuchten and Alves, 1982]. The constant concentration boundary condition represents the case where colloids exist at the inlet boundary at a prescribed concentration (this includes instantaneous or pulse injection), while the constant flux boundary condition represents the case where colloids are added at a constant rate to the fluid that enters the fracture. The constant concentration boundary condition indicates that with steady velocity, the advective flux across the boundary is constant, while the constant flux indicates that the sum of advective and dispersive fluxes is constant. Solutions resulting from both boundary conditions can be used in the analysis of experimental breakthrough curves obtained by injecting colloids into a rock fracture.

2.5 Particle Tracking

With the ever expanding capabilities of computers, particle tracking solutions to various engineering problems are becoming increasingly complex and realistic. Although random walk methods, Monte Carlo simulations, and Fokker–Planck solutions to differential equations have been employed for many years [Ahlstrom *et al.*, 1977], the availability of inexpensive high speed processors and vast memory storage has allowed the application of these solution techniques to increasingly complex problems [e.g., Uffink, 1989; Valocchi and Quinodoz, 1989; Yamashita and Kimura, 1990; Kitanidis, 1994; Grindrod and Lee, 1997; Lu, 2000; Liu *et al.*, 2000; Michalak and Kitanidis, 2000]. Although particle tracking techniques were originally applied to contaminant transport in porous media [e.g., Thompson and Gelhar, 1990; Thompson and Dougherty, 1992; Thompson, 1993; Thompson *et al.*, 1996], extensions to fractured media have been made. For example, particle tracking schemes that model the transport of colloids in both uniform [Yamashita and Kimura, 1990; James and Chrysikopoulos, 1999] and variable aperture fractures [Reimus, 1995; Grindrod and Lee, 1997; James and Chrysikopoulos, 2000; Tsang and Tsang, 2001] as well as fracture networks [Liu *et al.*, 2000] have been developed. James and Chrysikopoulos [2001a, b] have also compared

a traditional particle tracking algorithm with analytical solutions for the ideal case of polydisperse colloid transport in a uniform fracture and excellent agreement was shown supporting the validity of particle tracking techniques as solution methods for the transport of colloids and contaminants in fractures. Higher order particle tracking schemes have been devised; however, they were found to only be useful in heterogeneous systems with complicated unsteady flow fields [*Bensabat et al.*, 2000].

Chapter 3

Effective Parameters for a Colloid Plume

In this chapter expressions for the effective velocity and effective dispersion coefficient for a plume of finitely sized spherical particles with neutral buoyancy flowing within a water saturated fracture are derived. Consider the miscible displacement of a fluid initially free of particles by another fluid containing suspended particles of finite size within a fracture formed by two semi-infinite parallel plates. A parabolic velocity profile is induced by a uniform longitudinal pressure gradient and the no slip condition at the fracture walls with maximum fluid velocity maintained along the fracture centerline. Particle spreading occurs due to the combined actions of molecular diffusion and the dispersive effect of the velocity gradient. Unlike the derivation for the Taylor dispersion coefficient, here the finite size of the particles is taken into account. It is shown that because the finite size of a particle excludes it from the slowest moving portion of the velocity profile, the effective particle velocity is increased, while the overall particle dispersion is reduced.

3.1 Background

It is often assumed that the solutes are infinitesimally small and that axial advection and transverse diffusion chiefly govern contaminant fate and transport in fractures. While it is true that many contaminants are of molecular size, this is not always the case. Many studies have shown colloids to be ubiquitous in groundwater, often having a high affinity for contaminant sorption [*Smith and Degueudre, 1993; Contardi et al., 2001*]. Essentially, if a contaminant sorbs onto a colloid, the colloid itself becomes a contaminant with transport properties different than the soluble contaminant [*Abdel-Salam and Chrysikopoulos, 1995a, b*].

It is well known that for a viscous fluid flowing in a channel, a velocity profile exists such that the velocity of the fluid is maximum along the centerline and diminishes toward the wall. A colloidal particle injected into such a channel will, by Brownian motion, make transverse excursions normal to the direction of the flow thereby sampling and adopting velocities across the channel. The mean velocity of the particle will therefore be a reflection of the velocity profile of the interstitial fluid with the important qualification that the center of a particle will be excluded from the slowest streamlines closest to the fracture walls because of its size [*Small, 1974*]. Consequently, the particle will move through the channel with a mean velocity greater than the mean fluid velocity by a factor that increases with increasing ratio of particle size to fracture aperture. This change in effective particle velocity also alters the effective dispersion coefficient of the particle plume if the analysis made by *Taylor [1953]* is performed with the modified particle velocity used in place of the mean fluid velocity.

In this chapter, the effective velocity and effective dispersion coefficient for finitely sized spherical colloidal particles with neutral buoyancy are derived from first principles. Because the finite size of a particle excludes it from the slowest moving portion of the velocity profile near the walls of a fracture, it is shown that the effective velocity of a particle plume is greater than the mean interstitial fluid velocity. Furthermore, this particle size exclusion leads to a decrease in the effective dispersion coefficient of a particle plume.

3.2 Mathematical Derivations

3.2.1 Effective Velocity

Assume that a fully developed, unidimensional, Poiseuille velocity distribution exists within a fracture as shown in Figure 3.1, expressed as [Fox and McDonald, 1992, p. 392],

$$u_x(z) = U_{\max} \left[1 - 4 \left(\frac{z}{b} \right)^2 \right]. \quad (3.1)$$

The mean fluid velocity may be expressed as

$$\begin{aligned} \bar{U} &= \frac{1}{b} \int_{-\frac{b}{2}}^{\frac{b}{2}} u_x(z) dz \\ &= \frac{2}{3} U_{\max}, \end{aligned} \quad (3.2)$$

where U_{\max} is the maximum velocity of the interstitial fluid along the centerline of the fracture; and z is the coordinate direction perpendicular to the walls of the fracture with its origin at the center of the fracture. It is assumed that a spherical particle travels with a velocity corresponding to the local flow velocity at its centroid. Particle-wall overlap is not allowed. Hydrodynamic, gravitational, van der Waals, and electrostatic forces are not considered in the calculation of particle velocity. The upper limit of the Reynolds number for colloid sized particles flowing in fractured media is below 10^{-3} , well into the Stokes flow regime. Drag and lift forces may be neglected. The average (or effective) velocity of a particle is estimated by integrating the Poiseuille velocity distribution over the aperture available to a particle and dividing by that same available aperture. The available aperture is considered as the original aperture, b , less the diameter of a particle, d_p . Because particle penetration of the fracture wall is not permitted, the finite size of a particle does not allow it to sample the slowest moving portion of the velocity profile nearest the wall. This size exclusion leads to an effective particle velocity given by:

$$\begin{aligned} U_{\text{eff}} &= \frac{U_{\max}}{b - d_p} \int_{-\frac{b-d_p}{2}}^{\frac{b-d_p}{2}} \left[1 - 4 \left(\frac{z}{b} \right)^2 \right] dz \\ &= \frac{2}{3} U_{\max} \left[1 + \frac{d_p}{b} - \frac{1}{2} \left(\frac{d_p}{b} \right)^2 \right]. \end{aligned} \quad (3.3)$$

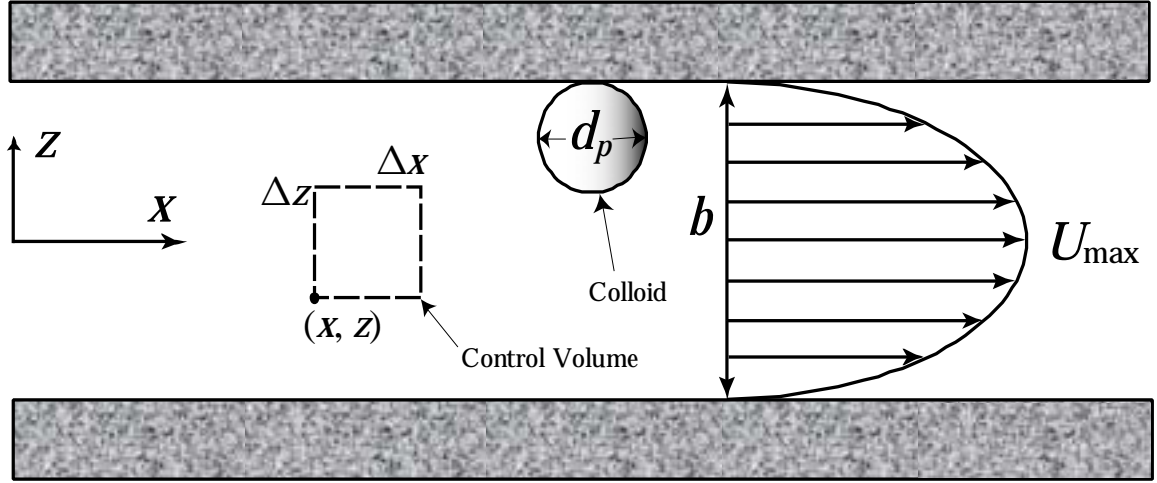


Figure 3.1: Schematic illustration of the fracture considered in this study.

Note that the effective particle velocity (3.3) is greater than the mean fluid velocity (3.2) because the particle diameter may not be larger than the fracture aperture ($d_p/b < 1$). In view of (3.3) it is evident that the effective velocity of a particle increases with increasing particle diameter.

3.2.2 Effective Dispersion Coefficient

Consider a control volume of unit depth defined as $\Delta x \Delta z$ and situated in a fracture of aperture b as shown in Figure 3.1. Conservation laws require that net mass accumulation of suspended particles be equal to the difference between mass entering and exiting the control volume as follows:

$$\frac{\partial (n_{d_p} V)}{\partial t} = \left(\dot{\mathcal{N}}_{\text{in}} - \dot{\mathcal{N}}_{\text{out}} \right)_{\text{diffusion}}^{\text{transverse}} + \left(\dot{\mathcal{N}}_{\text{in}} - \dot{\mathcal{N}}_{\text{out}} \right)_{\text{advection}}^{\text{axial}} \quad (3.4)$$

where n_{d_p} is the number concentration of colloid particles; $\dot{\mathcal{N}}$ is the time rate of change of the number of colloids; $V = \Delta x \Delta z$ is the two-dimensional control volume per unit depth; and t is time. Transport by axial diffusion is neglected in (3.4) as it is small in comparison to that by axial advection. This assumption was initially made by *Taylor* [1953] as well as *Aris* [1956]; however, *Berkowitz and Zhou* [1996] proved it to be a reasonable approximation for all but small time.

Using a truncated Taylor series expansion around an arbitrary position x , i.e., $f(x + \Delta x) = f(x) + \Delta x f'(x) + \dots$, for the axial advection term yields:

$$\dot{\mathcal{N}}_{\text{in}} = A u_x(z) n_{d_p}, \quad (3.5)$$

$$\dot{\mathcal{N}}_{\text{out}} = A \left[u_x(z) n_{d_p} + \frac{\partial u_x(z) n_{d_p}}{\partial x} \Delta x \right], \quad (3.6)$$

where $A = \Delta z$ is the unit depth cross-sectional area available for axial advection within the control volume. Similarly, using a truncated Taylor series expansion around an arbitrary position z for the transverse diffusion term leads to:

$$\dot{\mathcal{N}}_{\text{in}} = \Delta x J_z, \quad (3.7)$$

$$\dot{\mathcal{N}}_{\text{out}} = \Delta x \left(J_z + \frac{\partial J_z}{\partial z} \Delta z \right), \quad (3.8)$$

where J_z is the flux term evaluated at z that is assumed to approximate a Fickian diffusion process as

$$J_z = -\mathcal{D}_{d_p} \frac{\partial n_{d_p}}{\partial z}, \quad (3.9)$$

where \mathcal{D}_{d_p} is the molecular diffusion coefficient of a particle with diameter d_p , from the Stokes–Einstein diffusion equation:

$$\mathcal{D}_{d_p} = \frac{kT}{3\pi\mu d_p}, \quad (3.10)$$

where k is Boltzmann’s constant; and T is the absolute temperature, and μ the dynamic viscosity of the interstitial fluid, respectively.

Substituting (3.5)–(3.8) into (3.4) and dividing by V yields the following partial differential equation

$$\frac{\partial n_{d_p}(x, z, t)}{\partial t} = \mathcal{D}_{d_p} \frac{\partial^2 n_{d_p}(x, z, t)}{\partial z^2} - u_x(z) \frac{\partial n_{d_p}(x, z, t)}{\partial x}. \quad (3.11)$$

The preceding equation is the two-dimensional, unsteady, advection–diffusion equation with axial advection and transverse diffusion as the two governing transport mechanisms.

Because in the present derivation the molecular diffusion in the axial direction is neglected, all axial particle movement is due to advection. A steady–state assumption is made by considering

only advection across the plane moving with the center of mass of a colloid particle plume, such that x and t may be collapsed into a single coordinate so that the transient term in (3.11) may be eliminated. This can be achieved by the following coordinate transformation

$$\xi = x - U_{\text{eff}}t. \quad (3.12)$$

Applying the preceding coordinate transformation to (3.11) yields the following partial differential equation

$$\mathcal{D}_{d_p} \frac{\partial^2 n_{d_p}(\xi, z)}{\partial z^2} = [u_x(z) - U_{\text{eff}}] \frac{\partial n_{d_p}(\xi, z)}{\partial \xi}, \quad (3.13)$$

where the term $u_x(z) - U_{\text{eff}} = u_\xi(z)$ is termed the ‘velocity defect’, defined as the velocity that is a function of z at a point $\xi = 0$ that follows the first moment of a particle plume in time. Subtracting the effective velocity (3.3) from the Poiseuille (parabolic) velocity profile (3.2) yields

$$\begin{aligned} u_\xi(z) &= u_x(z) - U_{\text{eff}} \\ &= \frac{U_{\text{max}}}{3} \left[\left(1 - \frac{d_p}{b}\right)^2 - 12 \left(\frac{z}{b}\right)^2 \right]. \end{aligned} \quad (3.14)$$

Figure 3.2 is an illustration of the velocity defect. Note that particles in the shaded regions have a tendency to diffuse in the direction of the open arrows because of the concentration gradient induced by the ‘velocity defect’. It is in these shaded regions where axial particle advection (indicated by the filled arrows) and transverse particle diffusion (indicated by the open arrows) are important. With respect to the moving frame of reference, the velocity of a particle that is in contact with the wall becomes $u_\xi(\pm(b - d_p)/2) = -(2/3)U_{\text{max}}(1 - d_p/b)^2$. Consequently, the apparent velocity of the particles in the shaded areas to the left of the moving frame of reference is negative as indicated by the direction of the filled arrows. Because the mean particle velocity at the plane for which $\xi = 0$ is zero, the transfer of particles across this plane depends only on the transverse variation of n_{d_p} . In view of (3.14), the governing equation (3.13) can be expressed as

$$\frac{\partial^2 n_{d_p}(\xi, z)}{\partial z^2} = \frac{U_{\text{max}}}{3\mathcal{D}_{d_p}} \left[\left(1 - \frac{d_p}{b}\right)^2 - 12 \left(\frac{z}{b}\right)^2 \right] \frac{\partial n_{d_p}(\xi, z)}{\partial \xi}. \quad (3.15)$$

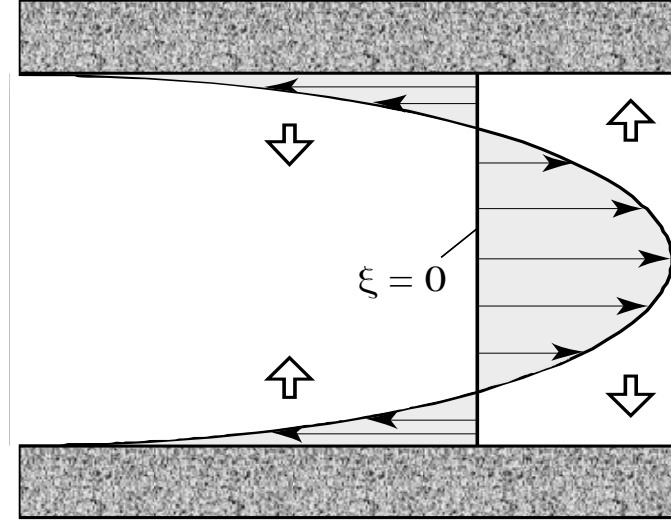


Figure 3.2: Schematic illustration of the ‘velocity defect’ represented by the shaded areas. Filled arrows indicate axial advection of particles and open arrows indicate transverse molecular diffusion of particles.

Employing the assumption that transverse concentration gradients induced by axial advection are quickly smoothed out by transverse molecular diffusion [Taylor, 1953], the rate of change of the particle number concentration with respect to the moving frame of reference may be assumed nearly constant across the aperture of the fracture. This assumption implies that $\partial n_{d_p}(\xi, z)/\partial \xi$ may be replaced with $\partial n_{d_p}(\xi)/\partial \xi$. Integration of (3.15) with respect to z yields

$$\frac{\partial n_{d_p}(\xi, z)}{\partial z} = \frac{U_{\max} b}{3D_{d_p}} \left[\left(1 - \frac{d_p}{b}\right)^2 \frac{z}{b} - 4 \left(\frac{z}{b}\right)^3 \right] \frac{\partial n_{d_p}(\xi)}{\partial \xi} + C(\xi), \quad (3.16)$$

where $C(\xi)$ is an integration constant. Applying the non-dispersive flux boundary condition across the centerline ($z = 0$), because of the neutral particle buoyancy, indicates that the integration constant vanishes:

$$\left. \frac{\partial n_{d_p}(\xi, z)}{\partial z} \right|_{z=0} = 0 \Rightarrow C(\xi) = 0. \quad (3.17)$$

Integration of (3.16) with respect to z yields

$$n_{d_p}(\xi, z) = \frac{U_{\max} b^2}{6\mathcal{D}_{d_p}} \left[\left(1 - \frac{d_p}{b}\right)^2 \left(\frac{z}{b}\right)^2 - 2 \left(\frac{z}{b}\right)^4 \right] \frac{\partial n_{d_p}(\xi)}{\partial \xi} + n_{cl}(\xi), \quad (3.18)$$

where $n_{cl}(\xi)$ is an integration constant. It can be shown by evaluating $n_{d_p}(\xi, 0)$ that $n_{cl}(\xi)$ is actually the particle concentration at the centerline of the fracture.

The average particle concentration in the z -direction over the entire fracture aperture is defined by integrating the particle number concentration across the fracture and dividing by the fracture aperture

$$\bar{n}_{d_p}(\xi) = \frac{1}{b} \int_{-b/2}^{b/2} n_{d_p}(\xi, z) dz. \quad (3.19)$$

Substituting (3.18) into (3.19) and performing the integration, the average colloid concentration is expressed as:

$$\bar{n}_{d_p}(\xi) = \frac{U_{\max} b^2}{6\mathcal{D}_{d_p}} \left[\frac{7}{120} - \frac{1}{6} \frac{d_p}{b} + \frac{1}{12} \left(\frac{d_p}{b}\right)^2 \right] \frac{\partial \bar{n}_{d_p}(\xi)}{\partial \xi} + n_{cl}(\xi). \quad (3.20)$$

Note that due to averaging over b , the term $\partial n_{d_p}(\xi)/\partial \xi$ is replaced by $\partial \bar{n}_{d_p}(\xi)/\partial \xi$. Solving (3.20) for $n_{cl}(\xi)$ and substituting the resulting expression into (3.18) allows $n_{d_p}(\xi, z)$ to be presented only in terms of the average concentration across the fracture as follows:

$$n(\xi, z) = \frac{U_{\max} b^2}{6\mathcal{D}_{d_p}} \left[-\frac{7}{120} + \frac{1}{6} \frac{d_p}{b} - \frac{1}{12} \left(\frac{d_p}{b}\right)^2 + \left(1 - \frac{d_p}{b}\right)^2 \left(\frac{z}{b}\right)^2 - 2 \left(\frac{z}{b}\right)^4 \right] \frac{\partial \bar{n}_{d_p}(\xi)}{\partial \xi} + \bar{n}(\xi). \quad (3.21)$$

To evaluate the effective dispersion coefficient, an expression for the flux of particles across a plane that is moving with the first moment of a particle plume in time is sought. The average flux of particles in the axial direction relative to the moving coordinate, ξ , is given by

$$\begin{aligned} \bar{J} &= \frac{1}{b - d_p} \int_{-\frac{b+d_p}{2}}^{\frac{b-d_p}{2}} n_{d_p}(\xi, z) u_{\xi}(z) dz \\ &= -\frac{2}{945} \frac{U_{\max}^2 b^2}{\mathcal{D}_{d_p}} \left(1 - \frac{d_p}{b}\right)^6 \frac{\partial \bar{n}_{d_p}(\xi)}{\partial \xi}, \end{aligned} \quad (3.22)$$

where the latter transformation is a consequence of employing (3.14) and (3.21). The average flux is calculated only for the portion of the fracture available to the particles, hence the region spanned by the limits of integration.

Using the effective velocity as a moving frame of reference, the transport of particles within the fracture may be viewed as a dispersion problem. Consequently, the advection–diffusion equation may now be redefined as Fick’s second law of diffusion along the moving frame of reference, ξ , with diffusion coefficient D_{eff} . Thus, the unsteady transport of particles is expressed through use of the continuity equation assuming there is no particle generation, as follows [Bird *et al.*, 1960, p. 555]

$$\frac{\partial \bar{n}_{d_p}(\xi)}{\partial t} = -\frac{\partial \bar{J}}{\partial \xi}. \quad (3.23)$$

Substituting the expression for average particle flux (3.22) into the preceding equation yields

$$\frac{\partial \bar{n}_{d_p}(\xi)}{\partial t} = D_{\text{eff}} \frac{\partial^2 \bar{n}(\xi)}{\partial \xi^2}, \quad (3.24)$$

where the effective dispersion coefficient, D_{eff} , represents the apparent particle spreading arising from the combined effect of the advective flux of particles across the plane moving with the center of mass of a particle plume plus the particle molecular diffusion, and it is defined as

$$D_{\text{eff}} = \mathcal{D}_{d_p} + \frac{2}{945} \frac{U_{\text{max}}^2 b^2}{\mathcal{D}_{d_p}} \left(1 - \frac{d_p}{b}\right)^6. \quad (3.25)$$

For the limiting case where a particle becomes negligibly small, $d_p \rightarrow 0$, the preceding expression for the effective dispersion coefficient for finitely sized particles reduces to the classic Taylor dispersion coefficient

$$D_{\text{Taylor}} = \mathcal{D}_{d_p} + \frac{2}{945} \frac{U_{\text{max}}^2 b^2}{\mathcal{D}_{d_p}}. \quad (3.26)$$

3.3 Discussion

The effect of finite particle size on particle transport in a water saturated, uniform aperture fracture is examined in this section by focusing on the limiting cases where the particle diameter becomes infinitesimally small ($d_p \rightarrow 0$) as well as when the particle diameter is comparable to the fracture aperture ($d_p \rightarrow b$). As the diameter of a particle becomes infinitesimally small, the effective velocity with which the particle plume travels is reduced to the mean flow velocity, $U_{\text{eff}} = \frac{2}{3}U_{\text{max}}$.

Furthermore, the effective dispersion coefficient of a plume of small particles reduces to the Taylor dispersion coefficient. This is in agreement with the assumption of an infinitesimally small solute made by Taylor in his derivation. At the limit of the particle diameter approaching the fracture aperture, the effective velocity of a particle plume becomes U_{\max} while the corresponding effective dispersion coefficient reduces to the molecular diffusion coefficient. Both results arise directly from the assumptions that each particle travels with a velocity equal to that found at its centroid due to the existing hydraulic gradient and that particle-wall overlap is not permitted. If a particle is nearly equal in size to the aperture of the fracture, it will experience only a narrow range of velocities close to U_{\max} thereby decreasing the dispersive effect of the velocity gradient. If a particle only experiences a single velocity, the dispersion of a particle plume is caused by molecular diffusion alone. The expected behavior of D_{eff} at both limits of small and large particles is evident from (3.25).

Figure 3.3a compares the effective velocity for a monodisperse plume of finitely sized particles calculated from (3.3) to the mean fluid velocity calculated from (3.2). Figure 3.3b compares the effective dispersion coefficient for a monodisperse plume of finitely sized particles calculated from (3.25) to the Taylor dispersion coefficient calculated from (3.26). Particle diameters range from 0.1% up to one-quarter of the fracture aperture. It should be noted that the molecular diffusion coefficient used in both the effective and Taylor dispersion coefficients was calculated from (3.10) even though the Taylor dispersion coefficient is derived for infinitesimally small particles. It is evident from Figure 3.3 that when the particle diameter is 6.5% of the fracture aperture, the effective dispersion coefficient of a particle plume is 50% less than the corresponding Taylor dispersion coefficient. Therefore, accounting for the finite size of a particle increases the effective velocity and decreases the dispersion of a particle plume within a fracture. Clearly, the findings in this work suggest that for the transport of finitely sized particles through a water saturated fracture particle size should be taken into account.

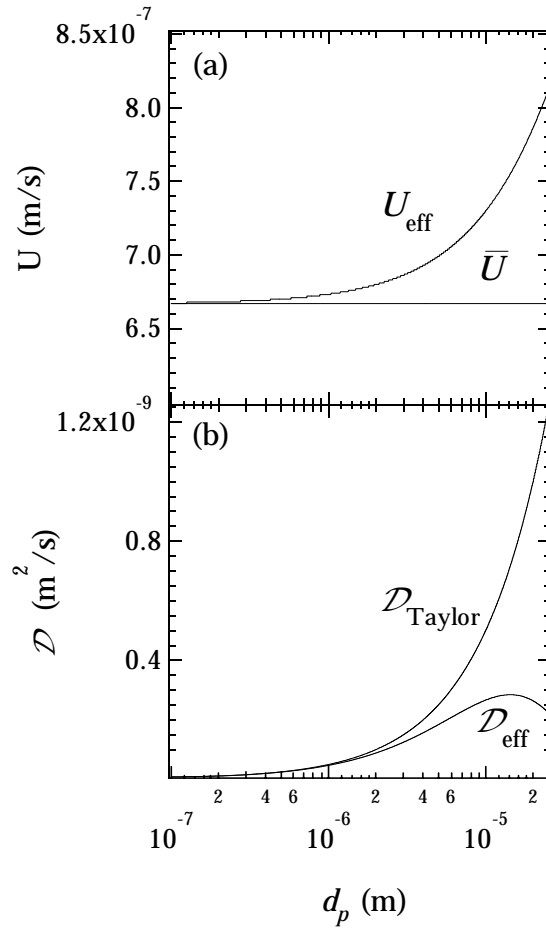


Figure 3.3: Effective parameters for finitely sized particles of diameter, d_p . The effective and mean velocities are compared in (a); and (b) compares the effective and Taylor dispersion coefficients as a function of particle size (here $b = 1 \times 10^{-4}$ m, $U_{\text{max}} = 1 \times 10^{-6}$ m/s, and $T = 288.15$ K).

3.4 Summary

In this chapter an effective velocity (3.3) and an effective dispersion coefficient (3.25) for finitely sized, spherical, particles traveling in a uniform aperture fracture are derived. The slowly flowing carrier fluid forms a parabolic velocity profile within the fracture. Because particle-wall overlap is not allowed, and because a particle is assumed to flow at a velocity equal to that found at its centroid, the size of a particle physically excludes it from the slowest moving portion of the velocity profile located at the fracture walls. While this size exclusion serves to increase the effective

travel velocity of a particle plume, it also decreases its effective dispersion coefficient. The effective dispersion coefficient derived here is found to be similar in form to the Taylor dispersion coefficient. In fact, in the limit of a particle diameter becoming infinitesimally small, the newly derived effective dispersion coefficient reduces to the classic Taylor dispersion coefficient. The results presented in this chapter show that the finite size of a particle does in fact increase the effective plume velocity and decreases the overall spreading of a particle plume.

Chapter 4

Analytical Solutions

Analytical solutions are derived in this chapter that describe the transport of finitely sized monodisperse and polydisperse particles of neutral buoyancy within a semi-infinite, uniform fracture subject to several boundary and initial conditions. The transport of one monodisperse and three polydisperse particle plumes composed of hard spherical particles with equivalent mean but different log-normally distributed diameters is investigated. Instantaneous as well as continuous particle injection are examined. Both reversible and irreversible particle-wall interactions are considered. It is shown that both the finite particle size and the characteristics of the particle diameter distribution significantly affect the shape of the particle concentration breakthrough curves. Furthermore, increasing the standard deviation of the particle diameter enhances particle spreading and increases the number of sorbed particles when particle-wall interactions are taken into account. Excellent agreement between available experimental data and the analytical solution for the case of an instantaneous release of monodisperse particles in a natural fracture is observed.

4.1 Background

The governing partial differential equations for transport in a fracture are linear with respect to the dependent variable (i.e., particle concentration). Therefore, analytical solutions to polydisperse particle transport in a fracture can be derived from the corresponding analytical solutions to monodisperse particle transport through use of the superposition principle. In the present study, four cases are considered. The first case represents an instantaneous release of particles into a fracture without particle–wall reactions. In the second case, it is assumed that a constant concentration of particles is present at the fracture inlet and that particles do not interact with the walls of the fracture. In both of these cases, the appropriate governing equation is of a form amenable to a straightforward analytical solution. The third and fourth cases examined correspond to a constant concentration of particles at the fracture inlet, but with irreversible and reversible particle attachment onto the fracture walls, respectively. It should be noted that the analytical solutions for polydisperse particles presented in this chapter are applicable to any distribution of particle sizes, but model simulations are presented here for one monodisperse and three log–normal polydisperse distributions.

4.2 Development of Models

4.2.1 Governing Transport Equations

Consider the miscible displacement of a fluid initially free of particles by another fluid containing suspended particles of neutral buoyancy within a fracture formed by two semi–infinite parallel plates of unit depth as shown in Figure 3.1. The governing equations for particle transport in a uniform fracture accounting for advection, diffusion, and particle accumulation at the fracture walls are given by:

$$\frac{\partial n_{d_p}(x, z, t)}{\partial t} = \mathcal{D}_{d_p} \left[\frac{\partial^2 n_{d_p}(x, z, t)}{\partial x^2} + \frac{\partial^2 n_{d_p}(x, z, t)}{\partial z^2} \right] - u_x(z) \frac{\partial n_{d_p}(x, z, t)}{\partial x}, \quad (4.1)$$

$$\frac{\partial n_{d_p}^*(x, t)}{\partial t} = -\mathcal{D}_{d_p} \frac{\partial n_{d_p}(x, \pm b/2, t)}{\partial z}, \quad (4.2)$$

where n_{d_p} is the temporally and spatially varying number density (concentration) of particles with diameter d_p ; $n_{d_p}^*$ is the time and space dependent number of sorbed particles per unit surface area of the fracture wall; and $u_x(z)$ is the local interstitial fluid velocity. A fully developed Poiseuille velocity distribution exists within the fracture defined in Chapter 3 by equation (3.2) and the molecular diffusion coefficient of a spherical particle was defined by equation (3.10). Furthermore, it is assumed that the fluid density and dynamic viscosity are constant and that gravitational effects as well as particle–particle interactions are negligible. The coupled differential equations (4.1) and (4.2) take into account the relationship between suspended colloids within the fracture and colloids attached onto the fracture surface.

The formulation of equations (4.1) and (4.2) is quite general and, depending on boundary and initial conditions, not amenable to an exact analytical solution. In subsequent sections, analytical solutions to various simplified versions of (4.1) and (4.2) subject to appropriate boundary and initial conditions specific to each case considered will be derived.

4.2.2 Transport Parameters for Finitely Sized Particle Plumes

4.2.2.1 Non-sorbing or Reversibly Sorbing Particles

In this work it is assumed that a hard spherical particle of neutral buoyancy travels with a velocity corresponding to the flow velocity at its centroid due to the existing hydraulic gradient. It should be noted that hydrodynamic, gravitational, van der Waals, and electrostatic forces are not included in the calculation of particle velocity. Particles are not allowed to penetrate the fracture walls. Because the finite size of a particle does not allow it to sample the slowest moving portion of the velocity profile nearest the wall, the effective velocity of a particle plume is greater than the mean fluid velocity. The effective velocity of a particle plume was derived in Chapter 3 and given by (3.3) and it is evident that the effective velocity of a particle plume increases with increasing particle diameter ($d_p/b < 1$).

Following Taylor–Aris procedures, it is assumed that the only contributors to particle dispersion in a fracture are the fully developed Poiseuille flow in the axial direction, transverse diffusion, and particle–wall surface reactions. Although the parabolic velocity profile creates fluid shear in the z -direction, solutions for particle number concentrations derived here are independent of z because the average particle concentration at a given axial location within a fracture is determined by integrating the particle concentration across the local aperture of the fracture. Consequently, particle plume movement resembles plug flow. The difference between a parabolic velocity profile and plug flow conditions on particle transport lies in the spreading of the particles. Under plug flow conditions, the molecular diffusion coefficient may be orders of magnitude smaller than the effective dispersion coefficient.

The Taylor dispersion coefficient of a non–reactive solute in a uniform fracture was given by equation (3.26). As described in Chapter 3, a modified form of the Taylor dispersion coefficient must be used for finitely sized particles. The effective dispersion coefficient for a plume of particles with diameter d_p was given by (3.25) where it was shown that increasing the particle diameter decreases the overall dispersion of the plume.

4.2.2.2 Irreversibly Sorbing Particles

Effective parameters for solute transport in cylindrical tubes and ideal fractures subject to irreversible sorption have been derived in numerous works [*Sankarasubramanian and Gill, 1974; Johns and DeGance, 1975; Berkowitz and Zhou, 1996; Dijk and Berkowitz, 1998*]. In this section effective parameters appropriate for the transport of finitely sized particles undergoing irreversible sorption at the fracture walls are presented.

The first–order effective decay coefficient arising from irreversible solute attachment at the fracture walls is derived in Appendix D as:

$$K_{\text{eff}} = \frac{12\mathcal{D}_{d_p}}{b^2} \frac{Da}{6 + Da}, \quad (4.3)$$

where Da is the dimensionless Damköhler number measuring the ratio of the tendency for reaction to the tendency for diffusive transport, defined as [Butt, 1980, p. 377]

$$Da = \frac{k_f b}{\mathcal{D}_{d_p}}, \quad (4.4)$$

where k_f is the forward sorption rate constant.

The mean velocity of an irreversibly sorbing solute in a fracture is derived in Appendix D and is modified here to account for finitely sized particles by employing (3.3). The resulting effective velocity for a plume of finitely sized particles undergoing irreversible sorption at the fracture walls is given as

$$U_{\text{eff}} = \frac{2}{3} U_{\text{max}} \left[1 + \frac{d_p}{b} - \frac{1}{2} \left(\frac{d_p}{b} \right)^2 + \frac{3}{10} \frac{Da}{6 + Da} \right]. \quad (4.5)$$

Colloid reactions with fracture walls lead to a depletion of particles in the slower moving portion of the velocity profile resulting in a distribution of suspended particles weighted in favor of those particles present in the faster moving region of the flow profile. Thus, suspended particles are advected at a velocity greater than the effective velocity observed in the absence of particle sorption.

The dispersion coefficient for an irreversibly sorbing solute traveling within a water saturated fracture with uniform aperture is derived in Appendix D. Substitution of the preceding equation into the dispersion coefficient for an irreversibly sorbing solute plume leads to the following effective dispersion coefficient for a plume of finitely sized particles undergoing irreversible sorption at the fracture walls:

$$D_{\text{eff}} = \mathcal{D}_{d_p} + \frac{2}{945} \frac{U_{\text{max}}^2 b^2}{\mathcal{D}_{d_p}} \left[\left(1 - \frac{d_p}{b} \right)^6 - \frac{7}{10} \frac{Da}{6 + Da} \right]. \quad (4.6)$$

From the preceding relationship it is evident that increasing Da serves to decrease particle spreading in a fracture. Note that if $Da = 0$ (no wall reaction or $k_f = 0$), then (4.5) and (4.6) reduce to (3.3) and (3.25), respectively.

4.3 Analytical Solutions

4.3.1 Instantaneous Injection Without Particle Sorption

4.3.1.1 Monodisperse Particle Plume

Consider the case where a known number of monodisperse particles are released instantaneously within a uniform, water saturated, fracture. Assuming that there are no particle–wall interactions, the governing equation (4.1) is eliminated from the model formulation. It is assumed that the concentration of colloids in the z –direction is uniform, equal to the average colloid concentration across the fracture aperture and determined by:

$$\bar{n}_{d_p}(x, t) = \frac{1}{b} \int_{-\frac{b}{2}}^{\frac{b}{2}} n_{d_p}(x, z, t) dz. \quad (4.7)$$

As in Chapter 3, the two–dimensional form of the advection–diffusion equation (4.1) may be simplified through a transformation of coordinates. A steady state assumption is made by considering only advection across the plane moving with the center of mass of a particle distribution, such that x and t may be collapsed into a single coordinate and the transient term in (4.1) may be eliminated. Let $\xi = x - U_{\text{eff}}t$ represent the distance along the fracture from a fluid parcel traveling with velocity equal to the effective velocity of a particle plume, U_{eff} , at time, t . Following Chapter 3, application of this transformation yields, after some manipulation, the familiar unsteady dispersion equation [James and Chrysikopoulos, 2001b]:

$$\frac{\partial \bar{n}_{d_p}(\xi, t)}{\partial t} = D_{\text{eff}} \frac{\partial^2 \bar{n}_{d_p}(\xi, t)}{\partial \xi^2}, \quad (4.8)$$

where D_{eff} defined by (3.25) describes the spreading of the plume with respect to the moving coordinate ξ . For an instantaneous injection of monodisperse particles at the inlet of a semi–infinite fracture, the appropriate boundary and initial conditions are:

$$\bar{n}_{d_p}(0, t) = 0, \quad (4.9)$$

$$\bar{n}_{d_p}(\infty, t) = 0, \quad (4.10)$$

$$\bar{n}_{d_p}(\xi, 0) = n_o \delta(\xi), \quad (4.11)$$

where n_o represents the initial number of monodisperse particles injected into the fracture per cross-sectional area of the fracture (plane source); and $\delta(\xi)$ is the Dirac delta function. The combination of boundary and initial conditions (4.9) and (4.11) describe an instantaneous release of colloids. Boundary condition (4.10) states that the fracture system is semi-infinite and the concentration of particles far downstream from the inlet at any time is zero. Note that only for the case of instantaneous particle injection, n_o has units of particles per cross-sectional area of the fracture while $\delta(\xi)$ has units of inverse length. The analytical solution to (4.8) subject to (4.9), (4.10), and (4.11) has been derived by *Carslaw and Jaeger* [1988, p. 258] and it is presented here as a function of the original variable $x = \xi + U_{\text{eff}}t$ as follows:

$$\bar{n}(x, t) = \frac{n_o}{(4\pi D_{\text{eff}}t)^{1/2}} \exp\left[-\frac{(x - U_{\text{eff}}t)^2}{4D_{\text{eff}}t}\right]. \quad (4.12)$$

The subscript d_p has been dropped for solutions involving monodisperse particles to differentiate those solutions from the solutions for polydisperse particle plumes. It should be noted that (4.12) is a novel analytical solution because of the new definitions of U_{eff} and D_{eff} for particles of diameter d_p given by (3.3) and (3.25), respectively.

4.3.1.2 Polydisperse Particle Plume

Because the governing partial differential equation (4.8) is linear in \bar{n}_{d_p} , superposition of two or more solutions for differently sized particles is allowed, provided that the boundary and initial conditions as well as the domains of the various solutions are identical. For an initial number concentration of polydisperse particles introduced into the fracture, $n_{o_{d_p}}$, consisting of several discrete initial number sub-concentrations of particles with diameter d_p ,

$$n_{o_{d_p}} = \sum_{d_p} n_o(d_p). \quad (4.13)$$

In view of the analytical solution for a monodisperse particle distribution given by (4.12), with n_o replaced by $n_o(d_p)$, the analytical solution for the polydisperse particle distribution is obtained by

summing the individual solutions corresponding to each discrete $n_o(d_p)$ as follows:

$$\bar{n}_{d_p}(x, t) = \sum_{d_p} \frac{n_o(d_p)}{(4\pi D_{\text{eff}} t)^{1/2}} \exp\left[-\frac{(x - U_{\text{eff}} t)^2}{4D_{\text{eff}} t}\right]. \quad (4.14)$$

For a continuous distribution of particle diameters the initial number concentration of polydisperse particles is expressed as

$$n_{o_{d_p}} = \int_0^\infty n_{\text{pdf}} \, dd_p, \quad (4.15)$$

where n_{pdf} is an appropriate probability density function of polydisperse particles introduced into the fracture. Consequently, the analytical solution for a continuous distribution of instantaneously injected polydisperse particles is obtained from (4.15) by replacing the summation with integration over the entire range of particle sizes in the polydisperse particle distribution and replacing $n_o(d_p)$ with n_{pdf} as follows:

$$\bar{n}_{d_p}(x, t) = \int_0^\infty \frac{n_{\text{pdf}}}{(4\pi D_{\text{eff}} t)^{1/2}} \exp\left[-\frac{(x - U_{\text{eff}} t)^2}{4D_{\text{eff}} t}\right] \, dd_p. \quad (4.16)$$

Employing (3.3) and (3.25) in (4.16) yields an integral equation expressing the temporally and spatially varying particle concentration of a polydisperse particle plume within a water saturated fracture with uniform aperture that is a function of the distribution of particle diameters. Note that, in practice, the upper limit of integration in (4.16) need only be evaluated to b because $d_p < b$.

4.3.2 Constant Concentration Injection Without Particle Sorption

4.3.2.1 Monodisperse Particle Plume

Berkowitz and Zhou [1996] have presented a solution for the specific case of solute transport in a channel formed between two parallel plates with a constant concentration inlet boundary condition. In this section the model is extended to the more general case of transport of finitely sized, monodisperse colloids subject to constant concentration injection. Using the Taylor–Aris assumptions of axial advection and transverse molecular diffusion being the dominant transport processes, (4.8) may be solved analytically for an average particle concentration across the fracture, subject to

constant concentration particle injection. For the case when a fracture is initially free of particles, with a constant concentration of particles at the inlet, and without colloid reactions at the fracture walls, the appropriate boundary and initial conditions are:

$$\bar{n}_{d_p}(0, t) = n_o, \quad (4.17)$$

$$\bar{n}_{d_p}(\infty, t) = 0, \quad (4.18)$$

$$\bar{n}_{d_p}(\xi, 0) = 0, \quad (4.19)$$

where n_o is the total number of monodisperse colloids per unit fracture volume (concentration). The analytical solution to (4.8) subject to (4.17), (4.18), and (4.19) may be found using Laplace transform techniques [*van Genuchten and Alves, 1982; Berkowitz and Zhou, 1996*]. It is presented here in a form that accounts for the finite size of the particles as

$$\bar{n}(x, t) = \frac{n_o}{2} \left\{ \operatorname{erfc} \left[\frac{x - U_{\text{eff}} t}{2(D_{\text{eff}} t)^{1/2}} \right] + \exp \left(\frac{x U_{\text{eff}}}{D_{\text{eff}}} \right) \operatorname{erfc} \left[\frac{x + U_{\text{eff}} t}{2(D_{\text{eff}} t)^{1/2}} \right] \right\}, \quad (4.20)$$

where U_{eff} and D_{eff} are given by (3.3) and (3.25), respectively.

4.3.2.2 Polydisperse Particle Plume

The analytical solution for the more general case of a constant concentration injection of polydisperse particles in the absence of particle sorption onto the fracture walls is obtained in this section. Substituting (4.15) for n_o in (4.20) and integrating the resulting expression for the average colloid concentration over all particle diameters leads to the following expression for the time and space dependent polydisperse particle concentration

$$\bar{n}_{d_p}(x, t) = \frac{1}{2} \int_0^\infty n_{\text{pdf}} \left\{ \operatorname{erfc} \left[\frac{x - U_{\text{eff}} t}{2(D_{\text{eff}} t)^{1/2}} \right] + \exp \left(\frac{x U_{\text{eff}}}{D_{\text{eff}}} \right) \operatorname{erfc} \left[\frac{x + U_{\text{eff}} t}{2(D_{\text{eff}} t)^{1/2}} \right] \right\} dd_p. \quad (4.21)$$

The size dependent values for the effective velocity and effective dispersion coefficient given by (3.3) and (3.25), respectively, should be used in the preceding equation. It is noteworthy that in both (4.20) and (4.21) the term involving the exponential function is non-zero only for small x or t .

4.3.3 Constant Concentration Injection with Irreversible Sorption

4.3.3.1 Monodisperse Particle Plume

Colloid particles present in environmental systems have physicochemical properties that allow them to react with the media in which they reside. Consequently, particle–wall reactions (attachment) can be important processes affecting the movement of a particle plume within a water saturated fracture. The particle concentration sorbed onto the walls of a fracture may be determined through the solution of the governing partial differential equation (4.2).

The local linear irreversible rate of particle sorption as a function of the average colloid concentration across the fracture can be expressed as [Abdel-Salam and Chrysikopoulos, 1994]

$$\frac{\partial n_{d_p}^*(x, t)}{\partial t} = k_f \bar{n}_{d_p}(x, t), \quad (4.22)$$

where k_f is the forward sorption rate constant that is often expressed as a function of particle diameter [Adamczyk et al., 1992a]. In view of (4.22), the governing equation (4.2) can be rewritten as

$$\frac{\mathcal{D}_{d_p} \partial n_{d_p}(x, \pm b/2, t)}{\partial z} = -k_f \bar{n}_{d_p}(x, t). \quad (4.23)$$

The preceding equation expresses the flux of particles at the fracture walls as a function of average colloid concentration across the fracture, particle diffusion coefficient, and sorption rate.

Following the procedures of Appendix D, each term of the governing transport equation (4.1) is averaged across the fracture according to (4.7), yielding the following differential equation for average solute concentration:

$$\frac{\partial \bar{n}_{d_p}(x, t)}{\partial t} = \mathcal{D}_{d_p} \left[\frac{\partial^2 \bar{n}_{d_p}(x, t)}{\partial x^2} + \frac{\partial n_{d_p}(x, \pm b/2, t)}{\partial z} \right] - \frac{\partial}{\partial x} \int_{-\frac{b}{2}}^{\frac{b}{2}} u_x(z) n_{d_p}(x, z, t) dz. \quad (4.24)$$

Substitution of the Poiseuille velocity profile given by (3.1) for $u_x(z)$ and evaluating the integral term as well as employing (4.23) in (4.24) yields the following one–dimensional advection–diffusion equation with a first–order decay term

$$\frac{\partial \bar{n}_{d_p}(x, t)}{\partial t} = D_{\text{eff}} \frac{\partial^2 \bar{n}_{d_p}(x, t)}{\partial x^2} - U_{\text{eff}} \frac{\partial \bar{n}_{d_p}(x, t)}{\partial x} + K_{\text{eff}} \bar{n}_{d_p}(x, t), \quad (4.25)$$

where the effective decay, advection, and dispersion constants for irreversibly sorbing colloids are given by (4.3), (4.5), and (4.6), respectively.

The solution to (4.25) subject to the following constant concentration inlet boundary and initial conditions

$$\bar{n}_{d_p}(0, t) = n_o, \quad (4.26)$$

$$\bar{n}_{d_p}(\infty, t) = 0, \quad (4.27)$$

$$\bar{n}_{d_p}(x, 0) = 0, \quad (4.28)$$

is tabulated by *van Genuchten and Alves* [1982]:

$$\begin{aligned} \bar{n}(x, t) = & \frac{n_o}{2} \exp\left(\frac{xU_{\text{eff}}}{2D_{\text{eff}}}\right) \left\{ \exp\left(-\frac{\Omega x}{2D_{\text{eff}}}\right) \operatorname{erfc}\left[\frac{x - \Omega t}{2(D_{\text{eff}}t)^{1/2}}\right] \right. \\ & \left. + \exp\left(\frac{\Omega x}{2D_{\text{eff}}}\right) \operatorname{erfc}\left[\frac{x + \Omega t}{2(D_{\text{eff}}t)^{1/2}}\right] \right\}, \end{aligned} \quad (4.29)$$

$$\Omega = (U_{\text{eff}}^2 + 4K_{\text{eff}}D_{\text{eff}})^{1/2}, \quad (4.30)$$

where, for the case of finitely sized particles undergoing irreversible sorption at the fracture walls considered here, K_{eff} , U_{eff} , and D_{eff} are given by (4.3), (4.5), and (4.6), respectively.

4.3.3.2 Polydisperse Particle Plume

The analytical solution for the particle number concentration of a continuous distribution of polydisperse particles is obtained by integrating (4.29) over all particle diameters and using $n_{o_{d_p}}$ from (4.15) in place of n_o to yield

$$\begin{aligned} \bar{n}_{d_p}(x, t) = & \frac{1}{2} \int_0^\infty n_{\text{pdf}} \exp\left(\frac{xU_{\text{eff}}}{2D_{\text{eff}}}\right) \left\{ \exp\left(-\frac{\Omega x}{2D_{\text{eff}}}\right) \operatorname{erfc}\left[\frac{x - \Omega t}{2(D_{\text{eff}}t)^{1/2}}\right] \right. \\ & \left. + \exp\left(\frac{\Omega x}{2D_{\text{eff}}}\right) \operatorname{erfc}\left[\frac{x + \Omega t}{2(D_{\text{eff}}t)^{1/2}}\right] \right\} dd_p, \end{aligned} \quad (4.31)$$

where K_{eff} , U_{eff} , D_{eff} , and Ω are defined in (4.3), (4.5), (4.6), and (4.30) respectively. The last term inside the integral of the preceding equation rapidly diminishes for increasing x or t , as it does in (4.29).

4.3.4 Constant Concentration Injection with Reversible Sorption

4.3.4.1 Monodisperse Particle Plume

Changes in solution chemistry of the interstitial fluid and the presence of hydraulic gradients within the fracture may contribute to the resuspension of previously deposited colloid particles. Consequently, we consider the case where particles are allowed to reversibly sorb onto fracture walls. It is assumed that local chemical equilibrium exists throughout the system. For simplicity, the following linear isotherm is used to express the relationship between the average number of particles in solution and the number of particles sorbed onto the solid surface

$$n_{d_p}^*(x, t) = k_r \bar{n}_{d_p}(x, t), \quad (4.32)$$

where k_r is the surface distribution coefficient. Taking the derivative of both sides of (4.32) with respect to time yields the desired expression for the time dependent flux of colloids at the fracture surface

$$\frac{\partial n_{d_p}^*(x, t)}{\partial t} = k_r \frac{\partial \bar{n}_{d_p}(x, t)}{\partial t}. \quad (4.33)$$

A closed form analytical solution to the coupled governing equations (4.1) and (4.2) subject to a constant concentration of colloids at the inlet and reversible wall attachment is not achievable. However, for the special case where the particle concentration is averaged across the fracture, the following one-dimensional advection–dispersion equation approximates the transport of finitely sized particles along a uniform aperture fracture [*Domenico and Schwartz*, 1990, p. 477]:

$$\frac{\partial \bar{n}_{d_p}(x, t)}{\partial t} + \frac{2}{b} \frac{\partial n_{d_p}^*(x, t)}{\partial t} = D_{\text{eff}} \frac{\partial^2 \bar{n}_{d_p}(x, t)}{\partial x^2} - U_{\text{eff}} \frac{\partial \bar{n}_{d_p}(x, t)}{\partial x}. \quad (4.34)$$

The preceding equation is a consequence of mass conservation applied to the average colloid concentration within the fracture. The factor of two in front of the rate of change of sorbed colloids per unit fracture surface area arises from colloids reversibly sorbing onto both walls of the fracture. Employing (4.33) in (4.34) yields

$$R \frac{\partial \bar{n}_{d_p}(x, t)}{\partial t} = D_{\text{eff}} \frac{\partial^2 \bar{n}_{d_p}(x, t)}{\partial x^2} - U_{\text{eff}} \frac{\partial \bar{n}_{d_p}(x, t)}{\partial x}, \quad (4.35)$$

where U_{eff} and D_{eff} are given by (3.3) and (3.25), respectively; and the retardation factor, R , of the suspended particles is a function of the forward sorption rate constant as well as the fracture aperture and is given by

$$R = 1 + 2\frac{k_r}{b}. \quad (4.36)$$

The solution to the governing partial differential equation (4.35) subject to boundary and initial conditions (4.26), (4.27), and (4.28) was tabulated by *van Genuchten and Alves* [1982] and it is presented here in a modified form that accounts for finitely sized particles

$$\bar{n}(x, t) = \frac{n_o}{2} \left\{ \operatorname{erfc} \left[\frac{Rx - U_{\text{eff}}t}{2(D_{\text{eff}}Rt)^{1/2}} \right] + \exp \left(\frac{xU_{\text{eff}}}{D_{\text{eff}}} \right) \operatorname{erfc} \left[\frac{Rx + U_{\text{eff}}t}{2(D_{\text{eff}}Rt)^{1/2}} \right] \right\}, \quad (4.37)$$

where U_{eff} and D_{eff} are given by (3.3) and (3.25), respectively. Note that when there is no wall reaction ($k_r = 0$) the retardation factor is one and (4.37) reduces to (4.20).

4.3.4.2 Polydisperse Particle Plume

Integrating (4.37) over all particle sizes, replacing n_o by $n_{o_{dp}}$ defined by equation (4.15), and using the size dependent effective velocity and effective dispersion coefficient given by (3.3) and (3.25), respectively, results in the following expression representing the time and space dependent number concentration of polydisperse colloids in a uniform fracture subject to linear reversible sorption at the fracture walls

$$\bar{n}_{dp}(x, t) = \frac{1}{2} \int_0^\infty n_{\text{pdf}} \left\{ \operatorname{erfc} \left[\frac{Rx - U_{\text{eff}}t}{2(D_{\text{eff}}Rt)^{1/2}} \right] + \exp \left(\frac{xU_{\text{eff}}}{D_{\text{eff}}} \right) \operatorname{erfc} \left[\frac{Rx + U_{\text{eff}}t}{2(D_{\text{eff}}Rt)^{1/2}} \right] \right\} dd_p. \quad (4.38)$$

A summary of all equations solved, boundary and initial conditions employed for each case, and their respective solutions is presented for monodisperse colloids in Table 4.1 and for polydisperse colloids in Table 4.2. Note that any appropriate probability density function n_{pdf} can be employed with the analytical solutions for polydisperse particle transport in saturated fractures derived here.

Table 4.1: Analytical solutions for monodisperse particle transport in saturated fractures.

Model	B.C.'s/I.C.	Analytical Solution
$\frac{\partial \bar{n}(\xi, t)}{\partial t} = D_{\text{eff}} \frac{\partial^2 \bar{n}(\xi, t)}{\partial \xi^2}$	$\bar{n}(0, t) = 0$	$\bar{n}(x, t) = \frac{n_o}{(4\pi D_{\text{eff}} t)^{1/2}} \exp\left[-\frac{(x - U_{\text{eff}} t)^2}{4D_{\text{eff}} t}\right]$
$\xi = x - U_{\text{eff}} t$	$\bar{n}(\infty, t) = 0$	$U_{\text{eff}} = \frac{2}{3} U_{\text{max}} \left[1 + \frac{d_p}{b} - \frac{1}{2} \left(\frac{d_p}{b}\right)^2\right]$
	$\bar{n}(\xi, 0) = n_o \delta(\xi)$	$D_{\text{eff}} = \mathcal{D}_{d_p} + \frac{2}{945} \frac{U_{\text{max}}^2 b^2}{\mathcal{D}_{d_p}} \left(1 - \frac{d_p}{b}\right)^6$
$\frac{\partial \bar{n}(\xi, t)}{\partial t} = D_{\text{eff}} \frac{\partial^2 \bar{n}(\xi, t)}{\partial \xi^2}$	$\bar{n}(0, t) = n_o$	$\bar{n}(x, t) = \frac{n_o}{2} \left\{ \text{erfc}\left[\frac{x - U_{\text{eff}} t}{2(D_{\text{eff}} t)^{1/2}}\right] \right.$
$\xi = x - U_{\text{eff}} t$	$\bar{n}(\infty, t) = 0$	$\left. + \exp\left(\frac{x U_{\text{eff}}}{D_{\text{eff}}}\right) \text{erfc}\left[\frac{x + U_{\text{eff}} t}{2(D_{\text{eff}} t)^{1/2}}\right] \right\}$
	$\bar{n}(\xi, 0) = 0$	$U_{\text{eff}} = \frac{2}{3} U_{\text{max}} \left[1 + \frac{d_p}{b} - \frac{1}{2} \left(\frac{d_p}{b}\right)^2\right]$
		$D_{\text{eff}} = \mathcal{D}_{d_p} + \frac{2}{945} \frac{U_{\text{max}}^2 b^2}{\mathcal{D}_{d_p}} \left(1 - \frac{d_p}{b}\right)^6$
$\frac{\partial \bar{n}(x, t)}{\partial t} = D_{\text{eff}} \frac{\partial^2 \bar{n}(x, t)}{\partial x^2}$	$\bar{n}(0, t) = n_o$	$\bar{n}(x, t) = \frac{n_o}{2} \exp\left(\frac{x U_{\text{eff}}}{2D_{\text{eff}}}\right) \left\{ \exp\left(-\frac{\Omega x}{2D_{\text{eff}}}\right) \times \right.$
$- U_{\text{eff}} \frac{\partial \bar{n}(x, t)}{\partial x}$	$\bar{n}(\infty, t) = 0$	$\left. \text{erfc}\left[\frac{x - \Omega t}{2(D_{\text{eff}} t)^{1/2}}\right] + \exp\left(\frac{\Omega x}{2D_{\text{eff}}}\right) \text{erfc}\left[\frac{x + \Omega t}{2(D_{\text{eff}} t)^{1/2}}\right] \right\}$
$+ K_{\text{eff}} \bar{n}(x, t)$	$\bar{n}(x, 0) = 0$	$\Omega = (U_{\text{eff}}^2 + 4K_{\text{eff}} D_{\text{eff}})^{1/2}$
		$U_{\text{eff}} = \frac{2}{3} U_{\text{max}} \left[1 + \frac{d_p}{b} - \frac{1}{2} \left(\frac{d_p}{b}\right)^2 + \frac{2}{5} \frac{Da}{6+Da}\right]$
		$D_{\text{eff}} = \mathcal{D}_{d_p} + \frac{2}{945} \frac{U_{\text{max}}^2 b^2}{\mathcal{D}_{d_p}} \left[\left(1 - \frac{d_p}{b}\right)^6 - \frac{7}{10} \frac{Da}{6+Da}\right]$
		$K_{\text{eff}} = \frac{12\mathcal{D}_{d_p}}{b^2} \frac{Da}{6+Da}$
$R \frac{\partial \bar{n}(x, t)}{\partial t} = D_{\text{eff}} \frac{\partial^2 \bar{n}(x, t)}{\partial x^2}$	$\bar{n}(0, t) = n_o$	$\bar{n}(x, t) = \frac{n_o}{2} \left\{ \text{erfc}\left[\frac{Rx - U_{\text{eff}} t}{2(D_{\text{eff}} Rt)^{1/2}}\right] \right.$
$- U_{\text{eff}} \frac{\partial \bar{n}(x, t)}{\partial x}$	$\bar{n}(\infty, t) = 0$	$\left. + \exp\left(\frac{x U_{\text{eff}}}{D_{\text{eff}}}\right) \text{erfc}\left[\frac{Rx + U_{\text{eff}} t}{2(D_{\text{eff}} Rt)^{1/2}}\right] \right\}$
	$\bar{n}(x, 0) = 0$	$R = 1 + 2\frac{k_r}{b}$
		$U_{\text{eff}} = \frac{2}{3} U_{\text{max}} \left[1 + \frac{d_p}{b} - \frac{1}{2} \left(\frac{d_p}{b}\right)^2\right]$
		$D_{\text{eff}} = \mathcal{D}_{d_p} + \frac{2}{945} \frac{U_{\text{max}}^2 b^2}{\mathcal{D}_{d_p}} \left(1 - \frac{d_p}{b}\right)^6$

Table 4.2: Analytical solutions for polydisperse particle transport in saturated fractures.

Model	B.C.'s/I.C.	Analytical Solution
$\frac{\partial \bar{n}_{d_p}(\xi, t)}{\partial t} = D_{\text{eff}} \frac{\partial^2 \bar{n}_{d_p}(\xi, t)}{\partial \xi^2}$	$\bar{n}_{d_p}(0, t) = 0$	$\bar{n}_{d_p}(x, t) = \int_0^\infty \frac{n_{\text{pdf}}}{(4\pi D_{\text{eff}} t)^{1/2}} \exp\left[-\frac{(x-U_{\text{eff}}t)^2}{4D_{\text{eff}}t}\right] dd_p$
$\xi = x - U_{\text{eff}}t$	$\bar{n}_{d_p}(\infty, t) = 0$	$U_{\text{eff}} = \frac{2}{3}U_{\text{max}} \left[1 + \frac{d_p}{b} - \frac{1}{2} \left(\frac{d_p}{b}\right)^2\right]$
	$\bar{n}_{d_p}(\xi, 0) = n_{o_{d_p}} \delta(\xi)$	$D_{\text{eff}} = \mathcal{D}_{d_p} + \frac{2}{945} \frac{U_{\text{max}}^2 b^2}{\mathcal{D}_{d_p}} \left(1 - \frac{d_p}{b}\right)^6$
$\frac{\partial \bar{n}_{d_p}(\xi, t)}{\partial t} = D_{\text{eff}} \frac{\partial^2 \bar{n}_{d_p}(\xi, t)}{\partial \xi^2}$	$\bar{n}_{d_p}(0, t) = n_{o_{d_p}}$	$\bar{n}_{d_p}(x, t) = \frac{1}{2} \int_0^\infty n_{\text{pdf}} \left\{ \text{erfc}\left[\frac{x-U_{\text{eff}}t}{2(D_{\text{eff}}t)^{1/2}}\right] \right.$
$\xi = x - U_{\text{eff}}t$	$\bar{n}_{d_p}(\infty, t) = 0$	$\left. + \exp\left(\frac{xU_{\text{eff}}}{D_{\text{eff}}}\right) \text{erfc}\left[\frac{x+U_{\text{eff}}t}{2(D_{\text{eff}}t)^{1/2}}\right] \right\} dd_p$
	$\bar{n}_{d_p}(\xi, 0) = 0$	$U_{\text{eff}} = \frac{2}{3}U_{\text{max}} \left[1 + \frac{d_p}{b} - \frac{1}{2} \left(\frac{d_p}{b}\right)^2\right]$
		$D_{\text{eff}} = \mathcal{D}_{d_p} + \frac{2}{945} \frac{U_{\text{max}}^2 b^2}{\mathcal{D}_{d_p}} \left(1 - \frac{d_p}{b}\right)^6$
$\frac{\partial \bar{n}_{d_p}(x, t)}{\partial t} = D_{\text{eff}} \frac{\partial^2 \bar{n}_{d_p}(x, t)}{\partial x^2}$	$\bar{n}_{d_p}(0, t) = n_{o_{d_p}}$	$\bar{n}_{d_p}(x, t) = \frac{1}{2} \int_0^\infty n_{\text{pdf}} \exp\left(\frac{xU_{\text{eff}}}{2D_{\text{eff}}}\right) \times$
$- U_{\text{eff}} \frac{\partial \bar{n}_{d_p}(x, t)}{\partial x}$	$\bar{n}_{d_p}(\infty, t) = 0$	$\left\{ \exp\left(-\frac{\Omega x}{2D_{\text{eff}}}\right) \text{erfc}\left[\frac{x-\Omega t}{2(D_{\text{eff}}t)^{1/2}}\right] \right.$
$+ K_{\text{eff}} \bar{n}_{d_p}(x, t)$	$\bar{n}_{d_p}(x, 0) = 0$	$\left. + \exp\left(\frac{\Omega x}{2D_{\text{eff}}}\right) \text{erfc}\left[\frac{x+\Omega t}{2(D_{\text{eff}}t)^{1/2}}\right] \right\} dd_p$
		$\Omega = (U_{\text{eff}}^2 + 4K_{\text{eff}}D_{\text{eff}})^{1/2}$
		$U_{\text{eff}} = \frac{2}{3}U_{\text{max}} \left[1 + \frac{d_p}{b} - \frac{1}{2} \left(\frac{d_p}{b}\right)^2 + \frac{2}{5} \frac{Da}{6+Da}\right]$
		$D_{\text{eff}} = \mathcal{D}_{d_p} + \frac{2}{945} \frac{U_{\text{max}}^2 b^2}{\mathcal{D}_{d_p}} \left[\left(1 - \frac{d_p}{b}\right)^6 - \frac{7}{10} \frac{Da}{6+Da}\right]$
		$K_{\text{eff}} = \frac{12\mathcal{D}_{d_p}}{b^2} \frac{Da}{6+Da}$
$R \frac{\partial \bar{n}_{d_p}(x, t)}{\partial t} = D_{\text{eff}} \frac{\partial^2 \bar{n}_{d_p}(x, t)}{\partial x^2}$	$\bar{n}_{d_p}(0, t) = n_{o_{d_p}}$	$\bar{n}_{d_p}(x, t) = \frac{1}{2} \int_0^\infty n_{\text{pdf}} \left\{ \text{erfc}\left[\frac{Rx-U_{\text{eff}}t}{2(D_{\text{eff}}Rt)^{1/2}}\right] \right.$
$- U_{\text{eff}} \frac{\partial \bar{n}_{d_p}(x, t)}{\partial x}$	$\bar{n}_{d_p}(\infty, t) = 0$	$\left. + \exp\left(\frac{xU_{\text{eff}}}{D_{\text{eff}}}\right) \text{erfc}\left[\frac{Rx+U_{\text{eff}}t}{2(D_{\text{eff}}Rt)^{1/2}}\right] \right\} dd_p$
	$\bar{n}_{d_p}(x, 0) = 0$	$R = 1 + 2\frac{k_r}{b}$
		$U_{\text{eff}} = \frac{2}{3}U_{\text{max}} \left[1 + \frac{d_p}{b} - \frac{1}{2} \left(\frac{d_p}{b}\right)^2\right]$
		$D_{\text{eff}} = \mathcal{D}_{d_p} + \frac{2}{945} \frac{U_{\text{max}}^2 b^2}{\mathcal{D}_{d_p}} \left(1 - \frac{d_p}{b}\right)^6$

4.4 Discussion

Particles found in natural environments are never of a single size; rather, they have a distribution of diameters. *Ledin et al.* [1994] have suggested that naturally occurring particles follow a log-normal distribution of diameters given by:

$$n_{\text{pdf}} = \frac{n_o}{\sqrt{2\pi}\zeta d_p} \exp \left[-\frac{1}{2} \left(\frac{\ln d_p - \lambda}{\zeta} \right)^2 \right], \quad (4.39)$$

where λ is the mean of the particle log-diameters; and ζ^2 is the variance of the particle log-diameters. In this work the mean particle diameter is represented by $\mu_{d_p} = \exp(\lambda + 0.5\zeta^2)$ and the standard deviation of the particle diameter by $\sigma_{d_p} = \mu_{d_p} (e^{\zeta^2} - 1)^{1/2}$ [*Ang and Tang*, 1975]. The initial concentration of polydisperse colloids in a plume is determined by integrating the preceding equation over all particles diameters in the distribution.

For the model simulations presented in this work four different particle distributions consisting of $n_o = n_{o_{d_p}} = 10,000$ particles/m³ are considered. One distribution is composed of monodisperse particles with diameter $d_p = 1 \times 10^{-6}$ m. The other three polydisperse particle distributions are composed of particles with log-normally distributed diameters; however, all have mean particle diameter $\mu_{d_p} = 1 \times 10^{-6}$ m with increasing standard deviations of $\sigma_{d_p} = 0.3, 0.6,$ and $0.9 \mu\text{m}$. It is assumed that the fracture has an aperture of $b = 1 \times 10^{-4}$ m and the maximum centerline velocity of the interstitial fluid is $U_{\text{max}} = 1 \times 10^{-6}$ m/s. The results from the model simulations are presented as space and time dependent particle concentrations in the form of snapshots in time, or breakthrough curves. The snapshots are taken after 5,000 hours of transport time in the system, while the breakthrough curves are estimated at a distance of 12 m from the particle injection point.

Figure 4.1a illustrates snapshots of particle number concentrations evaluated by (4.12) for the monodisperse particle distribution and by (4.16) for the polydisperse particle distributions at a time of 5,000 hours after the instantaneous injection of the particles into the fracture. Note that simply changing the value of σ_{d_p} changes the shape of the concentration profile. A large σ_{d_p} implies a wide range of particle diameters with a greater number of small particles and a few

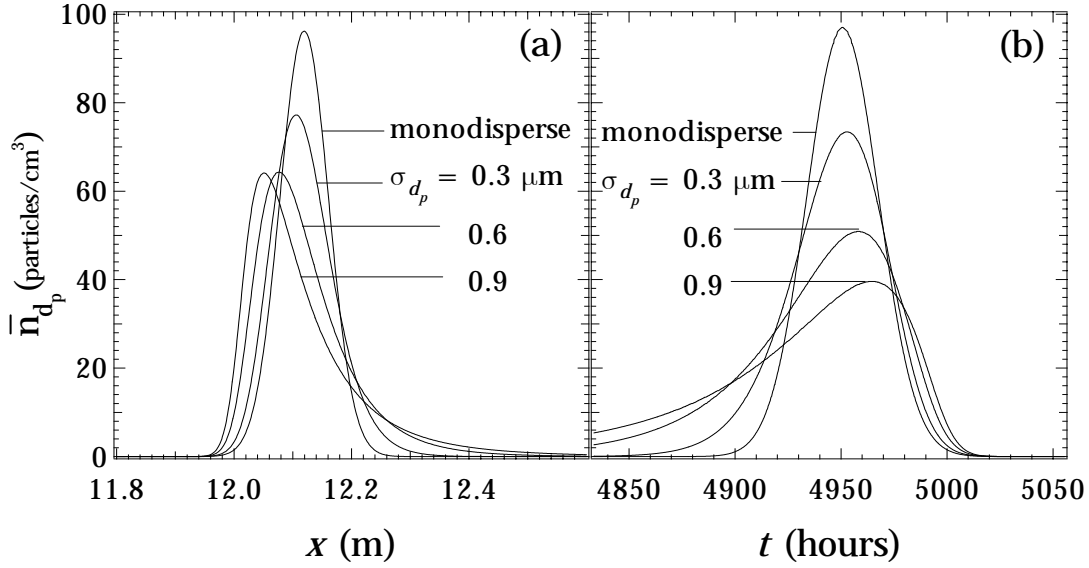


Figure 4.1: Particle concentration (a) snapshots and (b) breakthrough curves generated from (4.12) and (4.16) for 10,000 particles instantaneously injected at $t = 0$ into an aperture with $U_{\max} = 1 \times 10^{-6}$ m/s and $b = 1 \times 10^{-4}$ m. Three of the plumes are polydisperse and consist of particles with log-normally distributed diameters of $\mu_{d_p} = 1 \mu\text{m}$ and $\sigma_{d_p} = 0.3, 0.6,$ and $0.9 \mu\text{m}$, respectively, while the fourth plume is monodisperse and consists of particles with diameter $1 \mu\text{m}$. The snapshots of particle concentrations were evaluated 5,000 hours after injection and breakthrough curves were determined 12 m downstream from the particle injection location.

very large particles. These few largest particles experience the greatest mean velocity and lead the concentration front. Conversely, the many small particles contribute to a slower moving peak concentration that lags the peak concentration of the monodisperse distribution. Figure 4.1b shows normalized breakthrough curves evaluated by (4.12) and (4.16) at a distance of 12 m from the instantaneous injection point. Because of the increased range of colloid sizes for plumes with larger standard deviation in particle diameter, the particle distribution with $\sigma_{d_p} = 0.9 \mu\text{m}$ contains the largest and smallest colloids considered. The earlier initial breakthrough of this plume is attributed to the increased effective velocity of the largest particles. Further, complete breakthrough of this plume is delayed because of the many slower moving small particles.

Figure 4.2a shows normalized particle concentration fronts evaluated by (4.20) for the monodisperse particle distribution and by (4.21) for the polydisperse particle distributions at a

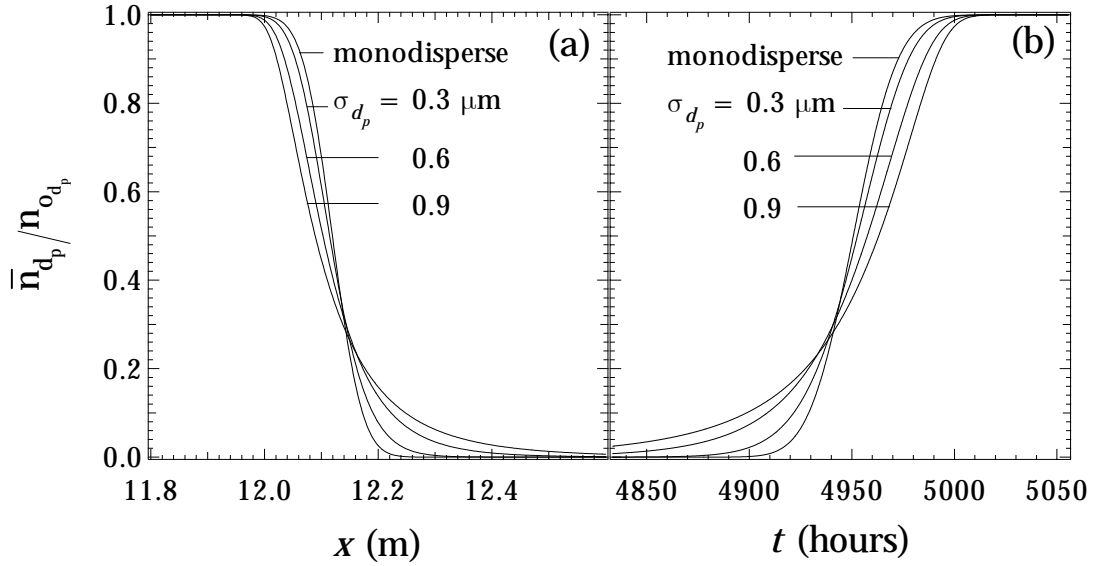


Figure 4.2: Normalized particle concentration (a) snapshots and (b) breakthrough curves evaluated by (4.20) and (4.21) for a constant concentration inlet boundary condition (here $U_{\max} = 1 \times 10^{-6}$ m/s, $b = 1 \times 10^{-4}$ m, $t = 5,000$ hr, and $x = 12$ m).

time of 5,000 hours after the initiation of constant concentration injection. Note that the steepest concentration front is exhibited by the monodisperse particle distribution. Increasing the standard deviation of the particle diameters increases the dispersion of the plume because polydisperse plumes with large standard deviations have greater ranges of effective particle velocities and effective dispersion coefficients. The normalized particle concentration breakthrough curves at a distance of 12 m from the fracture inlet are evaluated by (4.20) or (4.21) for constant concentration injection of the particle distributions and are illustrated in Figure 4.2b. Again, note the increasing dispersion of particle distributions with increasing standard deviation.

Normalized particle concentration fronts evaluated by (4.29) for the monodisperse particle distribution and by (4.31) for the polydisperse particle distributions subject to constant concentration injection and irreversible particle sorption onto the fracture walls are shown in Figure 4.3a. Note that the simulations are conducted for a constant Damköhler number of $Da = 1 \times 10^{-3}$. This small value was selected to show the advancing front of the particle plumes because a larger Damköhler number leads to deposition of the entire particle plume. Selecting a constant Damköhler

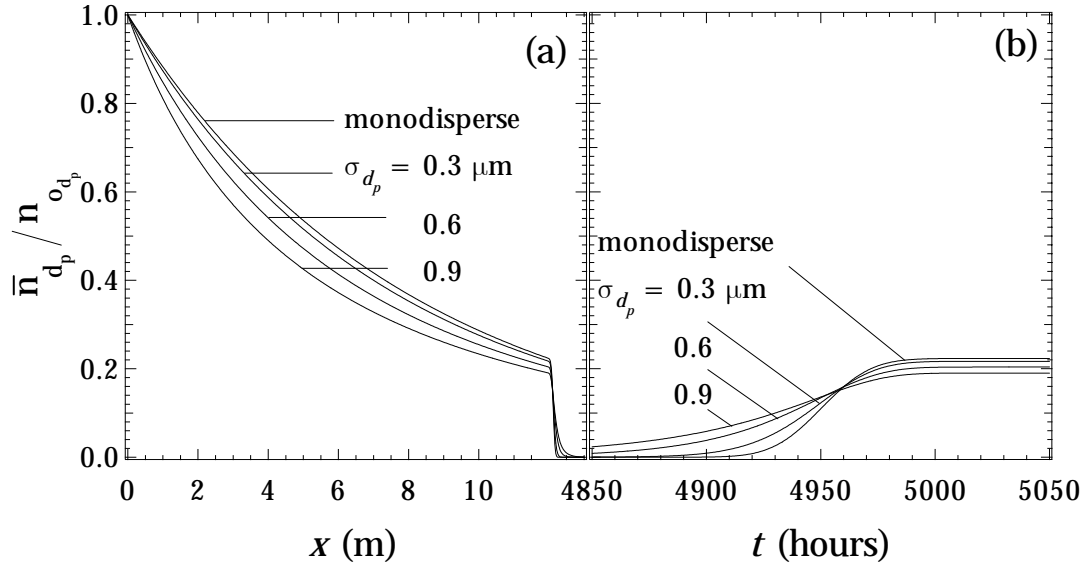


Figure 4.3: Normalized particle concentration (a) snapshots and (b) breakthrough curves evaluated by (4.29) and (4.31) for a constant concentration inlet boundary condition accounting for irreversible particle–wall reaction (here $U_{\max} = 1 \times 10^{-6}$ m/s, $b = 1 \times 10^{-4}$ m, $Da = 1 \times 10^{-3}$, $t = 5,000$ hr, and $x = 12$ m).

number forces the forward sorption rate coefficient, k_f , to be a function of particle size. Because the Damköhler number (4.4) describes the relative effect of reaction to that of molecular diffusion on particle transport and because a smaller particle has a larger molecular diffusion rate, a small particle will have a proportionally large forward sorption rate coefficient (inversely proportional to the particle diameter). Note the decreasing particle concentration with increasing σ_{d_p} (more small particles) of the injected particle distribution. Figure 4.3b illustrates the particle breakthrough curves evaluated from (4.29) and (4.31). It is evident that increasing the standard deviation of particle diameter leads to increased particle attachment onto the fracture walls. The particle distribution with the highest standard deviation in particle size contains the greatest number of small colloids (with large k_f). Small particles with large forward sorption rate coefficients preferentially sorb onto the fracture walls leading to a decreased normalized concentration breakthrough for the particle distribution with the largest standard deviation in particle diameter at a distance of 12 m from injection.

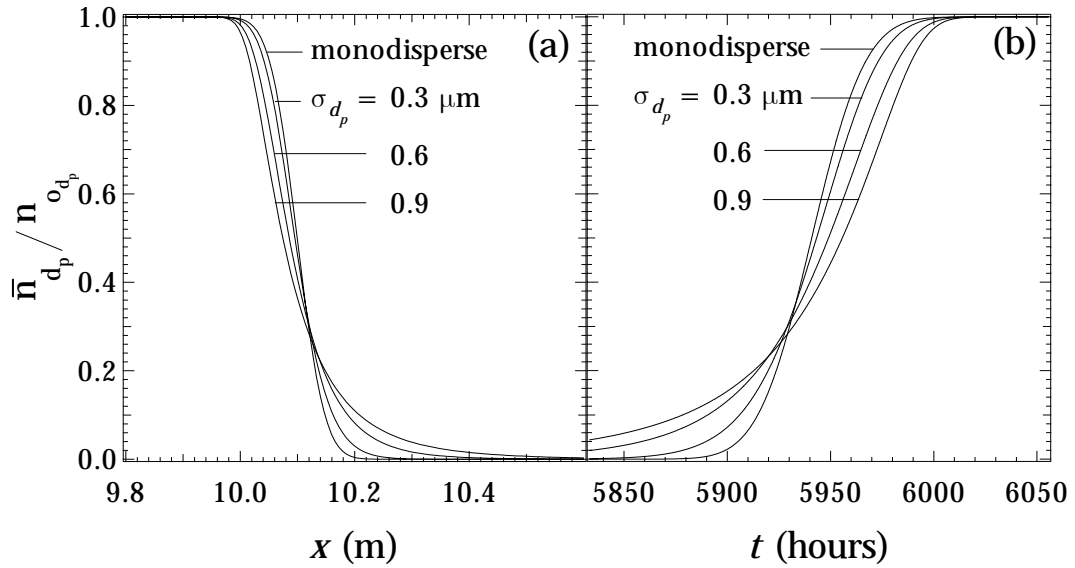


Figure 4.4: Normalized particle concentration (a) snapshots and (b) breakthrough curves evaluated by (4.37) and (4.38) for a constant concentration inlet boundary condition accounting for reversible particle–wall reaction (here $U_{\max} = 1 \times 10^{-6}$ m/s, $b = 1 \times 10^{-4}$ m, $k_r = 1 \times 10^{-5}$, $t = 5,000$ hr, and $x = 12$ m).

The normalized particle concentration fronts evaluated by (4.37) for the monodisperse particle distribution and by (4.38) for the polydisperse particle distributions subject to constant concentration injection and reversible sorption after 5,000 hours of simulation time are shown in Figure 4.4a. A retardation factor of $R = 1.2$ with $k_r = 1 \times 10^{-5}$ m was employed. The reversible sorption process serves primarily to retard the propagation of the particle concentration fronts. Figure 4.4b illustrates four normalized particle concentration breakthrough curves evaluated by (4.37) and (4.38). It should be noted that for the conditions considered here the time required for the particle plumes to achieve complete breakthrough at a distance of 12 m from the particle injection point is much greater than for the case of non-sorbing particles shown in Figure 4.3b.

4.5 Comparison with Experimental Data

An effort has been made to compare the analytical results derived in this work to available experimental data. Unfortunately, no experimental data could be found for the case of polydisperse particle transport. However, *Bales et al.* [1989] have experimentally studied virus transport in fractured rock. In their experiment a constant concentration of suspended *f2* coliphages (diameter 2.3×10^{-8} m) was introduced at the inlet of a 19 cm long natural fracture at a volumetric flow rate of 1.83×10^{-10} m³/s. The effective cross-sectional area of the fracture was calculated by dividing the estimated volume of the fracture by the estimated effective aperture and found to be 8.65×10^{-6} m². Although the effective porosity was reported as 0.23, the coliphages are considered large enough that penetration of the rock matrix is negligible. This experimental procedure can be most accurately compared to the solution for a constant concentration injection of monodisperse particles without reaction at the fracture walls given by (4.20) with U_{eff} and D_{eff} evaluated by (3.3) and (3.25), respectively. Because the experimental fracture was of natural rock with non-uniform aperture, the analytical results based on a uniform fracture may not be directly applicable to this case. Consequently, a nonlinear least squares procedure [*Pezzullo, 2000*] was employed in order to fit the experimental data using the calculated effective cross-sectional area of the fracture as the dependent variable. This procedure yielded an estimate of 1.00×10^{-5} m² for the effective cross-sectional fracture area, similar to the value suggested by *Bales et al.* [1989]. Dividing the volumetric flow rate by the fitted value of the effective cross-sectional area yields a mean fluid velocity within the fracture of $\bar{U} = 2/3U_{\text{max}} = 1.83 \times 10^{-5}$ m/s. Figure 4.5 clearly shows a good agreement between the model prediction (solid curve) and the experimental data (bullets).

4.6 Summary

Analytical solutions describing the transport of one monodisperse and three polydisperse particle plumes through a single fracture with uniform aperture accounting for an axial parabolic

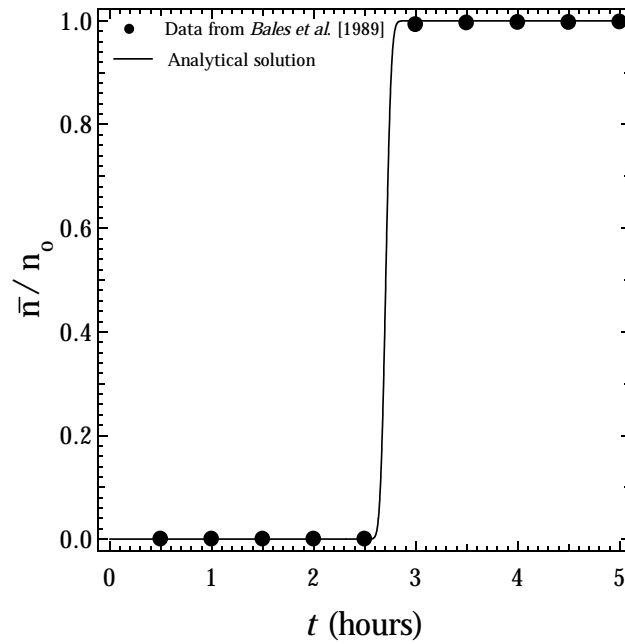


Figure 4.5: Comparison of experimental data from *Bales et al.* [1989] and the analytical solution (4.20) for *f2* coliphage (monodisperse particle) transport in a natural fracture in the absence of particle–wall reaction (here $b = 1.33 \times 10^{-4}$ m, $d_p = 2.3 \times 10^{-8}$ m, $\bar{U} = 2/3U_{\max} = 1.83 \times 10^{-5}$ m/s, and $x = 0.19$ m).

velocity profile, transverse molecular diffusion, and particle–wall reaction are derived. It is shown that a distribution in constituent diameters of a polydisperse particle plume significantly affects the shape of snapshots and concentration breakthrough curves. Increasing the range of colloid sizes while maintaining the mean colloid size increases the overall spreading of a particle plume. Based on data gathered from reported field studies, a log–normal distribution of particle sizes was used for the polydisperse plumes. A comparison of the analytical solution for instantaneous colloid injection into a fracture with no reaction at the walls and experimental data for coliphages traveling down a 19 cm natural fracture is made. Using a nonlinear least squares estimate for the fracture cross–sectional area, excellent agreement between the experimental data and the analytical breakthrough curve was observed.

Chapter 5

A New Particle Tracking Equation

5.1 Introduction

With the ever expanding capabilities of computers, particle tracking solutions to various engineering problems are becoming increasingly accurate. Although random walk methods, Monte Carlo simulations, and Fokker–Planck solutions to differential equations have been employed for many years, the availability of inexpensive high speed processors and vast memory storage has allowed the application of these solution techniques to increasingly complex problems [e.g. *Uffink*, 1989; *Valocchi and Quinodoz*, 1989; *Yamashita and Kimura*, 1990; *Lu*, 2000; *Liu et al.*, 2000; *Michalak and Kitanidis*, 2000]. For example, *James and Chrysikopoulos* [1999, 2000] have investigated particle tracking schemes that model the transport of variably sized colloids in both uniform and variable aperture fractures. *James and Chrysikopoulos* [2001a, b] have also compared a traditional particle tracking algorithm with analytical solutions for the ideal case of polydisperse colloid transport in a uniform fracture and excellent agreement was shown. However, for more realistic and involved models accounting for a fracture with variable aperture, a distribution of particle sizes, or particle sorption onto the fracture walls, a traditional particle tracking algorithm may not be the most efficient solution method [*James and Chrysikopoulos*, 2000]. There are often cases when

a particle tracking algorithm using a constant time step may lead to both insufficient prediction accuracy and excessive computation time.

An important case where the traditional particle tracking equation with a constant time step may be insufficient arises in the study of polydisperse colloid transport. Consider the simple example of random diffusion of a plume of polydisperse colloids in a quiescent fluid. Particle tracking theory suggests that the time step should be chosen small enough to represent the time that a particle might take to travel along a certain path before it is forced to significantly deviate from its course through a molecular exchange of kinetic energy [Uffink, 1988]. If a constant time step that is appropriate for the median colloid size is applied to all particles in the plume, this constant time step, when applied to colloid particles at each extreme of the size distribution, yields undesirable results. Colloid diameters and corresponding molecular diffusion coefficients can span several orders of magnitude, and as a result, the smallest colloids may travel diffusively too far during this pre-determined time step to meet the desired accuracy, while the largest colloids may require an excessive number of time steps to achieve the desired solution interval resulting in increased computational cost.

Another case when the traditional particle tracking algorithm may be insufficient is when the transport of colloids is significantly affected by deposition onto formation surfaces. As a colloid travels through a fracture, transport mechanisms may eventually bring the particle close enough to a fracture wall to have the opportunity to establish a contact at the liquid–solid matrix interface. If a time step was specified, rarely would the particle exactly encounter a sorption site on the fracture wall. Instead, by determining a random diffusive travel time for the particle to reach the fracture wall a known distance away, knowledge of exactly where and when a particle encounters a sorption site is obtained. In either of the above mentioned cases, a particle tracking equation with a pre-determined spatial step yielding a random travel time would achieve the desired predictional accuracy while maximizing computational efficiency.

The new particle tracking equation will maximize computational efficiency and solution accuracy by specifying a priori a spatial step and determining the random time it will take a spherical particle of neutral buoyancy to diffusively travel a specified distance. This chapter formally presents the methodology used to obtain accurate coefficients for the new particle tracking equation. Results based on the new particle tracking algorithm are validated through comparison with both an analytical solution and results from the traditional particle tracking equation.

5.2 Model Development

5.2.1 Traditional Particle Tracking Equation

The traditional particle tracking transport equation for the solution of advection–diffusion problems consists of a deterministic (or absolute advective) term, and a stochastic (or diffusive) term that is a function of the random motion of the particle [Thompson, 1993; Kitaniadis, 1994]. For the case of particle diffusion in the absence of advection considered in this chapter, the advective term is eliminated and in vector notation the traditional diffusive particle tracking equation is given by

$$\mathbf{X}^m = \mathbf{X}^{m-1} + \mathbf{B}(\mathbf{X}^{m-1}) \cdot \mathbf{Z}(0,1) \sqrt{\Delta t}, \quad (5.1)$$

where exponent m is the numerical step number; $\mathbf{X}^m = (x^m, y^m, z^m)^T$ is a three-dimensional position vector representing the x^m , y^m , and z^m Cartesian coordinates of the centroid location of a particle at the numerical step m ; $\mathbf{B}(\mathbf{X}^{m-1})$ is a deterministic scaling second order tensor, evaluated at \mathbf{X}^{m-1} , that is a function of the spreading of the particle plume; and $\mathbf{Z}(0,1)$ is a vector of three independent random numbers selected from the standard normal distribution (zero mean and unit variance). When only molecular diffusion is considered, the terms of the diagonal second-order tensor $\mathbf{B}(\mathbf{X}^{m-1})$ are equal to $\sqrt{2\mathcal{D}_{d_p}}$ [Ahlstrom et al., 1977]. The diffusive particle tracking vector equation (5.1) may be replaced by the following directional particle tracking equations,

$$x^m = x^{m-1} + Z(0,1) \sqrt{2\mathcal{D}_{d_p} \Delta t} \quad (5.2)$$

$$y^m = y^{m-1} + Z(0, 1) \sqrt{2\mathcal{D}_{d_p} \Delta t} \quad (5.3)$$

$$z^m = z^{m-1} + Z(0, 1) \sqrt{2\mathcal{D}_{d_p} \Delta t} \quad (5.4)$$

Traditionally, a time step is specified and an updated position vector is marched through time until the desired solution can be examined. In the limit of $\Delta t \rightarrow 0$, the particle tracking equation (5.1) becomes an exact solution to the diffusion equation [Kinzelbach, 1988; Thompson and Gelhar, 1990]. However, the cost of improved accuracy is increased processor time that is inversely proportional to decreasing Δt . When choosing an appropriate time step, both the accuracy of the solution and computational cost should be considered.

A particle suspended in a quiescent volume of fluid undergoes molecular diffusion in all three dimensions. Figure 5.1 shows the (a) x, y -plane and (b) x, z -plane Brownian motion pathlines for a particle with diameter $d_p = 1 \times 10^{-6}$ m that was released at the origin and allowed to diffuse in water at $T = 288.15$ K according to (5.2)–(5.4) with a time step of $\Delta t = 0.1$ s. The time required for this particle to exit a spherical volume of water with radius 5×10^{-5} m was $\Sigma \Delta t = 3,860$ s.

It is expected that the times required for a particle to repeatedly travel a constant distance would follow some distribution of random times. An intuitive estimation of the time required for a particle to travel a specified distance $\Delta z = z^m - z^{m-1}$ might be obtained by rearranging the traditional particle tracking equation (5.2) to solve for Δt as follows

$$\Delta t = \frac{[\Delta z / Z(0, 1)]^2}{2\mathcal{D}_{d_p}}. \quad (5.5)$$

However, if a plume of particles with diameter $d_p = 1 \times 10^{-6}$ m (i.e., colloidal particles) are to travel a distance of $\Delta z = 5 \times 10^{-5}$ m in water at $T = 288.15$ K, the preceding equation yields travel times ranging from 1 second to on the order of 10^{11} seconds, depending on the value of the random number $Z(0, 1)$. Neither end of the spectrum of travel times are physically observed, recall that the particle in Figure 5.1 required 3,860 s to travel 5×10^{-5} m. Shortest travel times are obtained for normally distributed random numbers with values greater than 1. In view of (5.5) it is evident that the large travel times are consequences of dividing Δz by a random number with value approaching

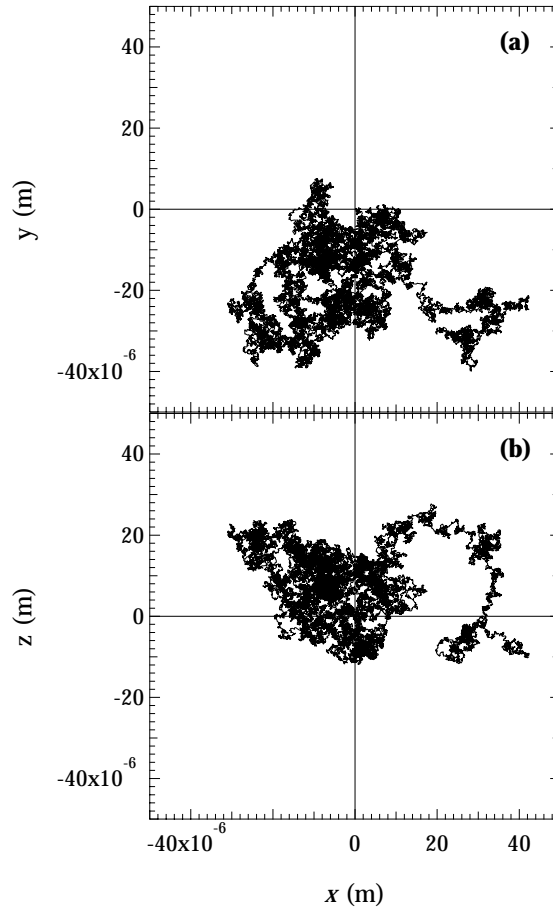


Figure 5.1: Pathline projected at (a) the x, y -plane; and (b) the x, z -plane of the Brownian motion for a particle of size $d_p = 1 \times 10^{-6}$ m released at the origin of a spherical volume of water of radius 5×10^{-5} m.

the zero mean. Any random number that falls near the mean (i.e., in the range of $\pm 10^{-5}$) produces a travel time too large to be physically reasonable. Clearly, the expression (5.5) is not adequate for the estimation of particle travel times.

5.2.2 New Particle Tracking Equation

The goal of this chapter is to generate a new particle tracking equation that expresses a diffusive travel time as a random function of a particle's diffusion coefficient and the distance traveled. Because diffusion is an isotropic process, the diffusive particle tracking equation (5.1) may

be studied by any of the three directional particle tracking equations (5.2)—(5.4). In this analysis, (5.4) will be used, but similar results may also be obtained from (5.2) or (5.3). The traditional particle tracking equation with an extremely small time step is used to generate histograms of times necessary for plumes of uniquely sized monodisperse particles to travel a preselected distance $|\Delta z|$ with the intent of determining the relationship between the characteristics of the histograms and the parameters, Δz and \mathcal{D}_{d_p} .

The one-dimensional particle tracking equation (5.2) is employed to simulate the diffusion of a particle plume in the x -direction initially released in water at $T = 288.15$ K and at $z = 0$ (the origin). Each particle is allowed to randomly diffuse until it moves a distance of $\Delta z = \pm 5 \times 10^{-5}$ m from the origin. The selected travel distance is representative of a typical fracture aperture in a fractured rock formation. The numerical time step is chosen to be $\Delta t = 1$ second, so that a large number of time steps ($\sim 3,000$ for a particle with diameter $d_p = 1 \times 10^{-6}$ m) will be required for any particle to travel the specified distance, even for the extreme case when the magnitude of all randomly generated numbers is 1. If the time step is too large, accuracy is compromised. The travel time, $\Sigma \Delta t$, required for the particle to achieve the specified distance $|\Delta z| = 5 \times 10^{-5}$ is recorded. This particle diffusion process is repeated 500,000 times. Each stochastic trajectory mimics the actual path of an individual particle. Collectively, the trajectories illustrate the overall behavior of a 500,000 particle plume. It should be noted that any possible particle-particle interactions are not accounted for in the present analysis. One hundred unique particle travel time histograms are prepared for particle diameters ranging from 1×10^{-7} m to 1×10^{-5} m in increments of 1×10^{-7} m. Figure 5.2 presents three of the one hundred travel time histograms generated by this process. Figure 5.2a is the histogram generated for the smallest particles considered in this study ($d_p = 1 \times 10^{-7}$ m); Figure 5.2b represents the median particle size examined ($d_p = 1 \times 10^{-6}$ m); and Figure 5.2c the largest particles ($d_p = 1 \times 10^{-5}$ m). Figure 5.2 supports the suggestion by *Tory* [2000] that diffusive travel times are log-normally distributed. Note that the travel times increase proportionally to the increase in particle diameter (decreasing molecular diffusion coefficient).

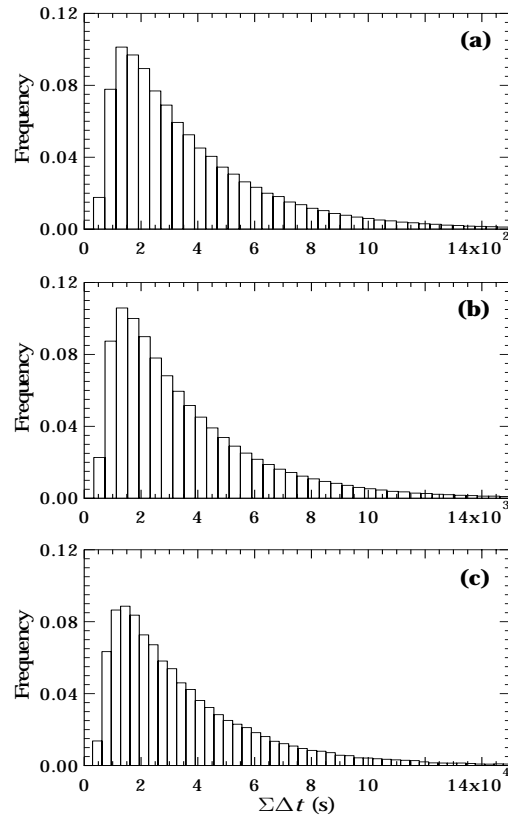


Figure 5.2: Histograms of travel times for monodisperse plumes of 500,000 particles of size (a) $d_p = 1 \times 10^{-7}$ m; (b) $d_p = 1 \times 10^{-6}$ m; and (c) $d_p = 1 \times 10^{-5}$ m, traveling a distance of $\Delta z = \pm 1 \times 10^{-5}$ m.

Taking the log of the travel time for each particle of the plume, $\tau = \ln \Sigma \Delta t$, and generating the corresponding histogram, it is observed that the normal probability density function (pdf) can consistently fit the distribution of log-travel times obtained by the traditional particle tracking equation (5.2). The normal pdf in terms of log-travel times is given by the equation [Banks *et al.*, 1996, p. 209],

$$f(\tau) = \frac{1}{\sigma_\tau \sqrt{2\pi}} \exp \left[-\frac{1}{2} \left(\frac{\tau - \mu_\tau}{\sigma_\tau} \right)^2 \right], \quad (5.6)$$

where μ_τ and σ_τ are the mean and standard deviation of log-travel times, respectively.

Figure 5.3 presents the three probability distributions of log-travel times corresponding to the same plumes of 500,000 monodisperse particles used to construct Figure 5.2. The solid lines on

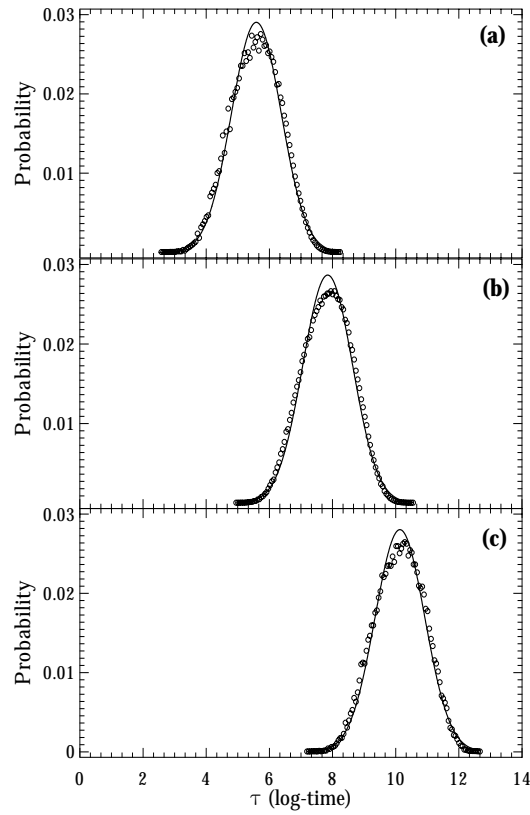


Figure 5.3: Probability distributions of log-travel times for the same monodisperse plumes used to generate Figure 5.2. The solid lines are obtained from the normal probability distribution function with parameters (a) $\mu_\tau = 5.588$ and $\sigma_\tau = 0.786$; (b) $\mu_\tau = 7.848$ and $\sigma_\tau = 0.787$; and (c) $\mu_\tau = 10.133$ and $\sigma_\tau = 0.787$.

Figure 5.3 represent the normal pdf's generated by (5.6). The parameters in (5.6), μ_τ and σ_τ , are the calculated arithmetic mean and standard deviation, respectively, of the log-travel times for the 500,000 particles of each plume. Note that in Figure 5.3a, $\mu_\tau = 5.588$ and $\sigma_\tau = 0.786$; in Figure 5.3b, $\mu_\tau = 7.848$ and $\sigma_\tau = 0.787$; and in Figure 5.3c, $\mu_\tau = 10.133$ and $\sigma_\tau = 0.787$.

Any normally distributed random number, $Z(\mu_\tau, \sigma_\tau^2)$, can be generated from the standard normal distribution, $Z(0, 1)$, by employing the following relationship [Banks *et al.*, 1996, p. 342],

$$Z(\mu_\tau, \sigma_\tau^2) = \mu_\tau + \sigma_\tau Z(0, 1). \quad (5.7)$$

Because it is evident from Figure 5.3 that a normal pdf closely approximates the log-travel times for

a plume of particles, a random number generated by (5.7) can be used to determine the log-travel time necessary for a particle with known diffusion coefficient to travel a specified distance. Assuming that the mean, μ_τ , and standard deviation, σ_τ , of log-travel times may be expressed as functions of the variables, Δz and \mathcal{D}_{d_p} , then taking the inverse log of a single normally distributed number generated from $Z(\mu_\tau, \sigma_\tau^2)$ is equivalent to selecting a particle travel time from the histogram of such travel times (see Figure 5.2).

As seen in Figure 5.3, the mean log-travel time varies with the particle diameter (i.e., molecular diffusion coefficient) used in each numerical simulation. For the units of the mean log-travel time to be log-seconds, the relationship for the mean of the log-travel times must be linear with respect to $\ln[(\Delta z)^2 / \mathcal{D}_{d_p}]$ and of the form

$$\mu_\tau = \alpha \ln \left[\frac{(\Delta z)^2}{\mathcal{D}_{d_p}} \right] + \beta, \quad (5.8)$$

where α is the slope and β the y -intercept of the linear least squares fit. The preceding equation may be rearranged as follows

$$\mu_\tau = \ln \left\{ \left[\frac{(\Delta z)^2}{\mathcal{D}_{d_p}} \right]^\alpha \right\} + \beta. \quad (5.9)$$

For the units of the mean log-travel time, μ_τ , to be consistent in the preceding equation, α must be unity. Using a linear least squares procedure, the preceding equation is fit to the 100 numerically determined data points for μ_τ , thereby specifying the y -intercept $\beta = -0.978 \pm 0.012$. Consequently, the mean of the log-travel times can be expressed as,

$$\mu_\tau = \ln \left[\frac{(\Delta z)^2}{\mathcal{D}_{d_p}} \right] - 0.978. \quad (5.10)$$

Figure 5.4 shows the 100 numerically determined values for μ_τ together with the best linear fit. The correlation coefficient between the numerical data points and (5.10) is $R^2 \approx 1$, indicating a near perfect fit.

Simulation results show that the values of the standard deviation of the log-travel times for each particle plume are independent of Δx and \mathcal{D}_{d_p} . The arithmetic mean and variance of

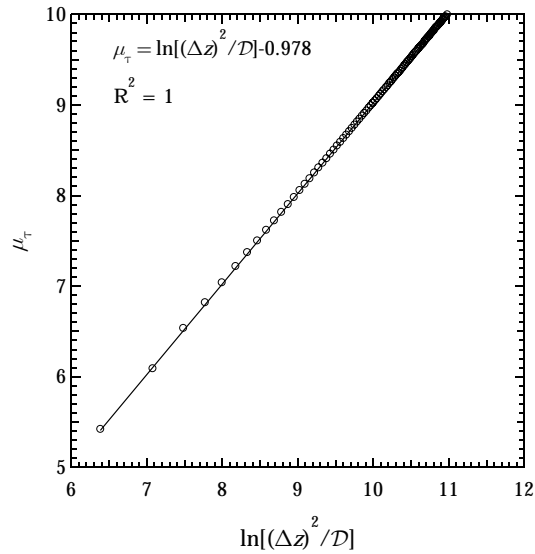


Figure 5.4: Variation of the mean log-travel time, μ_τ , as a function of the log of the ratio $(\Delta z)^2/D_{dp}$. The equation for the least squares fit (solid line) of the numerically determined values (open circles) and the corresponding correlation coefficient are shown.

the standard deviations of the log-travel times are 0.787 and 0.001, respectively, yielding a 95% confidence limit for the standard deviation in log-travel times of

$$\sigma_\tau = 0.787 \pm 0.002. \quad (5.11)$$

The standard deviation of log-travel times may be viewed as a measure of the difference between the fastest and slowest log-travel times for each particle plume, or the range of log-travel times. While these differences are constant on the log scale, the differences between the fastest and slowest actual travel times are inversely proportional to the molecular diffusion coefficient and proportional to the particle diameter (see Figure 5.2). For example, the range of travel times for 99% of the particles to travel the specified distance may be derived from properties of the normal distribution as $\exp(\mu_\tau + 2.58\sigma_\tau) - \exp(\mu_\tau - 2.58\sigma_\tau)$. Comparing the range of travel times for the values used in Figure 5.3a and 5.3b shows that the ratio of these ranges is 0.101, essentially the ratio of the diameters of the particles used for these simulations. Larger particles take a longer time to diffusively travel the specified distance while having a correspondingly larger range of travel times.

Substituting (5.10) and (5.11) into (5.7) yields,

$$Z(\mu_\tau, \sigma_\tau^2) = \ln \left[\frac{(\Delta z)^2}{\mathcal{D}_{d_p}} \right] - 0.978 + 0.787Z(0, 1). \quad (5.12)$$

Taking the inverse log of the previous equation yields a log-normally distributed travel time. Consequently, the time step necessary for a particle to travel a specified distance, Δz , may be written as:

$$\begin{aligned} \Delta t &= \exp [Z(\mu_\tau, \sigma_\tau^2)] \\ &= \exp \left\{ \ln \left[\frac{(\Delta z)^2}{\mathcal{D}_{d_p}} \right] - 0.978 + 0.787Z(0, 1) \right\}. \end{aligned} \quad (5.13)$$

A new particle tracking equation is obtained by recasting the preceding equation to describe the current time of a particle as a function of its previous time, specified travel distance, and particle diffusion coefficient as follows:

$$t^m = t^{m-1} + \exp \left\{ \ln \left[\frac{(z^m - z^{m-1})^2}{\mathcal{D}_{d_p}} \right] - 0.978 + 0.787Z(0, 1) \right\}. \quad (5.14)$$

To find the time for a particle to move a specified distance, $\Delta z = z^m - z^{m-1}$, select a single value from the standard normal distribution and substitute it into (5.14). It should be noted that *Reimus* [1995] has presented, without proof, the following particle tracking equation

$$\begin{aligned} \Delta t &= \exp \left\{ \ln \left[\frac{(\Delta z)^2}{2\mathcal{D}} \right] - 0.2 + 0.79Z(0, 1) \right\} \\ &= \exp \left\{ \ln \left[\frac{(\Delta z)^2}{\mathcal{D}_{d_p}} \right] - 0.89 + 0.79Z(0, 1) \right\}. \end{aligned} \quad (5.15)$$

Although equations (5.14) and (5.15) are similar, they have some subtle differences that will be discussed in the next section.

5.3 Verification

Consider a uniform fracture with aperture $b = 5 \times 10^{-5}$ m that is saturated with water (288.15 K) that is flowing with a Poiseuille velocity profile with maximum centerline velocity of

$U_{\max} = 1 \times 10^{-6}$ m/s. A polydisperse colloid (particle) plume of 10,000 particles with neutral buoyancy and log-normally distributed diameters with mean, $\mu_{d_p} = 1 \mu\text{m}$, and standard deviation, $\sigma_{d_p} = 0.9 \mu\text{m}$, is instantaneously injected at the fracture inlet at time zero. The various times required for the 10,000 particles to travel 8 m are used to generate the cumulative particle breakthrough curve. Three methods are used to obtain the cumulative particle breakthrough curves: the first method employs the traditional particle tracking algorithm with a constant time step, the second method utilizes the new particle tracking algorithm with a constant spatial step derived here, and the third method employs the analytical solution for polydisperse particle transport in a water saturated, uniform fracture (4.16) specified in Chapter 4 by equation (4.16) with effective plume velocity and effective plume dispersion coefficient given by (3.3) and (3.25), respectively.

5.3.1 Traditional Particle Tracking Algorithm

As discussed above, the general particle tracking transport equation consists of a non-stochastic or absolute term, the advection, and a stochastic term representing the random molecular diffusion [Thompson, 1993; Kitanidis, 1994]. In vector notation the particle tracking equations are [Thompson and Gelhar, 1990]

$$\mathbf{X}^m = \mathbf{X}^{m-1} + \mathbf{A}(\mathbf{X}^{m-1}) \Delta t + \mathbf{B}(\mathbf{X}^{m-1}) \cdot \mathbf{Z} \sqrt{\Delta t}, \quad (5.16)$$

where $\mathbf{A}(\mathbf{X}^{m-1})$ is the absolute forcing vector (i.e., the velocity profile) evaluated at \mathbf{X}^{m-1} ; and the remaining of the components are as described in the diffusive particle tracking equation (5.1). In view of (5.16), the traditional particle tracking transport equations for a uniform aperture fracture with a Poiseuille velocity profile can be written as:

$$x^m = x^{m-1} + U_{\max} \left[1 - 4 \left(\frac{z^{m-1}}{b} \right)^2 \right] \Delta t + Z(0, 1) \sqrt{2\mathcal{D}_{d_p} \Delta t}, \quad (5.17)$$

$$z^m = z^{m-1} + Z(0, 1) \sqrt{2\mathcal{D}_{d_p} \Delta t}. \quad (5.18)$$

The particle tracking model developed in this work assumes that every individual particle undergoes an incremental movement during each time step. It is understood that as a particle diffuses across

streamlines over a single time step that changes in particle velocity from the starting to ending location do not compromise the accuracy of the solution. The colloids are introduced at the inlet side of the fracture flow domain ($x = 0$) and distributed according to the local volumetric flow rate. It is assumed that the probability of a colloid entering the fracture at a given z -location (perpendicular to the fracture walls) is proportional to the flow rate at that particular position. Consequently, the probability of a colloid having a starting position of its centroid less than z is given by [Reimus, 1995]:

$$P(z) = \frac{\int_{-\frac{b}{2}}^z u_x(z) dz}{\int_{-\frac{b}{2}}^{\frac{b}{2}} u_x(z) dz}. \quad (5.19)$$

Substituting the Poiseuille velocity profile (3.1) into the preceding equation and integrating yields the following cubic equation

$$P(z) = -2 \left(\frac{z}{b} \right)^3 + \frac{3z}{2b} + \frac{1}{2}. \quad (5.20)$$

A uniform random number between zero and one is substituted for $P(z)$ in (5.20) and the roots of the resulting polynomial in z are evaluated by Newton's Method. Roots found outside of the range of $-b/2$ and $b/2$ are ignored. Because of the finite size of a particle it is possible that solution of (5.20) allows particle-wall overlap. If this occurs, new random numbers are selected until (5.20) yields a centroid location for a particle to be wholly contained within the fracture. Particle-particle interactions are not taken into account. A large number of particles is used in an effort to reduce random noise. A time step of $\Delta t = 0.9$ s was selected for use in the traditional particle tracking equation because it is the mean diffusive travel time necessary for the smallest particle of the polydisperse plume ($d_p = 1 \times 10^{-8}$ m) to move a distance equal to $1/4^{\text{th}}$ of the aperture according to the new particle tracking equation (5.14). A particle normalized cumulative number breakthrough curve is generated by tracking the number of particles that exit the fracture at 8 m.

5.3.2 New Particle Tracking Algorithm

Because molecular diffusion is the only transport mechanism in the z -direction, a constant spatial step in z may be used to determine the time step. Another particle breakthrough curve was

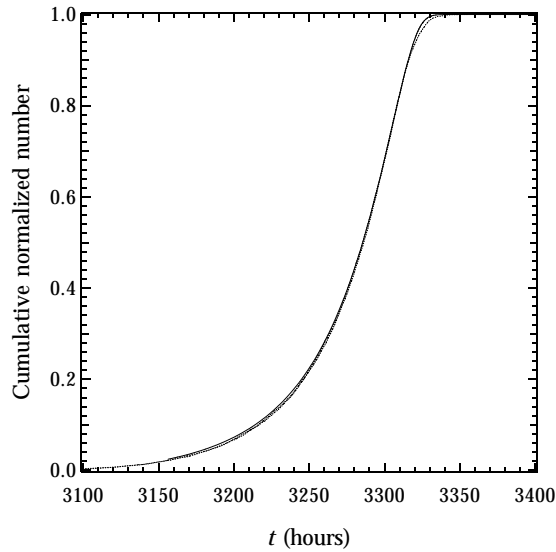


Figure 5.5: Cumulative normalized particle breakthrough curves determined by the traditional and new particle tracking algorithms (dashed lines) as well as by the analytical solution (solid line).

also generated using the new particle tracking equation with a constant spatial step equal to $1/4^{\text{th}}$ of the aperture ($\Delta z = 1.25 \times 10^{-5}$ m). Colloids are again placed in the fracture as a function of the flow rate according to (5.20). In the x -direction, the same particle tracking equation (5.17) is used to simulate particle motion; however, the spatial step in the z -direction is specified and the corresponding time step is calculated from (5.14). The particle tracking equation in the z -direction becomes

$$z^m = z^{m-1} \pm \Delta z, \quad (5.21)$$

where the direction of the displacement, $\pm \Delta z$, is determined from the sign of a standard normally distributed random number, $Z(0, 1)$.

5.3.3 Comparisons

Figure 5.5 shows that the cumulative particle breakthrough curves for each solution method are nearly coincident; however, the computational time required to produce each solution is quite different. Using a PC with an 866 MHz Pentium III processor, the traditional particle tracking equation required 32,071 seconds of CPU time to generate a solution while the new particle tracking

scheme required 3,100 seconds, an order of magnitude faster. It is apparent that for this case, the new particle tracking equation is computationally efficient and suffers no serious loss of accuracy.

Because the new particle tracking algorithm uses a constant spatial step to generate a random time step, at any spatial step level, m , each particle of the plume will have a different total travel time associated with it. This poses no problem when examining particle breakthrough curves; however, if reactive particles are considered one caveat is worthy of mention. If plume constituents are not all at the same time, local concentrations cannot be calculated. Sorption rate (or probability) may be a function of instantaneous local colloid concentrations and the constant spatial step particle tracking algorithm, without modification, is not a viable solution technique. In such instances, the traditional particle tracking algorithm may be a more appropriate solution technique.

5.4 Summary

Particle tracking methods are able to solve increasingly complex contaminant transport problems with the rapid advances in computing power. In cases where a constant time step is inappropriate (e.g., polydisperse particle plumes), it may be necessary to determine the (random) time it takes a particle to diffusively travel a specified distance. However, it is not possible to simply retrieve the time step directly from the traditional particle tracking equation. Because the size of a particle affects how it diffuses in a quiescent fluid, differently sized particles require different times to travel a given distance. Histograms of travel times for plumes of monodisperse particles were consistently log-normal in shape. Thus, probability distributions of the log-travel times are normally distributed. The parameters describing these normal distributions (i.e., mean and standard deviation of the log-travel times), are functions of the distance specified for travel and the diffusion coefficient of the particles. A constant standard deviation of log-travel times was found in each numerical simulation regardless of the parameter values, Δz and \mathcal{D}_{dp} . Using a least squares method, a linear relationship was found between the mean of the log-travel times and $\ln[(\Delta z)^2/\mathcal{D}_{dp}]$.

Employing the expressions obtained for the mean and standard deviation of the log-travel times, a new particle tracking equation with specified spatial step was determined. Using both the traditional and the new particle tracking algorithms to model polydisperse colloid transport in a fracture, a comparison of computational times proves that the new particle tracking equation derived here may be more efficient than the traditional particle tracking equation. Cumulative particle breakthrough curves for both constant spatial step and constant time step particle tracking algorithms compare favorably with the analytical solution. The new particle tracking equation is quite robust and may be applicable to particle tracking techniques where it is more appropriate to specify a spatial step than a temporal step.

Chapter 6

Transport in a Uniform Aperture

Fracture

6.1 Introduction

In this chapter, theoretical investigations based on particle tracking simulations are undertaken to gain a better understanding of the effect of a distribution of colloid sizes on their transport properties in a single fracture. Log-normal colloid diameter distributions are used because they are realistic representations of naturally occurring colloid suspensions [*Ledin et al.*, 1994]. Results are compared to analytical solutions derived in Chapter 4 for instantaneous particle injection within a uniform aperture fracture. The spreading of polydisperse colloid suspensions is compared to that of a monodisperse suspension. Matrix diffusion can serve to increase colloid residence time by back diffusion into the fracture once the bulk of the colloid cloud has moved downstream, and its role in colloid transport is examined as well. Furthermore, the effects of particle deposition onto fracture surfaces on the transport of colloids are investigated by both perfect sink and kinetic sorption models. For the kinetic sorption case both linear and nonlinear dynamic blocking functions (DBFs) are

employed, first applied to models of colloid transport in fractures by *Chrysikopoulos and Abdel-Salam* [1997]. Finally, the effect of fracture aperture on cumulative colloid breakthrough is investigated.

6.2 Model Development

6.2.1 Flow and Transport

As a basis for a comprehensive particle tracking simulation for polydisperse colloid transport in fractured media, particle movement in a single fracture with uniform aperture is considered in this chapter. Flow in the fracture is idealized as Poiseuille flow (i.e., having a parabolic velocity profile), where particles are both advected according to the local fluid velocity and diffused by molecular diffusion [*Buckley and Loyalka*, 1994]. The magnitude of the advective transport component is a function of the distance from the center of the fracture, i.e., the z -location as described by (3.1). Colloids are assumed to be hard spherical particles (i.e., no surface charge) that are advected and diffused through the aperture and are allowed to penetrate the surrounding matrix by diffusion or attach onto fracture walls. Although settling rates can affect colloid transport in fractures, gravitational effects have been disregarded in the interest of simplicity and in order to explicitly examine ideal particle transport in a single uniform fracture. *Ledin et al.* [1994] reported that colloids found in natural environments often follow a log-normal size distribution. The log-normal probability density function for colloid concentration was given by (4.39). A similar equation is used to describe the number of polydisperse colloids in a plume (as opposed to concentration) by replacing n_o with \mathcal{N}_o , the total number of plume constituents. The total number of particles in a log-normally distributed colloid plume is:

$$\begin{aligned} \mathcal{N}_{o_{dp}} &= \int_0^\infty \mathcal{N}_{pdf} \, dd_p \\ &= \int_0^\infty \frac{\mathcal{N}_o}{\sqrt{2\pi}\zeta d_p} \exp\left[-\frac{1}{2}\left(\frac{\ln d_p - \lambda}{\zeta}\right)^2\right] \, dd_p, \end{aligned} \quad (6.1)$$

where parameters λ and ζ are defined below (4.39).

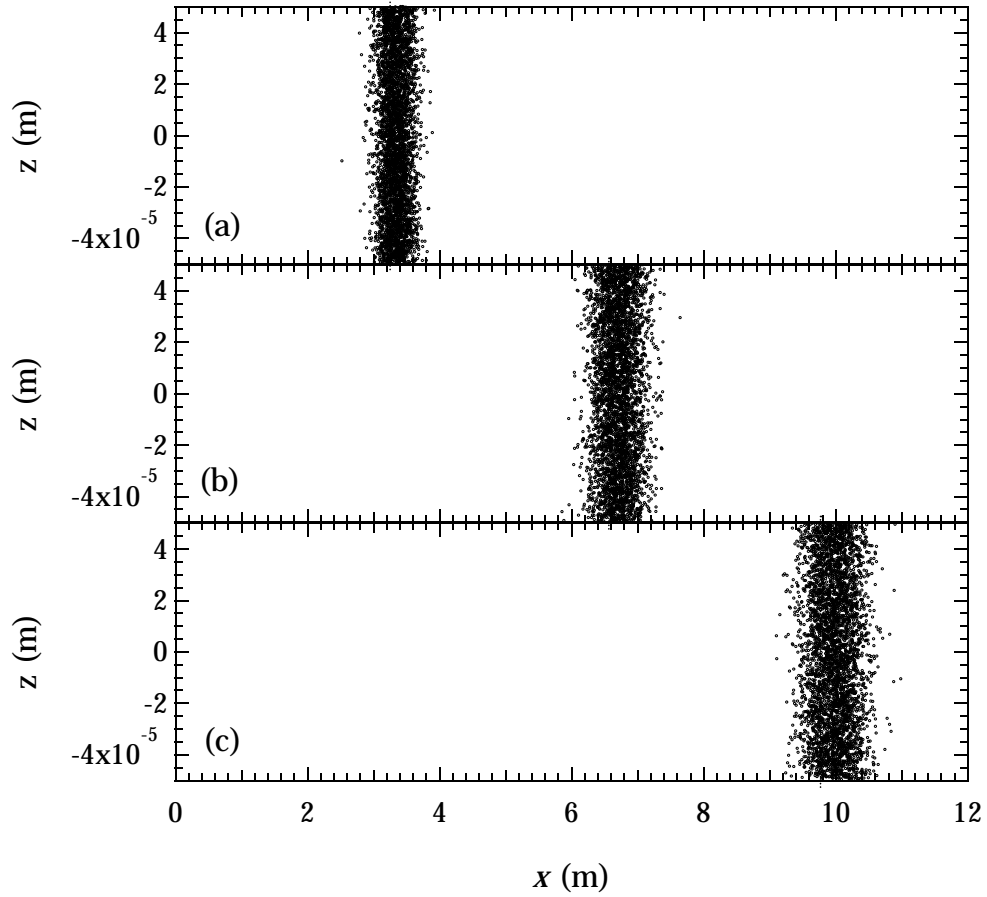


Figure 6.1: Monodisperse colloid transport in a uniform aperture fracture at simulation times of (a) 5×10^9 seconds, (b) 10×10^9 seconds, and (c) 15×10^9 seconds (here $d_p = 1 \times 10^{-6}$ m, $U_{\max} = 1 \times 10^{-9}$ m/s, and $b = 1 \times 10^{-4}$ m).

Recall that under fully developed Taylor conditions, axial advection and radial diffusion contribute to the overall dispersion with the net result of colloids traveling in an apparent plug flow. The difference between a parabolic velocity profile and a uniform velocity profile on particle transport lies in the spreading of the colloids. In plug flow, the diffusion coefficient, \mathcal{D}_{d_p} , may be orders of magnitude less than in parabolic flow where the effective dispersion coefficient, D_{eff} , governs the spreading. Figure 6.1 shows three snapshots of particle tracking data for a fracture with aperture $b = 1 \times 10^{-4}$ m and maximum fluid velocity $U_{\max} = 1 \times 10^{-9}$ m/s. The very small fluid velocity was chosen in order to make more prominent the dispersive effects on the instantaneous source of colloids

at this scale. It is evident from Figure 6.1 that the colloids are, on average, traveling slightly faster than the mean fluid velocity (dashed vertical line). Although there is a parabolic velocity profile within the fracture, the colloids are traveling as if under plug flow conditions because at fully developed Taylor conditions the dispersive pattern of colloids appears to be similar to that observed in plug flow as expected.

6.3 Matrix Diffusion

Diffusion within the matrix is typically modeled as a Fickian process where a concentration gradient controls mass transfer. As a colloid moves between fracture and matrix a sharp gradient is encountered both in porosity and diffusivity. *Thompson and Gelhar* [1990] note that additional deterministic velocity terms are necessary additions to a particle tracking algorithm when gradients in diffusivity or porosity exist. The appropriate mathematical expressions are:

$$U_{\mathcal{D}} = \nabla \cdot \mathcal{D}_{d_p} \quad (6.2)$$

$$U_{\theta} = \mathcal{D}_{d_p} (\nabla \cdot \ln \theta) \quad (6.3)$$

where $U_{\mathcal{D}}$ and U_{θ} are the deterministic velocities due to diffusivity and porosity gradients, respectively; and θ is the local porosity. If (6.2) and (6.3) are not included in a particle tracking algorithm, particles will falsely accumulate in stagnant and low porosity zones of the flow system.

6.4 Colloid Deposition

6.4.1 Perfect Sink Approximation

Colloid deposition onto fracture surfaces is often considered a relatively fast process when compared to interstitial fluid velocity so that a sorption relationship like the Smulochowski–Levich approximation is assumed valid. The Smulochowski–Levich relationship is an approximate analytical solution to the perfect sink model that solves the transport and continuity equations based on

Eulerian theory. With some manipulation, it can be cast in a form similar to a linear local irreversible deposition representation. As opposed to Lagrangian methods where the trajectories of individual particles are calculated (e.g., the particle tracking method), Eulerian methods describe particles collectively in terms of their distribution, or probability density, in space and time, $\bar{n}_{d_p}(x, t)$. Recall from Chapter 4 that the rate of change of the concentration of sorbed particles per unit fracture surface area is a function of the number of particles in the bulk solution:

$$\frac{\partial n_{d_p}^*(x, t)}{\partial t} = k_f \bar{n}_{d_p}(x, t), \quad (6.4)$$

where k_f is an approximation to the forward sorption rate coefficient. In the Smulochowski–Levich sorption relationship, deposition is described in terms of particle flux onto sorbent surfaces as a function of the colloid number concentration, $\bar{n}_{d_p}(x, t)$, flow velocity, U_{\max} , molecular diffusion coefficient, \mathcal{D}_{d_p} , fracture aperture, b , and distance from the fracture inlet, x . Due to the lack of detailed information on actual fracture conditions, and questionable validity of available colloidal force expressions applicable near walls, the attachment process of colloids is often represented by highly idealized models that, in an Eulerian analysis, are employed as boundary conditions for the governing transport equations. The Smulochowski–Levich approximation is a perfect sink model which assumes that the particle–wall hydrodynamic repulsive interaction is exactly counterbalanced by van der Waals attractions between the particle and the wall, and that all other colloidal and external forces are absent [*Elimelech et al.*, 1995, p. 100]. In view of this approximation, an analytically derived expression for the local dimensionless mass transfer coefficient, representing colloid deposition onto the surfaces of a fracture during colloid transport, is defined as [*Adamczyk et al.*, 1983]

$$Sh = \frac{J d_p}{2 \bar{n}_{d_p} \mathcal{D}_{d_p}}, \quad (6.5)$$

where Sh is the Sherwood number; and J is the normal component of the local colloid flux at the wall. *Van de Ven* [1989, p. 273] has presented Sherwood numbers for several flow geometries with surface sorption. Specifically, in the case of a parallel plate channel, the Sherwood number is given

as

$$Sh = 0.538 \left(\frac{bPe}{x} \right)^{\frac{1}{3}}, \quad (6.6)$$

where the fracture Peclet number, Pe , for a parallel plate fracture is defined as [Adamczyk and van de Ven, 1980]

$$Pe = \frac{U_{\max} d_p^3}{2b^2 \mathcal{D}_{d_p}}. \quad (6.7)$$

Equating (6.5) and (6.6) and subsequently employing (6.7), yields the following expression for the colloid flux at the surfaces of the fracture

$$J = 0.854 \left(\frac{\mathcal{D}_{d_p}^2 U_{\max}}{xb} \right)^{\frac{1}{3}} \bar{n}_{d_p}(x, t). \quad (6.8)$$

From the local concentration of colloids in the fracture, it is possible to determine the particle flux at any location x on the collector (fracture) surface in particles per square meter per second because \mathcal{D}_{d_p} , U_{\max} , and b are known constants. The forward sorption coefficient may be found by equating the flux of colloids onto the fracture surface, (6.8), to the rate of change of attached colloids at the fracture surface, (6.4). This yields a forward sorption rate constant of

$$k_f = 0.854 \left(\frac{\mathcal{D}_{d_p}^2 U_{\max}}{xb} \right)^{\frac{1}{3}}. \quad (6.9)$$

The preceding expression is employed in (6.4). It is important to note that with the use of the Smulochowski–Levich assumptions, the fracture walls act as perfect sinks and deposition of colloids onto a smooth parallel plate channel is considered irreversible. In this particle tracking model the effect of colloid size variations on attachment are realized in the forward sorption rate coefficient, (6.9), that is a function of the diffusion coefficient and consequently, a function of the colloid diameter.

6.4.2 Kinetic Relationship

A kinetic sorption approach accounting for the surface exclusion effects of previously deposited variably sized colloids is also examined. As a colloid travels through the fracture, the transport mechanisms (advection and diffusion) may eventually bring the particle close enough to

the fracture surface to have the opportunity to establish a contact resulting from local interaction forces between the colloid and the liquid–solid matrix interface. The probability of the particle being placed (sticking probability) per wall collision, is calculated by a modified Boltzmann law [*Adamczyk et al.*, 1991]

$$p = \exp\left(-\frac{\phi}{kT}\right) F\left(n_{d_p}^*\right). \quad (6.10)$$

where ϕ is the repulsive energy of interaction between the particle and the fracture surface ($\phi \simeq 10kT$ [*Adamczyk et al.*, 1997]); and $F(n_{d_p}^*)$ is DBF that takes into account the effect of previously deposited colloids per unit fracture surface area on subsequent colloid deposition by specifying the portion of the fracture surface that remains available for deposition [*Chrysikopoulos and Abdel-Salam*, 1997]. The previous equation may be used to model colloid deposition onto a fracture surface that may have previously deposited colloids. The DBF ranges between one (for a fracture free of colloids) and zero (for a fracture surface completely covered by deposited colloids). The detachment of colloids may be modeled by determining the random time of attachment according to the procedures outlined by *Valocchi and Quinodoz* [1989]; however, when interstitial fluid and sorbent surface chemical conditions favor the attachment of stable colloid particles onto sorbent surfaces, colloid deposition is essentially irreversible and restricted to monolayer coverage [*Johnson et al.*, 1996]. The linear DBF (the area that remains available for a colloid to deposit onto the fracture wall) is given by [*Song and Elimelech*, 1994; *Chrysikopoulos and Abdel-Salam*, 1997]

$$F\left(n_{d_p}^*\right) = \frac{\epsilon_{\max} - \epsilon}{\epsilon_{\max}} \quad (6.11)$$

where

$$\epsilon(x, t) = A_p n_{d_p}^*(x, t) \quad (6.12)$$

and

$$\epsilon_{\max} = \frac{1}{\nu}, \quad (6.13)$$

and $A_p = \pi d_p^2/4$ is the cross-sectional area of a colloid particle; and ν is a factor accounting for blocked area not directly covered by the colloid (excluded area) [*Rajagopalan and Chu*, 1981]. Due

to electrostatic repulsive forces a sorbed colloid should effectively block more area than simply the space it physically occupies. For comparison, the following nonlinear DBF is also investigated in this study [Adamczyk *et al.*, 1992b]:

$$F(n_{d_p}^*) = 1 - 2.184 \left(\frac{\epsilon}{\epsilon_{\max}} \right) + 0.986 \left(\frac{\epsilon}{\epsilon_{\max}} \right)^2 + 0.29 \left(\frac{\epsilon}{\epsilon_{\max}} \right)^3. \quad (6.14)$$

The linear DBF is valid for spherical uncharged particles depositing onto a flat surface. At higher surface coverage ($\epsilon \geq \epsilon_{\max}/10$), (6.14) is a better estimate of the area blocked by the colloids and is valid for coverage up to $0.8\epsilon_{\max}$ [Adamczyk *et al.*, 1992a; Chrysikopoulos and Abdel-Salam, 1997]. The Boltzmann law assumes that if a particle comes into contact with a fracture wall it is either adsorbed with probability, p , or reflected thereby affording a probabilistic sorption model to simulate the kinetic sorption of colloids [Hinrichsen *et al.*, 1990]. For example, if $\phi = 10kT$ and the fracture surface is free of colloids, $F(n_{d_p}^*) = 1$, then according to (6.10), $p = 4.54 \times 10^{-5}$ and roughly 2 particles out of every 10^4 wall collisions will sorb onto the fracture surface. Because particle detachment is often considered irreversible, desorption is not modeled in this analysis and the time of attachment is infinite.

6.5 Particle Tracking

Particle tracking algorithms provide stochastic solutions to linear partial differential equations like the advection–diffusion equation. Although the particle tracking technique does not provide a direct numerical solution to a differential equation, it does not suffer from numerical dispersion as do the finite element and finite difference methods [Thompson and Gelhar, 1990]. Particle tracking techniques have been applied in numerous investigations of contaminant transport in porous and fractured media [Ahlstrom *et al.*, 1977; Smith and Schwartz, 1980; Kinzelbach, 1988; Chrysikopoulos *et al.*, 1992; Thompson *et al.*, 1996; James and Chrysikopoulos, 1999, 2000]. It should be noted that particle tracking is the only method that facilitates the use of variably sized colloids. Each particle is individually considered (i.e., stored in a memory location), and as such, it can retain its own

unique characteristics including, for example, size and sorption status. Although such factors as gravity, clogging, flocculation, and filtration can affect colloid transport in fractures, they have been disregarded in the interest of simplicity and in order to explicitly examine ideal particle transport and sorption in a uniform aperture fracture. Because of the varied transport mechanisms examined in this chapter, both traditional and new particle tracking algorithms must be utilized. For cases when colloids irreversibly sorb according to the Smulochowski–Levich approximation or when they diffuse into the surrounding rock matrix it is necessary to use a traditional particle tracking algorithm with equations given by (5.17) and (5.18). This is because in the perfect sink approximation, (6.4), colloid deposition is dependent upon the instantaneous local colloid concentration requiring all colloids to be at the same time level. For the case of matrix diffusion, it is not possible to specify a constant spatial step in the z -direction because of the deterministic velocities that must be included to take into account the low porosity and diffusivity of the surrounding matrix described by (6.2) and (6.3), respectively. For simulations involving non-sorbing and kinetically sorbing colloids, the new particle tracking algorithm is more efficient to use. The distance a particle moves in the z -direction, $\Delta z = z^m - z^{m-1} = b/4$, is specified and the corresponding travel time is calculated from the new particle tracking equation, (5.14). Once the time step associated with a particle's movement of Δz is determined, the corresponding distances moved by the particle in the x -direction is calculated from (5.17). As in (5.21), the z -direction that the particle follows (positive or negative) is specified by the sign of a standard normally distributed random number.

6.6 Numerical Procedures

6.6.1 Transport

The colloid plume is introduced at the inlet side of the fracture flow domain ($x = 0$) and distributed according to the local volumetric flow rate. It is assumed that the probability of a colloid entering the fracture at a given z location (perpendicular to the fracture walls) is proportional to

the flow rate at that particular position as done in Chapter 5. The probability of a colloid having a starting position less than z is given by (5.20). A large number of particles, on the order of 150,000, is used in an effort to reduce random noise [Valocchi and Quinodoz, 1989]. Although increasing the number of particles increases the computation time, a large number of particles leads to smoother results by averaging out the effect of individual particles. As in any averaging process, the larger the sample size, the less the contribution of a single component and the more smooth and regular the results. For the traditional particle tracking algorithm, at each time level a new particle position is determined from (5.17) and (5.18). The constant time step is chosen to be the mean time necessary for the smallest particle to diffusively travel a distance equal to $1/4^{\text{th}}$ of the fracture aperture according to (5.14). When the new particle tracking algorithm is employed, the spatial step is set equal to $1/4^{\text{th}}$ of the fracture aperture and the corresponding time step is calculated from (5.14) and used in (5.17). For the case where the solid matrix is impermeable (zero porosity), all particles are reflected from the wall as in a mirror image without loss of energy. That is, the final x -location remains unchanged, whereas the final z -coordinate is set a distance away from the wall equal to the distance that the particle would have obtained if it had penetrated the rock matrix plus the particle diameter. For example, if a particle of $d_p = 5 \times 10^{-7}$ m initially obtains a z value of 5.03×10^{-5} m (5×10^{-5} m being the location of the fracture wall), its reflected z -location would be 4.92×10^{-5} m.

6.6.2 Matrix Diffusion

For permeable rock matrices, each time a particle reaches a fracture surface, it has a probability of penetrating the matrix that is proportional to the matrix porosity. For example, when a colloid contacts a solid matrix with porosity 0.1, it has a 10% chance of encountering a void space of that solid matrix. A uniformly distributed random number between 0 and 1 is generated each time a particle encounters a wall, and if this number is less than the porosity, the colloid enters the matrix. It is assumed that a particle entering a solid matrix continues to migrate within

the pore as it did in the fracture only for the remaining portion of the time step, because when a particle enters a pore, it still experiences an effective porosity of 1.0 and its diffusivity is not altered from that in the fracture. Although the probability of penetrating the matrix is independent of particle size, once in the matrix, particle diameter affects how a particle is transported according to its diffusion coefficient (also a factor in both (6.2) and (6.3)). As the rock matrix interferes with colloid diffusion, the diffusion coefficient is also proportional to the solid matrix porosity (i.e., the value of the particle diffusion coefficient within a solid matrix with porosity 0.1 is assumed to be $0.1\mathcal{D}_{d_p}$ [Buckley and Loyalka, 1993]). Although wall effects on diffusion and velocity are known, no modification to diffusivity or particle velocity in the fracture near the walls is performed as the constant time step used in this analysis is too large to account for such corrections.

To incorporate the deterministic velocities arising from the reduction in diffusivity and porosity inside the rock matrix, a transition zone just inside the solid matrix is defined. The gradients of diffusivity and porosity are assumed to vary linearly over that zone, chosen to be one half of the fracture aperture. Thus, the differences between matrix and fracture diffusivities and log-porosities are calculated and divided by the transition zone thickness to determine gradients in the transition zone. Thus, (6.2) and (6.3) may be expressed as

$$U_{\mathcal{D}} = \frac{2\mathcal{D}_{d_p}(\theta - 1)}{b}, \quad (6.15)$$

and

$$U_{\theta} = \frac{2\mathcal{D}_{d_p} \ln \theta}{b}. \quad (6.16)$$

If a particle is within the matrix and less than a distance of $b/2$ from the fracture wall, $U_{\mathcal{D}}$ and U_{θ} are multiplied by Δt and added to the particle tracking equation in the z -direction as follows:

$$z^m = z^{m-1} + Z(0, 1) \sqrt{2\mathcal{D}_{d_p} \Delta t} \pm U_{\mathcal{D}} \Delta t \pm U_{\theta} \Delta t. \quad (6.17)$$

The sign of the deterministic velocities are opposite to the sign of z , encouraging particles to diffuse back into the fracture, thereby avoiding the uncharacteristic buildup of particles in stagnation and

low porosity zones. Any colloid size distribution (e.g., log-normal, Gaussian, or uniform) can be used in this particle tracking transport model.

6.6.3 Deposition

For the case of perfect sink attachment (employing the Smulochowski–Levich approximation to determine k_f), the fracture walls and channel aperture are discretized into length elements. Each element comprises a segment of the fracture walls, both top and bottom, along the x -direction. A triple nested sorting algorithm arranges the colloids first according to x -location, then size, and finally z -location. At the beginning of every time step, the number of colloids contained within each length element of the fracture is calculated. Within each length element the colloids are subdivided into ten equally sized ‘bins’ according to diameter. The size of each bin is set equal to one tenth of the difference between the largest and smallest colloid diameters of the particles present within the element. Subsequently, the flux of particles onto the surface within each element of each bin is determined according to (6.8). The flux, J , multiplied by the time step, Δt , (rounded to the nearest integer) indicates how many particles sorb onto each length element of the fracture from each bin during each time step. The particles nearest the wall (greatest absolute z -location) are assumed to attach. An exact particle balance is maintained by tagging each adsorbed particle with an integer associated with the length element to which it is attached. The number of attached particles may be plotted against their associated length element. This process is repeated each time step. Because colloids are assumed to sorb irreversibly, desorption is not considered.

When particles undergo kinetic sorption, the fracture wall is also discretized into length elements. Each time a particle comes in contact with the wall, its chance of sorbing is based on the number of previously sorbed colloids, $n_{d_p}^*$, and the particle–wall repulsive energy, ϕ . The number of sorbed colloids in each element of fracture wall is tallied after each particle movement and the sorption probability of a colloid onto an element is calculated according to relationship (6.11) or (6.14). As the number of sorbed colloids increases, the probability of future sorption decreases. The fracture surface area that remains available for deposition depends on the size of the sorbed colloids.

Table 6.1: Model parameters for simulations.

Parameter	Value	Reference
b	1×10^{-4} m	<i>Reimus</i> [1995]
U_{\max}	1×10^{-6} m/s	<i>Reimus</i> [1995]
ν	15	<i>Chrysikopoulos and Abdel-Salam</i> [1997]
Δt	1 s	(5.14)
Δz	2.5×10^{-5} m	
θ	0–0.1	<i>Buckley and Loyalka</i> [1994]
μ_{d_p}	1×10^{-6} m	<i>Ledin et al.</i> [1994]
σ_{d_p}	0.3, 0.6, 0.9 μm	
ϕ	4.04×10^{-19} J/colloid	<i>Adamczyk et al.</i> [1997]

6.7 Simulations and Discussion

6.7.1 Model Parameters

Particle tracking simulations of 150,000 particles were conducted following the previously described procedures. The diameter of each particle, d_p , is assigned a discrete quantized value accurate to one-hundredth of a micrometer. The three log-normal colloid diameter distributions with mean $\mu_{d_p} = 1 \times 10^{-6}$ m and standard deviations $\sigma_{d_p} = 0.3, 0.6,$ and $0.9 \mu\text{m}$ used in this study are shown in Figure 6.2. Unless otherwise specified, the simulations presented in this work are obtained with $U_{\max} = 1 \times 10^{-6}$ m/s, and $b = 1 \times 10^{-4}$ m. Table 6.1 summarizes model parameters.

6.7.2 Comparison with an Analytical Solution

To check the accuracy of the particle tracking algorithms described in this work, concentration distribution curves generated by the analytical solutions of Chapter 4 for the ideal case of monodisperse and polydisperse particle transport in a uniform aperture fracture are compared to appropriate particle tracking results. It is worth discussing how the particle number concentration is determined and how the results are presented. The particle tracking simulation only returns the two-dimensional x - and z -coordinates of each colloid, yet from these data a concentration is to be determined. First the maximum and minimum x -coordinates of all particles are used to calculate the range of values. This range is then divided into equal length subsections or ‘bins’ and the parti-

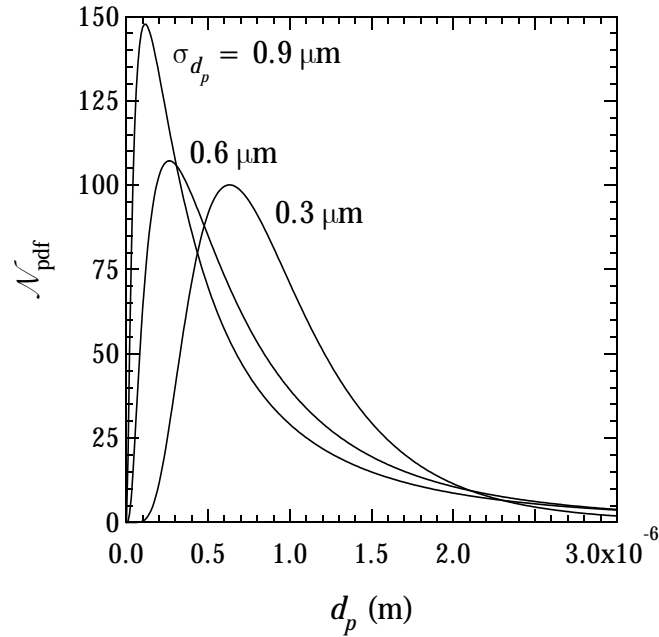


Figure 6.2: Illustration of three log-normal distributions of colloid diameters with $\mu_{d_p} = 1 \times 10^{-6}$ m and $\sigma_{d_p} = 0.3, 0.6,$ and $0.9 \mu\text{m}$.

cles that fall into each bin are counted (as would be done with a histogram). Because the length of the bin is known, as is the aperture, the number of colloids within this area can be presented as an areal concentration (particles/cm²). Similarly, for a three-dimensional fracture the corresponding volume concentrations should be expressed in (particles/cm³). Figure 6.3 shows an excellent agreement between the analytical solutions for monodisperse, (4.12), and polydisperse, (4.16), particle transport and the particle tracking simulations for all colloid plumes studied. Figure 6.3 shows how the monodisperse and three log-normally distributed polydisperse colloid plumes compare to a monodisperse colloid suspension at a distance of 12 m downstream from the fracture inlet (injection point). The larger the range of colloid sizes (large σ_{d_p}), the greater the observed spreading. Thus, by adding an extra degree of heterogeneity to the system (i.e. the distribution of colloid sizes), the spreading of a colloid plume is enhanced. This is analogous to the case of virus transport in porous media (viruses are often considered colloidal particles) where increased spreading is predicted with increased sorption variations caused by fluctuating external conditions [Chrysikopoulos and Sim,

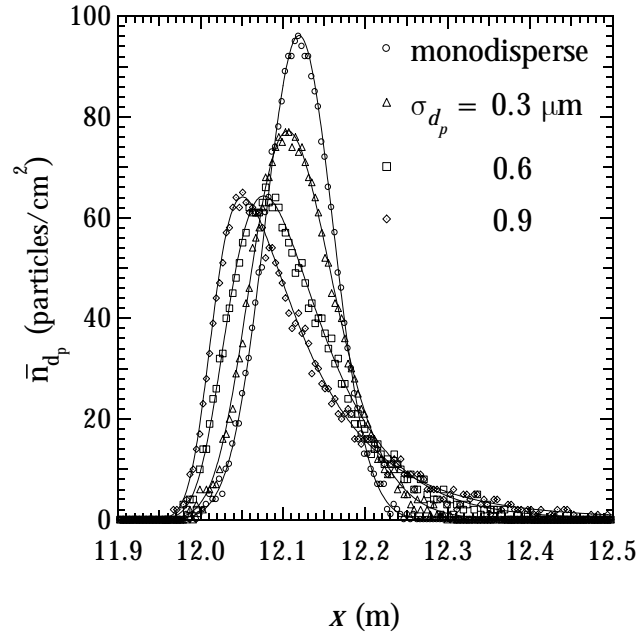


Figure 6.3: Comparison of the analytical solution (solid lines) and the particle tracking simulations for a monodisperse colloid plume (circles) and the three polydisperse colloid plumes with $\mu_{d_p} = 1 \times 10^{-6} \text{m}$ and $\sigma_{d_p} = 0.3 \mu\text{m}$ (triangles), $\sigma_{d_p} = 0.6 \mu\text{m}$ (squares), and $\sigma_{d_p} = 0.9 \mu\text{m}$ (diamonds). Due to the two-dimensional nature of the fracture considered, areal colloid concentrations are presented (here $t = 5,000$ days).

1996]. The introduction of random noise, ubiquitous in random walk methods, is evident as the particle tracking distribution is not completely smooth [Uffink, 1988]. It should be noted that the analytical solutions of Chapter 4 make the simplifying assumption that the effect of longitudinal diffusion is small enough to be neglected. This assumption is not employed in the particle tracking model, but its validity is supported.

6.7.3 Effects on Spreading

To examine the effect of variable size on colloid spreading, for each of the three log-normal diameter size distributions used, the predicted particle plume, at the end of 5,000 hours of simulation time, was divided into three groups with equal number of particles (50,000 particles). Histograms of colloid diameters for the three groups of each polydisperse plume are presented in Figure 6.4. The

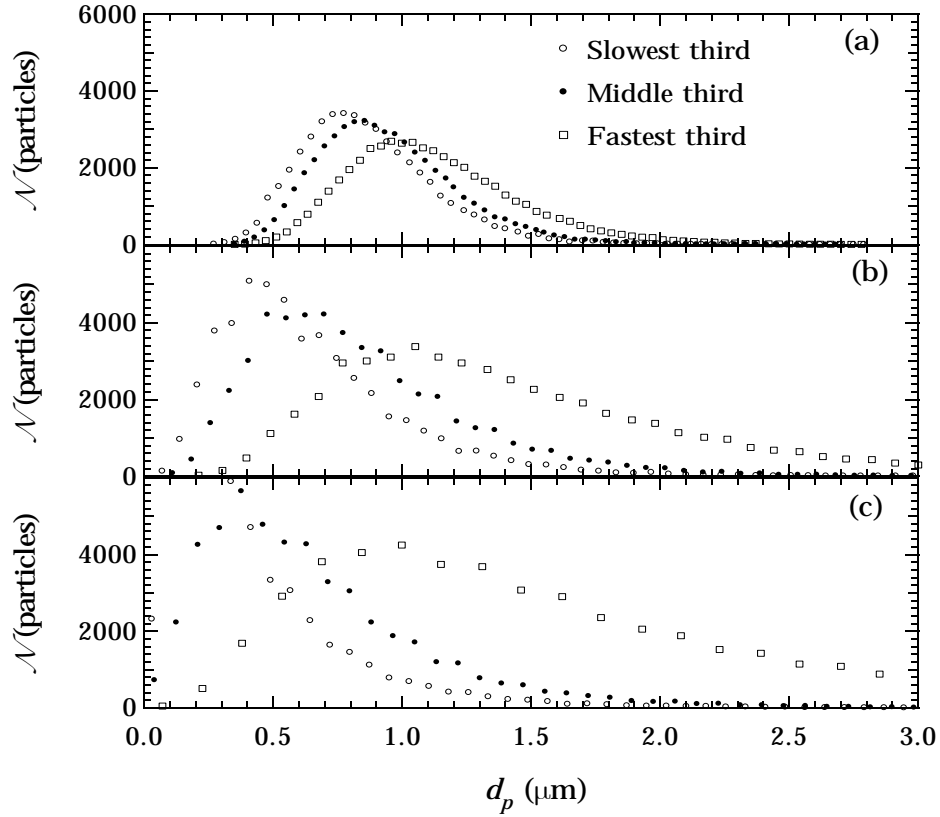


Figure 6.4: Number of colloids with a given diameter for plumes of colloids with log-normal diameter distributions with $\mu_{d_p} = 1 \times 10^{-6} \text{ m}$ and (a) $\sigma_{d_p} = 0.3 \text{ } \mu\text{m}$, (b) $\sigma_{d_p} = 0.6 \text{ } \mu\text{m}$, and (c) $\sigma_{d_p} = 0.9 \text{ } \mu\text{m}$ (here $t = 5,000 \text{ h}$). The colloids have been divided into thirds based on their travel distances. The squares represent the fastest third, the closed circles the middle third, and the open circles the slowest third (closest to the inlet).

first group is indicated in Figure 6.4 with open circles and represents the slowest colloids; that is, the colloids located nearest to the fracture inlet at the end of the specified simulation time. The second group is indicated by the filled circles and represents the portion of the particles that are located in the middle of the colloid plume. The third group is indicated by squares and represents the particles that have traveled farthest within the fracture. Although the distribution of each group retains a log-normal shape, it is clear that a separation of colloids based on size is occurring. The larger colloids travel further and faster than the smaller colloids. This result is expected based on a colloid's finite dimensions prohibiting it from contacting the slowest moving fluid near the fracture

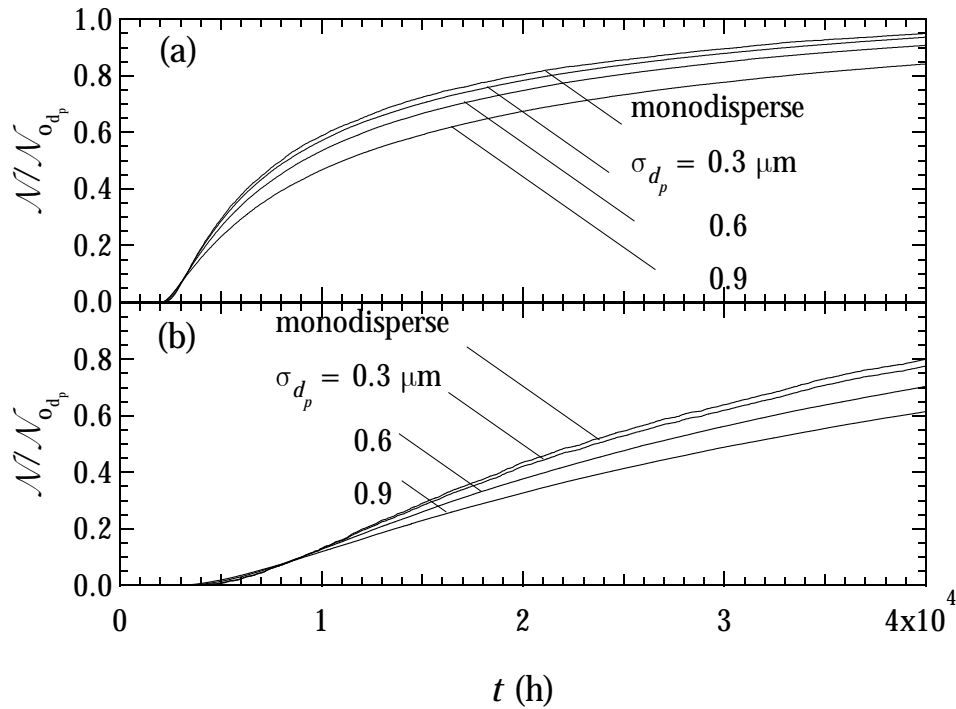


Figure 6.5: Normalized cumulative breakthrough curves for plumes of colloids having different log-normal distribution of particle diameters in a fracture with uniform aperture and (a) 1% and (b) 10% solid matrix porosity (here $x = 5$ m).

boundaries and thereby forcing it to be advected at a velocity faster than the mean fluid velocity. Clearly, Figure 6.4 shows that, on average, the largest colloid particles are transported faster than the smaller particles.

6.7.4 Effects of Matrix Diffusion

The effect of matrix diffusion on colloid breakthrough curves at a distance of 5 m from the fracture inlet for the monodisperse and the three log-normal colloid size distributions is illustrated in Figure 6.5. Clearly, differences in colloid size distribution lead to distinct cumulative breakthrough patterns. The higher the standard deviation of the colloid size distribution, the more pronounced the retardation of the colloid plume. In particular, the plume with $\sigma_{d_p} = 0.9 \mu\text{m}$ contains the largest number of small colloids. These smaller particles are transported slowest not only because they can

sample the slowest moving portion of the parabolic velocity profile (nearest to the wall), but because smaller colloids preferentially diffuse into the rock matrix.

The probability for diffusion into the fracture wall is dependent on the matrix porosity alone. However, the number of times that a colloid contacts the wall is a function of its diffusion coefficient. Due to their large diffusion coefficient (large diffusive travel distance per time step), smaller particles are more likely to come into contact with the fracture wall. Each time a particle contacts the wall there is a specified probability that it will diffuse into it. The more often a particle encounters a wall, the higher the chance that it will eventually diffuse into the solid matrix. The deterministic velocities added to the particle tracking equations assure back diffusion into the fracture once the bulk of the colloid cloud has passed. Although some particles are effectively lost from the system by diffusing well into the rock matrix (past the transition zone), many return to the fracture by the concentration gradient remaining when few colloids are left in the fracture. Smaller colloids are more likely to diffuse into (and be transported out of) the matrix. This effectively increases the residence time of small colloids and retards the breakthrough of large variance colloid plumes with many small constituents.

6.7.5 Colloid Deposition

6.7.5.1 Perfect Sink Sorption

Figure 6.6 presents sorbed colloid concentrations, $n_{d_p}^*$, after 5,000 hours of simulation time for each of the three colloid suspension considered ($\sigma_{d_p} = 0.3, 0.6,$ and $0.9 \mu\text{m}$). The results for the two-dimensional fracture considered here are presented in units of (particles/cm); however, for a fully three-dimensional fracture the corresponding units are (particles/cm²). The colloids are divided into three groups of 50,000 particles according to diameter. It is evident from Figure 6.6 that the smallest colloids show the highest sorbed concentration. Preferential sorption of small colloids occurs. Also, the number of deposited colloids as a function of fracture length follows an $x^{-\frac{1}{3}}$ dependence as indicated by the flux relationship (6.8). The concentration of colloids in the liquid phase decreases as more colloids sorb onto the fracture surface.

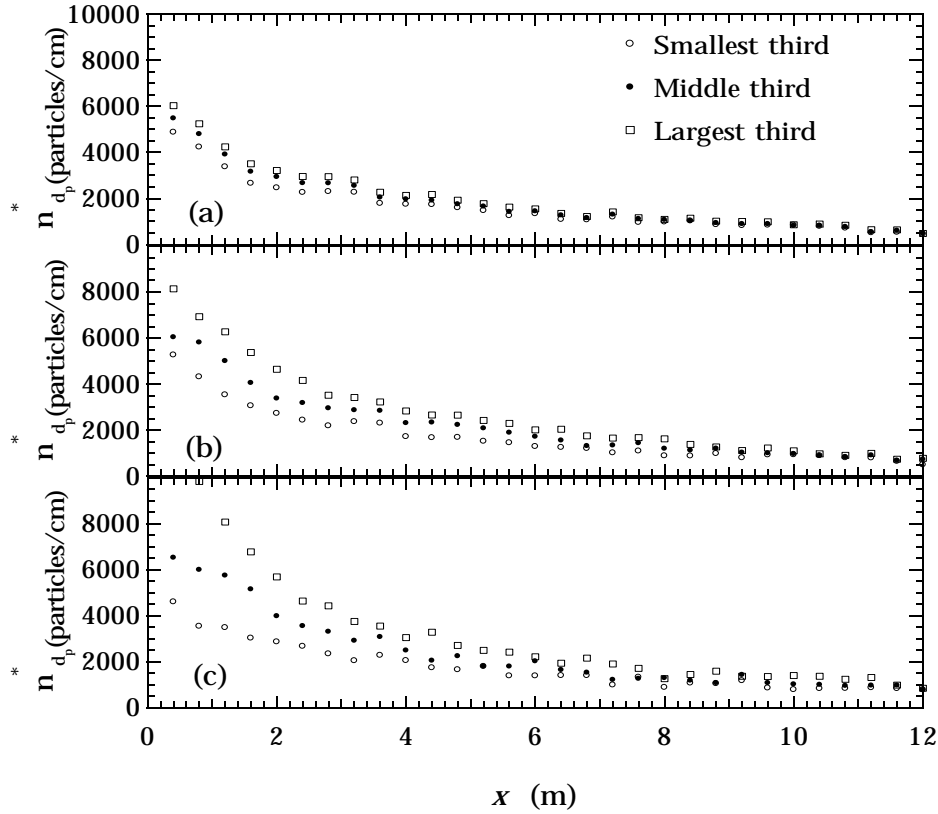


Figure 6.6: Sorbed colloid concentrations under perfect sink conditions as a function of fracture length for colloid plumes having log-normal diameter distribution with $\mu_{d_p} = 1 \times 10^{-6}$ m and (a) $\sigma_{d_p} = 0.3 \mu\text{m}$, (b) $\sigma_{d_p} = 0.6 \mu\text{m}$, and (c) $\sigma_{d_p} = 0.9 \mu\text{m}$. The colloids have been divided into thirds based on their diameter. The open circles represent the smallest third, the closed circles the middle third, and the squares the largest third (here $t = 5,000$ h).

6.7.5.2 Kinetic Sorption

Figure 6.7 shows snapshots of the sorbed colloid concentrations, $n_{d_p}^*$, under linear kinetic sorption conditions for each of the three log-normal colloid distributions considered in this study ($\sigma_{d_p} = 0.3, 0.6$, and $0.9 \mu\text{m}$). Because of their larger diffusion coefficients, preferential sorption of small colloids over larger colloids is expected as they will contact the wall more frequently than larger colloids. This is clearly illustrated in Figure 6.7 where the colloid suspension with $\sigma_{d_p} = 0.9 \mu\text{m}$ (composed of the largest number of small colloids), exhibits the greatest sorption near the entrance to the fracture.

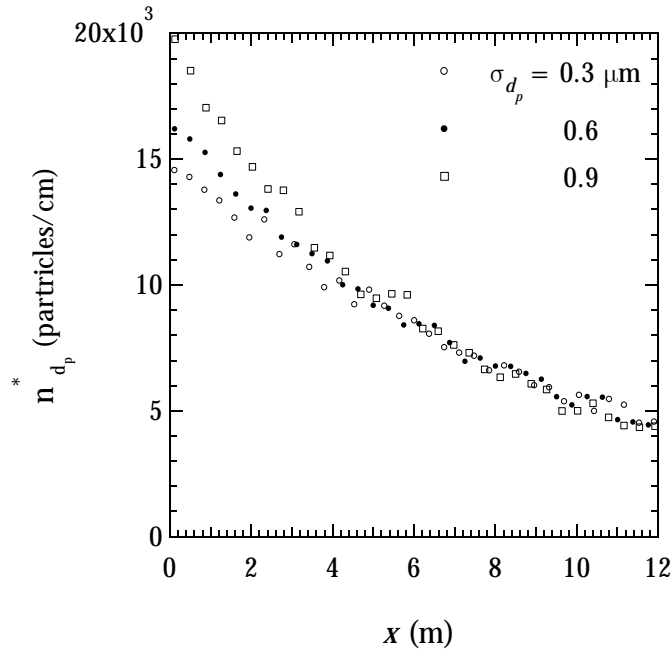


Figure 6.7: Overall sorbed colloid concentrations under linear DBF kinetic sorption conditions as a function of fracture length for the three polydisperse colloid plumes (here $t = 5,000$ h and $\phi = 10kT$). Due to the two-dimensional nature of the fracture considered, sorbed colloid concentrations per unit length are presented.

Figure 6.8 presents the colloids divided into three equal groups of 50,000 particles arranged according to diameter to reveal a trend of preferential sorption. The group comprising the largest third of colloids exhibits the least sorption while the group of the smallest third of colloids yields the highest concentration of sorbed colloids. As smallest particles have the largest Brownian diffusion, they come into contact with the fracture wall more often than the larger particles, and consequently have a higher sorption rate as is supported by Figure 6.8. Figure 6.9 compares the effect of linear and nonlinear DBFs on sorbed colloid concentrations. The results are comparable for all three polydisperse plumes with the nonlinear DBF leading to slightly lower sorbed colloid concentrations than the linear case. In view of (6.14), this is an expected result, because for a small concentration of sorbed particles, the nonlinear DBF behaves similarly to the linear DBF. Only for a relatively large concentration ($\epsilon \geq \epsilon_{\max}/10$) of sorbed particles per length element does the nonlinear case substantially deviate from the linear DBF in the form of a reduced sorption probability.

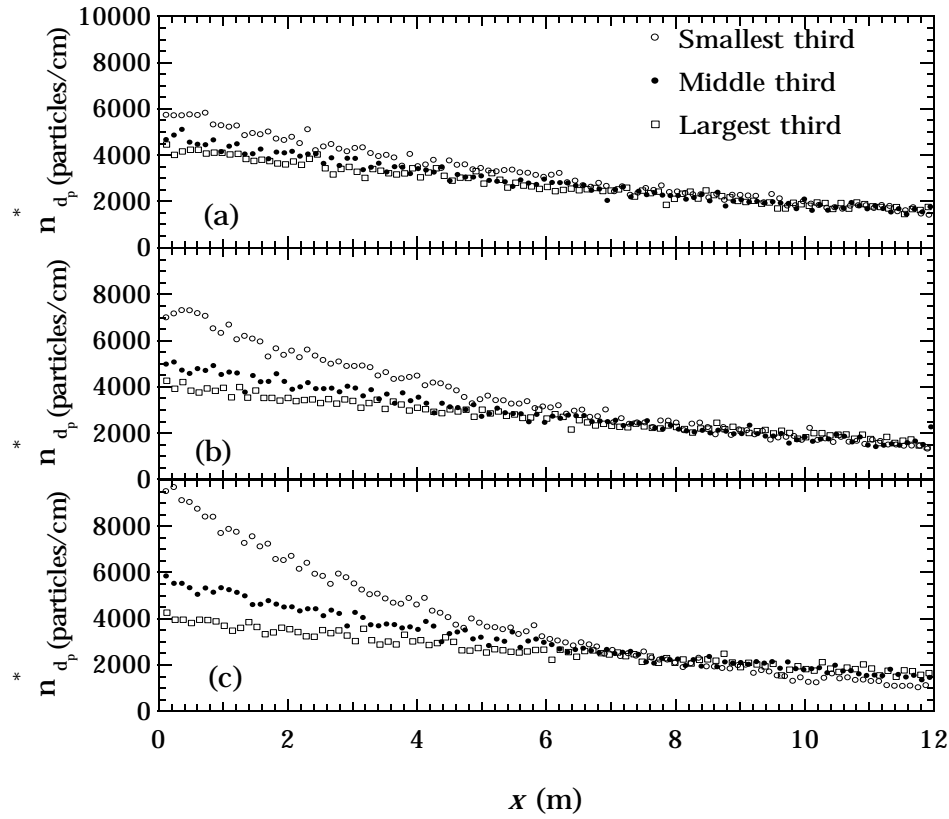


Figure 6.8: Sorbed colloid concentrations under linear kinetic sorption conditions as a function of fracture length for colloid plumes having log-normal diameter distributions with $\mu_{d_p} = 1 \times 10^{-6}$ m and (a) $\sigma_{d_p} = 0.3 \mu\text{m}$; (b) $\sigma_{d_p} = 0.6 \mu\text{m}$; and (c) $\sigma_{d_p} = 0.9 \mu\text{m}$. The colloids have been divided into thirds based on their diameter size (here $t = 5,000$ h and $\phi = 10kT$).

6.7.6 Effect of Varied Fracture Aperture

To examine the effect of fracture aperture on colloid deposition onto fracture walls, particle tracking simulations were conducted for fractures with distinct apertures while keeping all other transport parameters constant. A monodisperse colloid suspension is employed. Furthermore, it is assumed that colloids follow a linear kinetic sorption relationship. The results presented in Figure 6.10 indicate that the number sorbed colloids varies inversely to the aperture. The number of kinetically sorbed colloids from a monodisperse suspension decreases with increasing fracture aperture. As the aperture is increased, a colloid will contact the wall less frequently. *Abdel-Salam and Chrysikopoulos* [1994, 1995a, b] proposed an expression for the mass flux of colloids onto fracture surfaces with equivalent consequences.

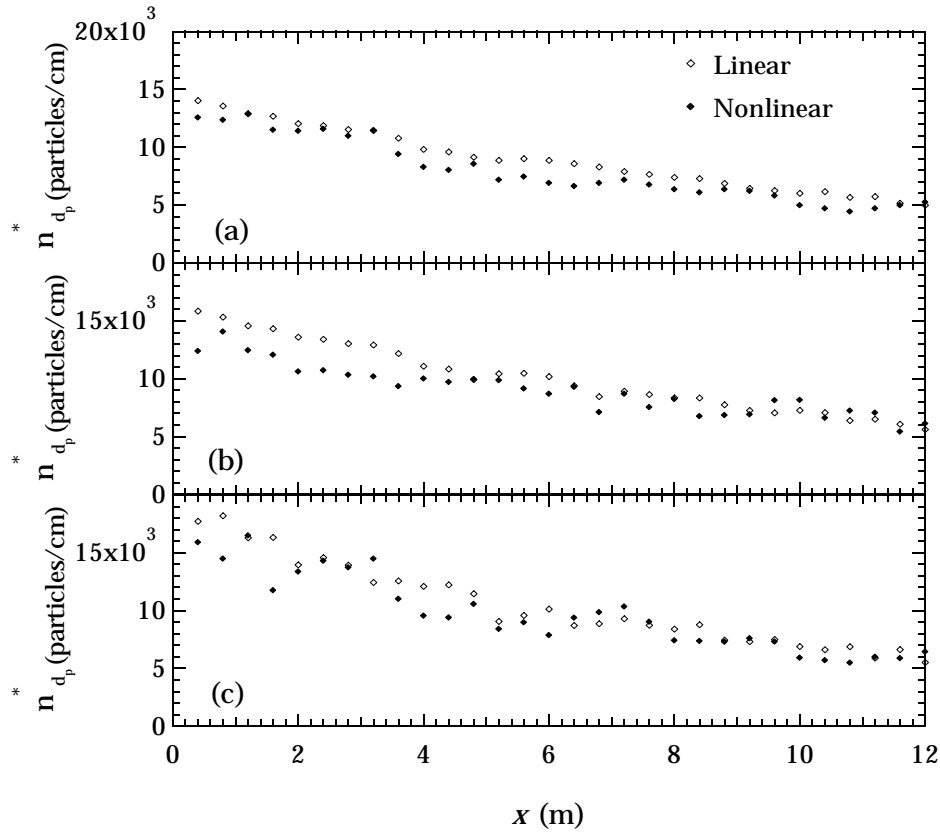


Figure 6.9: Effect of linear (open diamonds) and nonlinear (closed diamonds) DBFs on sorbed colloid concentrations along the fracture for colloid plumes having log-normal diameter distribution with $\mu_{d_p} = 1 \times 10^{-6} \text{m}$ and (a) $\sigma_{d_p} = 0.3 \mu\text{m}$; (b) $\sigma_{d_p} = 0.6 \mu\text{m}$; and (c) $\sigma_{d_p} = 0.9 \mu\text{m}$.

6.8 Summary and Conclusions

In this chapter, the transport of polydisperse colloid plumes in a fully saturated fracture with a uniform aperture was modeled by particle tracking techniques. Both the effects of matrix diffusion and surface sorption were individually investigated. Simulation results show that polydisperse colloid suspensions exhibit transport characteristics that differ from monodisperse suspensions. The observed spreading of polydisperse colloid plumes is proportional to the standard deviation of the colloid diameter distribution. Large colloids have larger effective velocities than smaller colloids resulting in faster transport times leading to increased spreading of a polydisperse plume. Cumulative breakthrough curves of polydisperse colloid suspensions in fractures with different matrix porosities

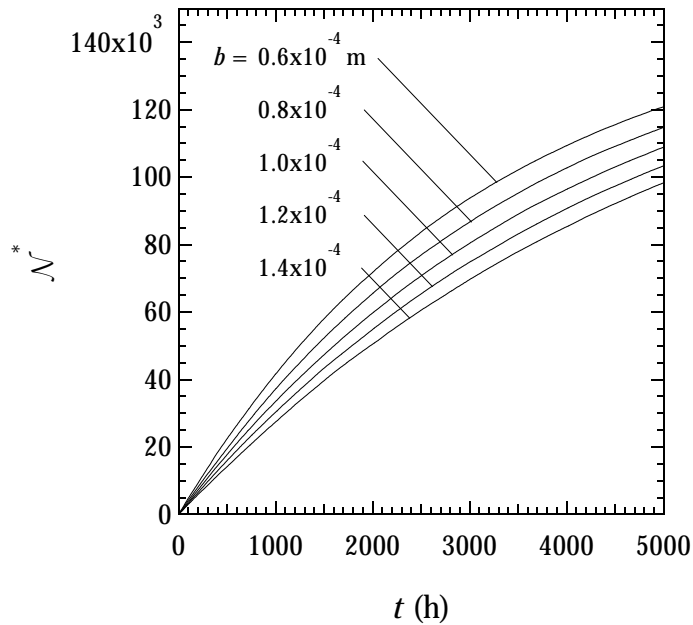


Figure 6.10: Total number of sorbed colloids from a monodisperse suspension ($d_p = 1 \times 10^{-6} \text{m}$) as a function of time for several different fracture apertures (here $x = 5 \text{ m}$).

indicate that a plume with larger standard deviation in colloid diameter becomes progressively retarded, owing to the increased number of small colloids that are more often trapped in the solid matrix. It can be concluded that the increased retardation for colloid plumes with higher standard deviation in colloid diameter is due to both the slower effective velocity of the smallest particles and their preferential diffusion into the solid matrix. Particle size affects colloid sorption with the smallest particles preferentially sorbing onto the fracture walls. The linear and nonlinear kinetic sorption DBF models examined show different sorbed colloid distributions when the fracture surface area covered by the sorbed colloids is relatively large, but similar results when sorbed colloid concentrations are low. Furthermore, it was demonstrated that the number of sorbed particles is inversely proportional to the fracture aperture. This investigation lays the groundwork for the next chapter that models the more realistic situation of reactive colloid transport in a variable aperture fracture.

Chapter 7

Transport in a Variable Aperture Fracture

7.1 Introduction

In Chapter 6 it was shown that polydisperse (log-normally distributed) colloid plumes exhibit greater spreading than monodisperse suspensions when flowing in a single, uniform aperture fracture. Furthermore, it was shown that larger particles are least retarded when the effects of matrix diffusion and surface sorption are included. In this chapter, the previous research efforts are extended to investigate the transport of polydisperse colloid distributions in a two-dimensional fracture with spatially variable aperture under both sorbing and non-sorbing conditions. Matrix diffusion of colloids is not considered in this chapter.

7.2 Fracture Generation

Figure 7.1 is an illustration of the system modeled in this work. The quasi-three-dimensional fracture used in this study is 8 m long (x -direction) and 4 m wide (y -direction). The fracture

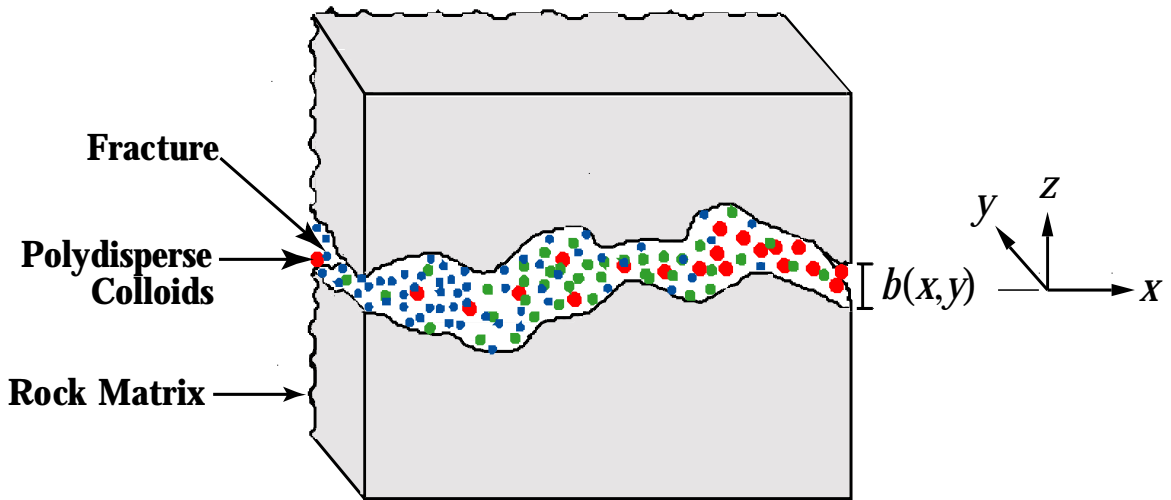


Figure 7.1: Schematic illustration of a quasi-three-dimensional fracture with spatially variable aperture $b(x, y)$ and a migrating plume of polydisperse colloids undergoing surface sorption. Note that $z = 0$ at the center of the fracture.

plane is partitioned into 3,200 discrete square elements. Each 10×10 cm element exhibits a distinct aperture and is represented by a contour plot of the fracture apertures in Figure 7.2. The aperture field is generated stochastically by the geostatistical code SPRT2D [Gutjahr, 1989]. It is assumed that the aperture distribution in the fracture plane follows a log-normal distribution [Johns *et al.*, 1993; Reimus *et al.*, 1993; Keller, 1998] with preselected mean, $\mu_{\ln b}$, and variance, $\sigma_{\ln b}^2$. Furthermore, the aperture distribution is assumed to vary spatially according to an isotropic exponential autocovariance function with specified correlation length, ξ_b . By definition, a correlation length implies that for distances in the fracture plane smaller than the correlation length the aperture values are likely to be similar, but at distances larger than the correlation length there is no correlation between apertures. Unique realizations of the aperture field are obtained by changing the seed number of the random field generator.

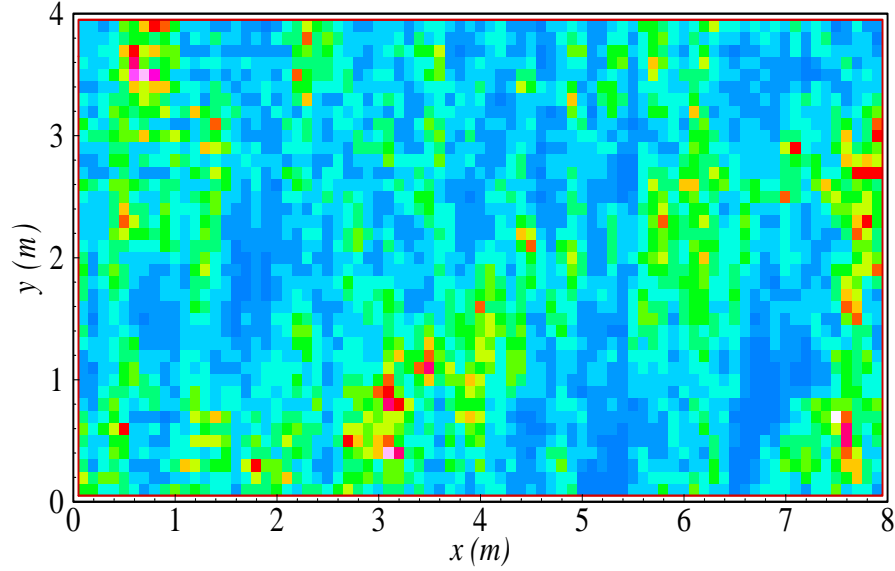


Figure 7.2: A realization of the aperture spatial distribution in the fracture plane. The fracture is partitioned into 80×40 equal-size elements. The varied shades illustrate apertures between 0.01 and 0.15 mm (here $x = 8$ m, $y = 4$ m, $\bar{b} = 1 \times 10^{-4}$ m, $\sigma_{\ln b}^2 = 0.15$, and $\xi_b = 1$ m).

7.3 Flow in a Fracture

7.3.1 Mathematical Model

The two-dimensional, steady-state partial differential equation describing flow within a spatially variable aperture fracture is [Chrysikopoulos and Abdel-Salam, 1997]

$$\frac{\partial}{\partial x} \left[b^3(x, y) \frac{\partial h(x, y)}{\partial x} \right] + \frac{\partial}{\partial y} \left[b^3(x, y) \frac{\partial h(x, y)}{\partial y} \right] = 0, \quad (7.1)$$

where $b(x, y)$ is the local fracture aperture; and h is the piezometric head. The preceding equation assumes that the cubic law (Reynolds equation) for incompressible laminar flow between two parallel plate elements can effectively simulate the average flow at every point within the fracture [Dijk et al., 1999]. Brown et al. [1995] has shown that the cubic law tends to overestimate fluid velocity in low aperture areas; however, variable aperture fractures will channelize flow thereby minimizing overall error for the cumulative breakthrough curves obtained using this approximation. The above equation is a stochastic partial differential equation, because one of its parameters, namely $b(x, y)$, is a stochastic variable.

For each realization of the aperture field, a distribution of the piezometric head within the fracture is obtained by solving the governing fluid flow equation (7.1) subject to constant head (Dirichlet) boundary conditions along the $x = 0$ and $x = 8$ m sides of the fracture. A net flow is induced in the positive x -direction with the incorporation of no-flow (Neumann) boundary conditions along the sides of the fracture at $y = 0$ and $y = 4$ m. Flow in the rock matrix is neglected because the saturated hydraulic conductivity in the rock matrix is several orders of magnitude smaller than the saturated hydraulic conductivity in the fracture [Abdel-Salam and Chrysikopoulos, 1996]. A grid of 3,321 (81×41) nodes is laid over the two-dimensional fracture (system of elements) considered here, and the piezometric head is determined at each unknown node.

7.3.2 Numerical Formulation

For each realization of the aperture field, the following five-point central finite difference numerical approximation is employed for the solution of the governing flow equation [Hoffman, 1992, p. 411]

$$b_{i,j+1/2}^3 h_{i,j+1} + b_{i,j-1/2}^3 h_{i,j-1} + b_{i+1/2,j}^3 h_{i+1,j} + b_{i-1/2,j}^3 h_{i-1,j} - h_{i,j} \left(b_{i,j+1/2}^3 + b_{i,j-1/2}^3 + b_{i+1/2,j}^3 + b_{i-1/2,j}^3 \right) = 0, \quad (7.2)$$

where the subscripts i and j are the discretized distance in the x - and y -directions, respectively. The five-point finite difference stencil is shown in Figure 7.3. The aperture at the interface of two adjacent elements in the x - and y -directions are obtained by employing the harmonic mean (derived in Appendix C)

$$b_{i,j\pm 1/2}^3 = \frac{2b_{i,j}^3 b_{i,j\pm 1}^3}{b_{i,j}^3 + b_{i,j\pm 1}^3}, \quad (7.3)$$

$$b_{i\pm 1/2,j}^3 = \frac{2b_{i,j}^3 b_{i\pm 1,j}^3}{b_{i,j}^3 + b_{i\pm 1,j}^3}. \quad (7.4)$$

Using the central finite difference numerical approximation (7.2) for the solution of the governing flow equation for each node on the grid of the fracture plane results in a set of linear

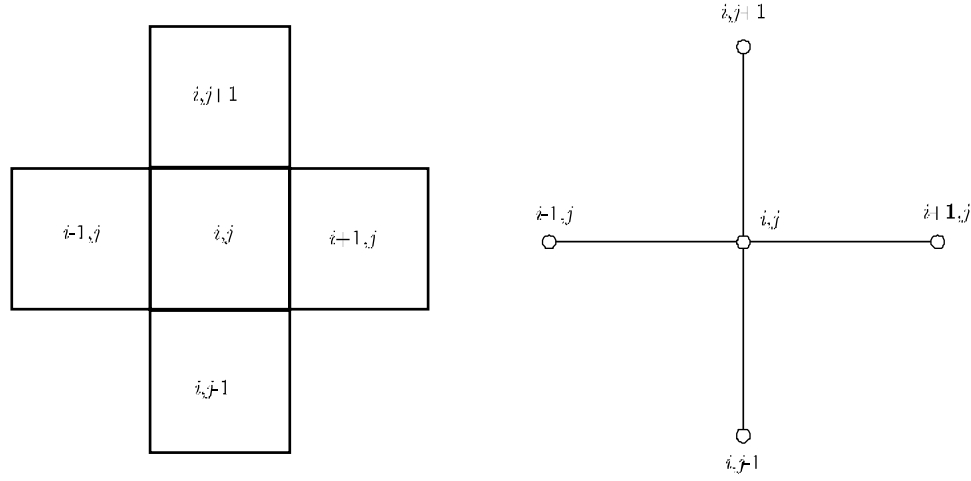


Figure 7.3: Five-point finite difference stencil.

equations with as many unknowns as the number of unspecified nodes on the fracture grid [Hoffman, 1992, p. 825]. The resulting set of linear equations is solved using a banded LU decomposition matrix solving algorithm [Press *et al.*, 1992, p. 963]. Average velocity components in the x - and y -directions are then calculated for every unit element from the steady-state volumetric fluxes by the following expressions:

$$\bar{u}_x = -\frac{\gamma b^2(x, y)}{12\mu} \frac{\partial h(x, y)}{\partial x}, \quad (7.5)$$

$$\bar{u}_y = -\frac{\gamma b^2(x, y)}{12\mu} \frac{\partial h(x, y)}{\partial y}, \quad (7.6)$$

Second order accurate finite difference forms of (7.5) and (7.6) used in this analysis are

$$\bar{u}_{x,i,j} = -\frac{\gamma b_{i,j}^2}{12\mu} \frac{h_{i+1,j} - h_{i-1,j}}{2\Delta x}, \quad (7.7)$$

$$\bar{u}_{y,i,j} = -\frac{\gamma b_{i,j}^2}{12\mu} \frac{h_{i,j+1} - h_{i,j-1}}{2\Delta y}. \quad (7.8)$$

Because a parabolic velocity profile develops within each element, the velocities in the x - and y -directions are functions of z

$$u_x(x, y, z) = \bar{u}_x(x, y) \frac{3}{2} \left\{ 1 - 4 \left[\frac{z}{b(x, y)} \right]^2 \right\}, \quad (7.9)$$

$$u_y(x, y, z) = \bar{u}_y(x, y) \frac{3}{2} \left\{ 1 - 4 \left[\frac{z}{b(x, y)} \right]^2 \right\}, \quad (7.10)$$

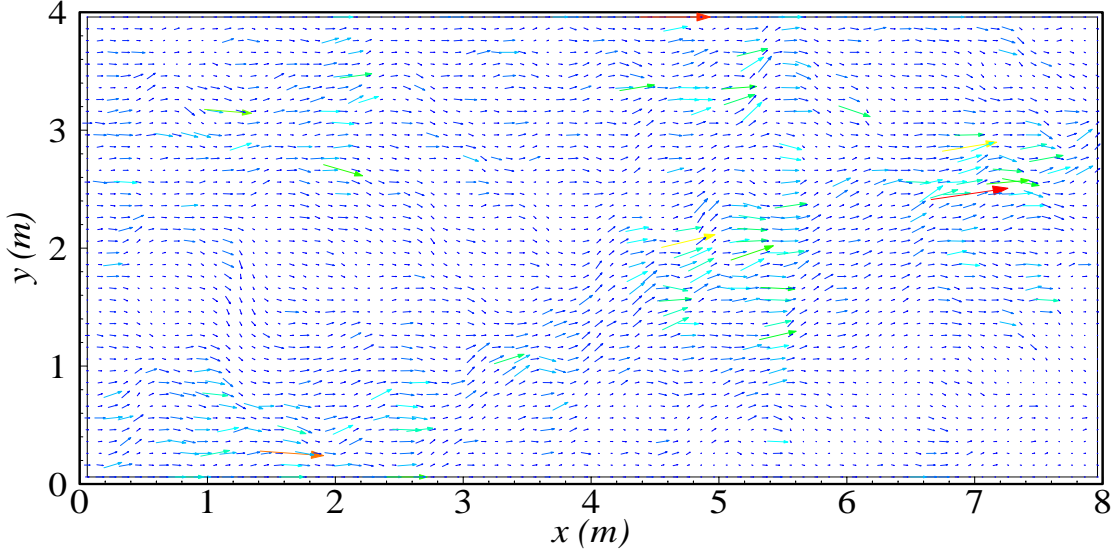


Figure 7.4: The velocity field in the variable aperture fracture shown in Figure 7.3. Arrow lengths are tangential and proportional to the local mean velocities.

where z is the direction normal to the fracture surface. Equations (7.9) and (7.10) are consequences of the no slip boundary conditions at the fracture walls, and are spatial functions of the (x, y, z) location in the fracture. Figure 7.4 is a vector plot of the velocity field.

7.4 Algorithm Development

7.4.1 Particle Tracking

The new particle tracking algorithm developed in Chapter 5 is employed in these simulations; however, three dimensions need to be considered. By substituting (7.9) and (7.10) into the vector particle tracking equation, (5.16), the overall transport equations for the problem examined in this work are:

$$x^m = x^{m-1} + \bar{u}_x(x^{m-1}, y^{m-1}) \frac{3}{2} \left\{ 1 - 4 \left[\frac{z^{m-1}}{b(x, y)} \right]^2 \right\} \Delta t + Z(0, 1) \sqrt{2\mathcal{D}_{dp} \Delta t}, \quad (7.11)$$

$$y^m = y^{m-1} + \bar{u}_y(x^{m-1}, y^{m-1}) \frac{3}{2} \left\{ 1 - 4 \left[\frac{z^{m-1}}{b(x, y)} \right]^2 \right\} \Delta t + Z(0, 1) \sqrt{2\mathcal{D}_{dp} \Delta t}, \quad (7.12)$$

$$z^m = z^{m-1} \pm \Delta z. \quad (7.13)$$

Again, a characteristic spatial step in the z -direction is specified and the associated time for the particle to travel this distance is calculated from (5.14). Once the time step associated with a particle's movement of Δz is determined, the corresponding distances moved by the particle in the x - and y -directions are determined from (7.11) and (7.12), respectively.

7.4.2 Numerical Methods

In these simulations, 10,000 colloids are introduced at the inlet side of the fracture flow domain ($x = 0$) and distributed according to the local volumetric flow rate as suggested by *Reimus* [1995, p. 93]. A discrete cumulative probability density function based on the volumetric flow rate into each inlet element of the fracture is constructed by summing all individual element flow rates at the fracture inlet and determining each element's contribution (probability) to the total sum. Subsequently, a uniform random number between zero and one is generated for each particle. The random number's placement in the cumulative distribution of the flow rates at the inlet designates the corresponding entrance element. Once the element, j , is specified, a particle's exact y -location in meters is found according to the equation:

$$y = \frac{(j - 1) + Rn(0, 1)}{10}, \quad (7.14)$$

where $Rn(0, 1)$ is a uniformly distributed random number between 0 and 1. As in Chapter 6, it is assumed that the probability of a colloid entering a designated element of the fracture inlet at a given z -location (perpendicular to the fracture walls) is proportional to the flow rate at that particular position. Consequently, the probability of a colloid having a starting position less than z is

$$P(z) = -2 \left[\frac{z}{b(0, y)} \right]^2 + \frac{3}{2} \frac{z}{b(0, y)} + \frac{1}{2}. \quad (7.15)$$

A uniform random number between zero and one is substituted for $P(z)$ in (7.15) and the roots of the resulting polynomial in z are evaluated by Newton's Method. Roots found outside of the range of $-b(0, y)/2$ and $b(0, y)/2$ are ignored and colloids must be wholly contained within the fracture.

For an impermeable solid matrix all particles are assumed to be reflected from fracture walls as in a mirror image without loss of energy if they do not sorb. That is, the final x - and y -coordinates position remain unchanged, whereas the final z location is placed a distance away from the wall equal to the distance that the particle would have obtained if it had penetrated the rock matrix plus the particle diameter.

Particle movements between elements of different aperture are assumed to follow the relationship [*Happel and Brenner*, 1965, p. 553]

$$\frac{z_{\text{old}}}{b_{\text{old}}} = \frac{z_{\text{new}}}{b_{\text{new}}}, \quad (7.16)$$

which is applicable for creeping flow conditions in slowly converging or diverging channels. Thus the ratio of the new z -location to the old z -location is equivalent to the ratio of the fracture aperture at the new location to the fracture aperture at the old location. Particle are allowed to cross both perpendicularly as well as diagonally between elements; however, if the particle crosses diagonally only its initial and final element apertures are used in (7.16).

7.5 Particle Deposition

The transport of colloids in fractured media is significantly affected by colloid deposition onto formation surfaces. The probability of a particle sorbing per wall collision (attachment efficiency), was described in Chapter 6 and the same methodology is used here. The effect of previously deposited colloids is taken into account through use of the linear DBF, (6.11). The value of a DBF ranges between one (for a fracture free of colloids) and zero (for a fracture surface completely covered by deposited colloids). Only the linear DBF is considered in the case of the variable aperture fracture because it is not expected to significantly differ from the nonlinear DBF. The modified Boltzmann law, (6.10), is incorporated into the particle tracking simulation as follows: each time a particle-wall encounter is recorded, first the probability p is determined and then a uniform random number between zero and one is generated. Particle attachment is assumed to occur if the selected random number is less than or equal to $pF(n_{d_p}^*)$.

7.6 Model Simulations

One monodisperse and three polydisperse colloid size distributions are examined here. All distributions have the same mean colloid diameter, $\mu_{d_p} = 1 \mu\text{m}$, and the three polydisperse colloid distributions are log-normally distributed with standard deviations in the colloid diameter of $\sigma_{d_p} = 0.3, 0.6,$ and $0.9 \mu\text{m}$ as shown in Figure 6.2.

The hypothetical fracture used in this work is subjected to a hydraulic gradient of 0.031 in the x -direction. Cumulative colloid number, \mathcal{N} , exiting the fracture at $x = 8 \text{ m}$, normalized by the initial liquid phase colloid number, $\mathcal{N}_{o_{d_p}}$, is evaluated by averaging the results from fifty realizations of the fracture aperture field. The number of realizations is chosen such that additional realizations do not change the calculated ensemble averages by more than 2%. Furthermore, the spatial step in the z -direction, Δz , is set equal to $1/4^{\text{th}}$ of the local fracture aperture. This distance was chosen in order to assure reasonable accuracy from the particle tracking program by allowing a particle to sample all portions of the velocity profile.

Figure 7.5 qualitatively illustrates the effect of colloid diameter distribution, fracture aperture variability, and colloid sorption on the transport of $\mathcal{N}_{o_{d_p}} = 10,000$ colloid particles in water saturated fractures. Four different cases are considered when the colloids have been in the system for approximately half of the mean total travel time for the fracture. The first case (Figure 7.5a) represents a fracture with uniform aperture, $b = 1 \times 10^{-4} \text{ m}$, and a plume of monodisperse colloids with particle diameter $1 \mu\text{m}$. The second case (Figure 7.5b) represents a fracture with uniform aperture ($b = 1 \times 10^{-4} \text{ m}$) and a plume of polydisperse colloids with log-normal diameter distribution described by a mean particle diameter of $\mu_{d_p} = 1 \mu\text{m}$ and standard deviation $\sigma_{d_p} = 0.9 \mu\text{m}$. It should be noted that this polydisperse plume is divided into three equally numbered groups based on diameter. The triangles represent the smallest third, the squares represent the middle third, and the circles represent the largest third. The next case (Figure 7.5c) represents a fracture with mean aperture $\bar{b} = 1 \times 10^{-4} \text{ m}$, variance of the log-transformed spatially variable aperture $\sigma_{\ln b}^2 = 0.037$,

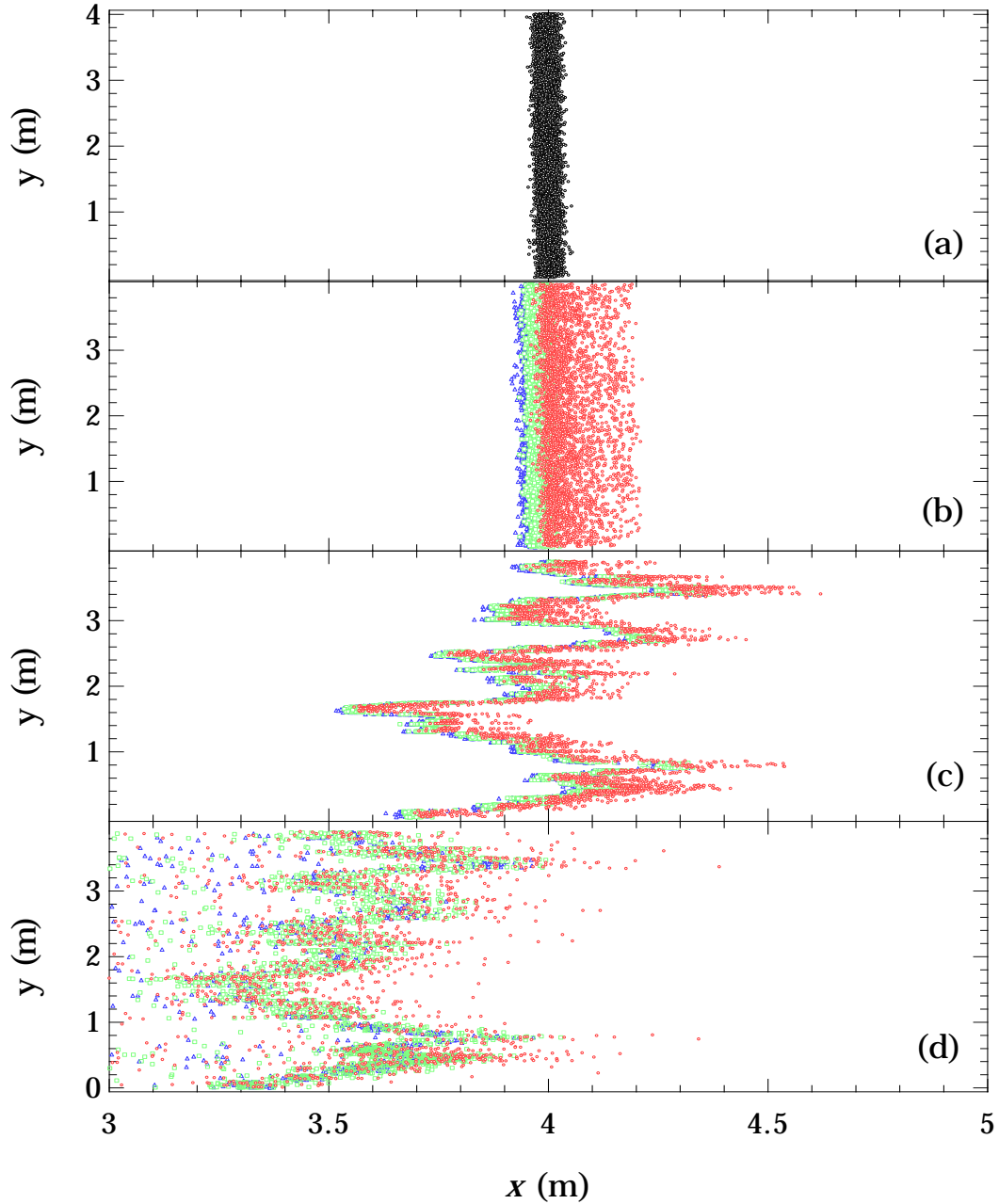


Figure 7.5: Snapshots of colloid positions (flow from left to right) for (a) a monodisperse colloid plume in a uniform aperture fracture; (b) a polydisperse colloid plume in a uniform aperture fracture; (c) a polydisperse colloid plume in a variable aperture fracture; and (d) a polydisperse colloid plume undergoing sorption in a variable aperture fracture. The polydisperse colloid plumes are split into thirds based on particle size with triangles being the smallest third, squares the middle third, and circles the largest third (here $t = 17.5$ hr).

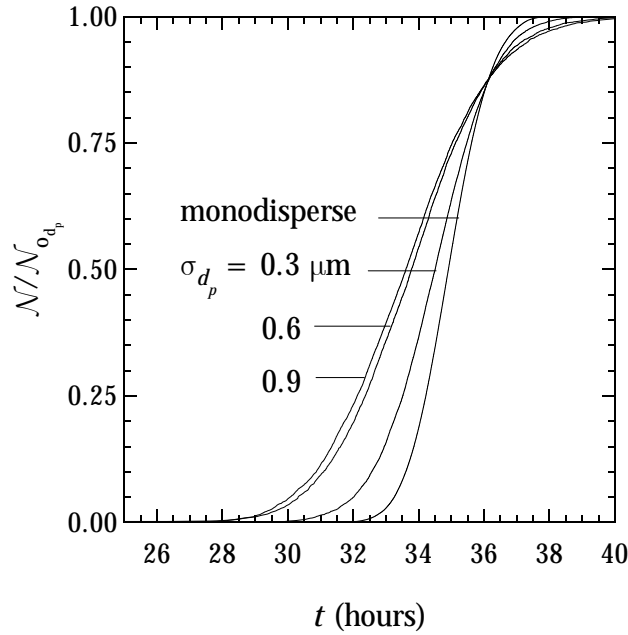


Figure 7.6: Normalized cumulative colloid breakthrough curves for a monodisperse and three polydisperse colloid plumes with mean diameter $\mu_{d_p} = 1 \mu\text{m}$ in a uniform fracture with aperture $b = 1 \times 10^{-4}$ m.

correlation length of the apertures $\xi_b = 1$ m, and the identical plume of polydisperse colloids used in the previous case. Finally, the last case (Figure 7.5d) represents the same situation as the third case with the additional constraint that the polydisperse colloids may undergo irreversible sorption. It should be noted that colloids sorbed onto the fracture surfaces as well as colloids in suspension are presented in Figure 7.5d with sorbed colloids showing significant retardation. Comparison of the four cases reveals that: polydisperse colloid suspensions spread more within the fracture than monodisperse suspensions (see Figures 7.5a, b); larger colloids travel fastest (see Figure 7.5b); aperture variability leads to preferential flow paths (see Figure 7.5c); and that the smallest colloids of the plume are preferentially sorbed as more of the smaller colloids lag the larger colloids (Figure 7.5d).

Normalized colloid breakthrough curves of the four colloid plumes considered in this study are presented in Figure 7.6 for the case of transport in a uniform aperture fracture. Clearly, the

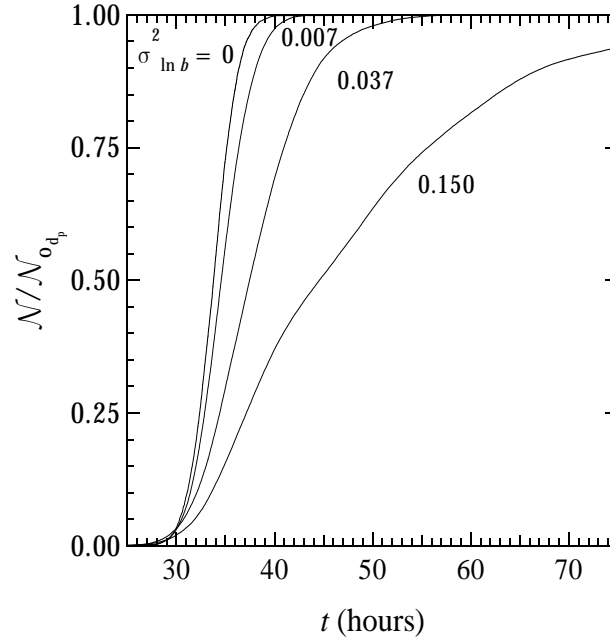


Figure 7.7: Normalized cumulative colloid breakthrough curves for a polydisperse colloid plume in variable aperture fractures with four different $\sigma_{\ln b}^2$ values (here $\bar{b} = 1 \times 10^{-4}$ m, $\sigma_{d_p} = 0.9 \mu\text{m}$, $\mu_{d_p} = 1 \mu\text{m}$, $\xi_b = 1$ m).

earliest colloid breakthrough corresponds to the plume with largest σ_{d_p} . As illustrated in Figure 7.5b, colloid separation within a plume is based on particle diameter with the larger colloids traveling faster than the smaller colloids. Although large particles tend to remain in high velocity streamlines near the center of the fracture longer than small particles because of fluid–particle phases stresses, drag, lift, and Faxen forces [McTigue *et al.*, 1986], none of these effects are considered in this analysis. Regardless, the largest particles travel at a velocity somewhat higher than the mean fluid velocity.

The effect of the variance of the log–transformed aperture on the transport of polydisperse colloids in fractures with spatially variable aperture is shown in Figure 7.7. Four different $\sigma_{\ln b}^2$ values are examined: 0.0 (uniform aperture), 0.007, 0.037, and 0.125. Comparison of the normalized cumulative colloid breakthrough curves indicate that increasing $\sigma_{\ln b}^2$ increases the tailing of the colloid plume. It is well established in the literature that increasing the heterogeneity of any flow or transport parameter leads to increased spreading [e.g., Dagan, 1982; Chrysikopoulos, 1995].

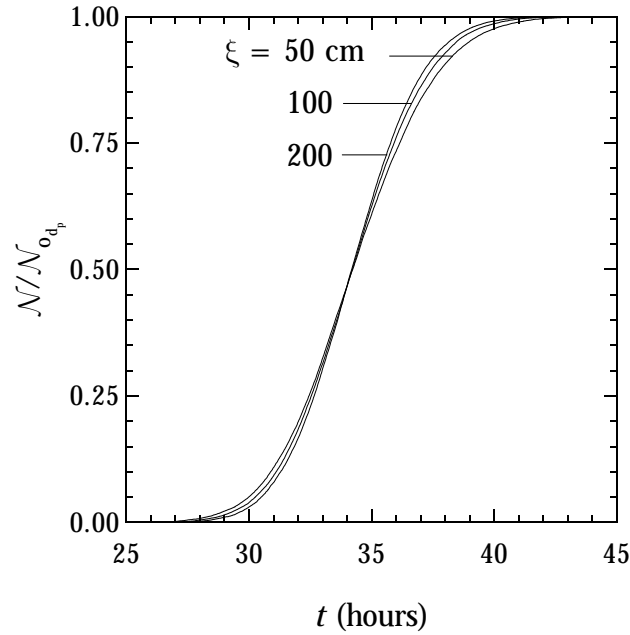


Figure 7.8: Normalized cumulative colloid breakthrough curves for a polydisperse colloid plume in variable aperture fractures with three different correlation lengths of the aperture fluctuations (here $\bar{b} = 1 \times 10^{-4}$ m, $\sigma_{\ln b}^2 = 0.037$, $\mu_{d_p} = 1 \mu\text{m}$, $\sigma_{d_p} = 0.9 \mu\text{m}$).

Further, *Rehmann et al.* [1999] have suggested that premature breakthrough of viruses (colloids) in high variance conductivity fields of porous media is a result of the increase in preferential flow paths. A similar phenomenon occurs here where large aperture portions of the fracture allow early colloid breakthrough while the many small aperture areas increase tailing by slowing many of the colloids. Because solution to the cubic equation overestimates the flow rates in low aperture areas of the fracture [*Brown et al.*, 1995], experimental results of colloid transport in a variable aperture fracture may exhibit even greater tailing than shown here. Some experimental work has been done studying colloid transport in a fracture, but selection of investigational parameters and measurement quantities complicate comparison with this work. *Bales et al.* [1989] showed early breakthrough and decreased spread of colloids when compared to solutes. Although no simulations were performed in this work with particles diffusing into the solid matrix, it was shown in Chapter 6 that matrix diffusion leads to increased retardation and increased tailing [*James and Chrysikopoulos*, 1999].

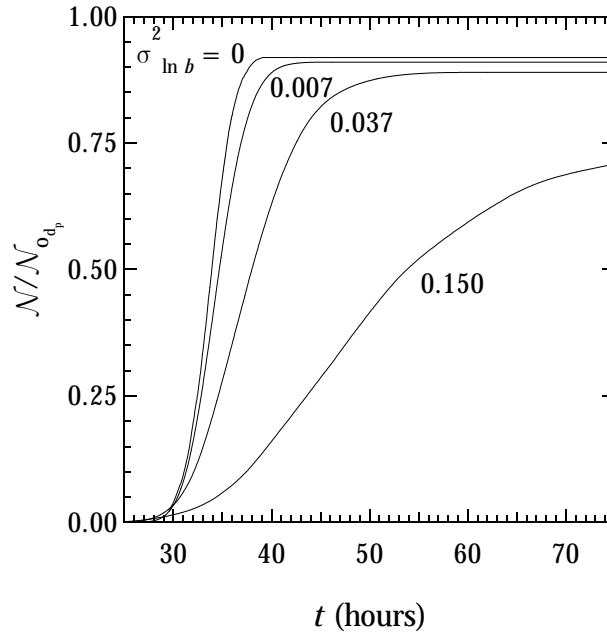


Figure 7.9: Normalized cumulative colloid breakthrough curves for an irreversibly sorbing polydisperse colloid plume in variable aperture fractures with four different $\sigma_{\ln b}^2$ values (here $\bar{b} = 1 \times 10^{-4}$ m, $\sigma_{d_p} = 0.6 \mu\text{m}$, $\mu_{d_p} = 1 \mu\text{m}$, $\xi_b = 1$ m, $\phi = 10kT$, $\nu = 15$).

The effect of the correlation length of aperture fluctuations on polydisperse colloid transport in a fracture with variable aperture is illustrated in Figure 7.8. The simulated normalized cumulative colloid breakthrough curves indicate that colloid spreading increases with increasing ξ_b because larger ξ_b implies a more heterogeneous field ($\xi_b = \infty$ is a random, uncorrelated field). Consequently, the longitudinal dispersivity of a fracture with spatially variable aperture is dependent on both ξ_b and $\sigma_{\ln b}^2$. This is analogous to the increase in dispersivity for a heterogeneous porous medium caused by an increase in the variance and correlation length of the hydraulic conductivity [Gelhar and Axness, 1983].

Figure 7.9 illustrates the effect of sorption on polydisperse colloid transport in variable aperture fractures. Sorption causes reduction in the number of colloids suspended in the liquid phase prohibiting the normalized cumulative colloid breakthrough curves from reaching the maximum value of one. These results are in agreement with previous investigations by Abdel-Salam and

Chrysikopoulos [1994]; however, it is worthwhile noting that increases in $\sigma_{\ln b}^2$ lead to elongated tailing of the colloid plume as well as enhanced colloid deposition. This result is attributable to the fact that for log-normally distributed apertures, a long tail toward larger apertures exists with the majority of aperture elements smaller than the mean. When $\sigma_{\ln b}^2$ increases, the range of apertures increases as does the number of small aperture elements. With an increased number of small aperture elements, more particle-wall collisions are expected leading to increased colloid sorption. Furthermore, it is clear from Figure 7.5d that, on average, it is the largest particles that travel fastest through the fracture and the smallest ones that are being deposited. Furthermore, small particles have higher molecular diffusion coefficients than large particles, thus small particles encounter the wall more frequently resulting in increased attachment.

7.7 Summary

The transport of polydisperse colloid plumes in a water saturated fracture with spatially variable aperture was modeled with the new particle tracking technique. Results from model simulations show that polydisperse colloid suspensions exhibit different transport characteristics than monodisperse suspensions. The observed spreading of colloid plumes can be attributed to variability in both fracture aperture fluctuations as well as colloid diameters. Small colloids tend to travel at velocities closer to the mean flow velocity while larger colloids travel faster, effectively increasing the spreading of the plume. Increasing the variability and/or the correlation length of the fracture aperture fluctuations results in more spreading of the colloids. When surface sorption is accounted for, it is the smallest colloids of a plume that preferentially sorb.

Chapter 8

Application and Engineering

Significance of Results

Chapter 3 presents a complete derivation of effective transport parameters for colloids traveling in a water saturated, uniform aperture, fracture. The finite size of constituents of a colloid plume impacts how it travels through fractured media resulting in increased effective velocity and decreased effective dispersion of the plume. As many transport models assume colloids and contaminants to be infinitely small, neglecting the effects of colloidal size on transport parameters may result in erroneous model output.

The analytical solutions presented in Chapter 4 for colloid transport in a uniform aperture fracture with and without sorption onto the rock matrix, provide a useful tool for determining the spatial and temporal distribution of colloidal particles in fractured systems. Although the analytical solutions are highly idealized, they can be used for preliminary examinations of colloid transport and for verification of numerical models for more complex systems.

The particle tracking algorithm developed in Chapter 5 provides an new and efficient numerical solution to what might otherwise be a computationally costly simulation. As opposed to

the traditional particle tracking equation where a constant time step is specified, in the new particle tracking equation a variable time step is determined from a pre-specified constant spatial step. Although this algorithm may not be applicable in all cases (i.e., when matrix diffusion or perfect sink sorption is included), it is an efficient method for determining breakthrough curves for polydisperse colloid transport in fractured media.

The particle tracking model developed in Chapter 6 is a good tool for studying colloid transport in fractures that are not subject to high overburden pressures (where fracture aperture variability is minimal). Colloids are allowed to diffuse into the surrounding rock matrix or to attach irreversibly and reversibly onto the fracture walls. The fact that the colloid plume comprises constituents of variable size (polydisperse) is enough to significantly affect transport parameters. It is shown that the largest particles are transported fastest and furthest while the small particles preferentially diffuse into or sorb onto the fracture walls. This could have serious implications on the disposal of hazardous material in fractured media, and on the design of waste repositories.

In most natural fractures, fracture aperture variability is important to consider. The model developed in Chapter 7 (an extension to the model used in Chapter 6) for colloid transport is used to examine colloid transport in a quasi-three-dimensional variable aperture fracture. Results indicate that variability in both the fracture aperture fluctuations as well as size of the constituents is enough to affect transport parameters. The model shows that when colloids are subject to flow channelization spreading through the system is enhanced. Again, variability in either polydispersity or fracture aperture fluctuations is enough to increase the spreading of a colloid plume. Large particles are transported fastest while the smallest particles are preferentially sorbed onto fracture walls. Again this could have significant effects on hazardous waste disposal practices, especially if contaminant co-transport is considered. The numerical models used in this research are robust and versatile. They are designed to be extendable to larger more general models of colloid and contaminant transport in both saturated and unsaturated fractured media.

Chapter 9

Summary, Conclusions and Future Research

9.1 Summary

The modeling work presented in this study investigates the saturated transport of colloids in fractured subsurface formations. Preliminarily, the finite size, or size exclusion effect, of colloids is considered. Colloids are proven to have higher effective velocities and lower effective dispersion rates than soluble contaminants. Because naturally occurring colloids are not infinitely small and not of a single, uniform size, the effects of polydispersity on the transport properties of a colloid plume are important to investigate. Several analytical models for polydisperse colloid transport in a single fracture idealized as two parallel plates and surrounded by an impenetrable host rock matrix were presented and solved. The analytical solutions were derived under both instantaneous and constant concentration injection inlet boundary conditions and for cases of irreversible or reversible deposition onto the fracture surfaces.

Because mathematical models require many simplifying assumptions to obtain closed form analytical solutions, they often do not reliably model the physical transport properties of natural colloids in subsurface fractured formations. In an effort to model more generalized systems a novel particle tracking algorithm is developed. Both the traditional and the new particle tracking equations calibrate well with previously derived analytical solutions. Furthermore, the new particle tracking algorithm shows a significant improvement in computational cost over the traditional particle tracking algorithm.

In an effort to model more complicated systems, the particle tracking algorithm is extended to incorporate the effects of polydispersity, matrix diffusion, and surface sorption. Simulation results show that matrix diffusion and surface sorption serve to retard the breakthrough of a colloid plume. Variation in the size of plume constituents leads to increased plume spreading as well as early plume breakthrough. The smallest colloids of a polydisperse plume transport slowest, preferentially diffuse into the surrounding matrix, and preferentially sorb onto the fracture surfaces. Polydispersity proves to be an important factor to consider when examining the transport of colloid sized particles.

Because natural rock fractures have a range or distribution of apertures, colloid transport was studied within the framework of a variable aperture fracture–rock matrix system. The variable aperture nature of the fracture renders flow and transport quasi–three–dimensional. The fracture aperture is considered a stochastic variable described by a spatially correlated log–normal probability density function. The new particle tracking algorithm is employed to simulate colloid transport in single realizations of a variable aperture fracture. Ensemble averages of breakthrough curves are used to analyze polydisperse colloid transport properties. Kinetic sorption of colloid onto the fracture surfaces is incorporated into the model with results indicating that both the fracture aperture variability and colloid polydispersity are important transport parameters.

9.2 Conclusions

The finite size of the constituents of a colloid plume increase its effective flow velocity and decrease its effective dispersion in a water saturated, parallel plate fracture. Also, analytical solutions for the transport of polydisperse colloid plumes in a uniform fracture subject to varied boundary conditions show that polydispersity alone is a significant factor affecting plume transport. Furthermore, small colloids travel slowest and preferentially sorb onto fracture walls.

A novel particle tracking algorithm with a specified spatial step and a random time step is derived and proves to be an efficient and accurate solution method when compared to analytical and traditional particle tracking solutions.

Generalizing both new and traditional particle tracking schemes to include penetration of polydisperse colloids into the fracture matrix and to incorporate both perfect sink (irreversible) and kinetic (reversible) reaction at the fracture walls yielded significant results. The colloid transport model of a single parallel plate fracture was found to be sensitive to polydispersity of the colloid plume. Large colloids travel fastest and furthest along uniform aperture fractures. Small particles preferentially diffuse into the fracture matrix. Furthermore, smaller particles show increased attachment rates under both perfect sink and kinetic sorption conditions. Increasing the aperture of the uniform fracture serves to reduce overall colloid deposition.

When the new particle tracking algorithm is extended to model a variable aperture fracture, several important results are realized. Both fracture aperture variability and colloid polydispersity are important parameters, increasing either serves to increase the dispersion of the plume throughout the system. Again, small colloid travel slowest and preferentially sorb onto fracture surfaces. This sorption rate increases for fractures with a higher variability in aperture.

9.3 Recommendations for Future Research

Although this work addressed many issues related to polydisperse colloid transport in saturated fractured media, other facets of flow, colloid, and colloid-facilitated contaminant transport in fractured media require further investigation. The most important of these are:

- Effective transport parameters for finitely sized particle are derived under the assumption that the colloids are hard spherical particles. Naturally occurring colloids may be aspherical and have significant surface charge. Incorporation of these colloid characteristics as well as wall effects will further generalize the results.
- Although the analytical models presented in Chapter 4 have several advantages, some of the inherent limitations are their inability: (a) to allow for colloid deposition rates as a function of colloid surface coverage; (b) to account for variability in the aperture that is present in real rock fractures; and (c) to account for gravitational forces. Nonetheless, these models can provide means for verifying the accuracy of numerical solutions to more comprehensive models for colloid transport in fractured subsurface formations.
- It may be possible to extend the new particle tracking scheme from a diffusive equation to one that incorporates a drift velocity, thereby further generalizing the algorithm.
- Some of the limitations inherent to the models for colloid transport presented in Chapters 6 and 7 are their inability to account for (a) gravitational effects; and (b) particle entrapment (clogging) between the fracture surfaces. Nonetheless, these models provide a starting point for generalization of the solution to more complicated physical systems.
- The reduction in permeability with deposition of colloids because of a decrease in fracture aperture ultimately leads to a time dependent fracture aperture and consequently an unsteady velocity field. Particle tracking models may be extended to account for such phenomena.

- Colloid and contaminant co-transport may easily be incorporated into any of the particle tracking algorithms. Co-transport has been an area of increasing concern and should be modeled by particle tracking techniques within the context of fractured media.
- The effect of anisotropy on the transport of polydisperse colloids in a variable aperture fracture should be considered.
- Particle tracking techniques should be applied to unsaturated flow and transport of polydisperse colloids in a variable aperture fracture.
- As a further step toward modeling a fracture network, flow and transport in a bifurcating fracture needs to be examined (see Appendices E and F). A particle tracking algorithm may be used to this end.
- The ultimate goals of this research are incorporation of many single fractures into a saturated and unsaturated fracture network with general modeling of reactive polydisperse colloid and contaminant co-transport subject to matrix diffusion and surface sorption.

Appendix A

Governing Equations for Poiseuille Fluid Flow

The Navier–Stokes equations for polyatomic Newtonian fluids are [*Happel and Brenner*, 1965]:

$$\begin{aligned} \rho \frac{\partial \mathbf{u}}{\partial t} + \rho \mathbf{u} \cdot \nabla \mathbf{u} = & -\nabla P + \mu \nabla^2 \mathbf{u} + \frac{1}{3} \mu \nabla (\nabla \cdot \mathbf{u}) + 2 (\nabla \mu) \cdot \nabla \mathbf{u} + (\nabla \mu) \times (\nabla \times \mathbf{u}) \\ & - \frac{2}{3} (\nabla \mu) (\nabla \cdot \mathbf{u}) + \kappa \nabla (\nabla \cdot \mathbf{u}) + (\nabla \kappa) (\nabla \cdot \mathbf{u}) + \rho \mathbf{F}, \end{aligned} \quad (\text{A.1})$$

where κ is the bulk or volume viscosity; μ is the kinematic viscosity; ρ is the fluid density; P is the local fluid pressure; \mathbf{F} are the body forces acting on the fluid (e.g., gravity); and \mathbf{u} is the three-dimensional velocity vector. If the fluid is incompressible (i.e., $\nabla \cdot \mathbf{u} = 0$) then (A.1) reduces to:

$$\rho \frac{\partial \mathbf{u}}{\partial t} + \rho \mathbf{u} \cdot \nabla \mathbf{u} = -\nabla P + \mu \nabla^2 \mathbf{u} + 2 (\nabla \mu) \cdot \nabla \mathbf{u} + (\nabla \mu) \times (\nabla \times \mathbf{u}) + \rho \mathbf{F}. \quad (\text{A.2})$$

If the flow is isothermal (i.e., constant bulk and kinematic viscosities), there is no viscosity gradient and the incompressible Navier–Stokes equations (A.2) may be reduced to:

$$\rho \frac{\partial \mathbf{u}}{\partial t} + \rho \mathbf{u} \cdot \nabla \mathbf{u} = -\nabla P + \mu \nabla^2 \mathbf{u} + \rho \mathbf{F}. \quad (\text{A.3})$$

Assuming that the only body force acting on the fluid is gravity, $\mathbf{F} = -gz$, the pressure and gravitational body forces may be combined into a reduced pressure

$$\mathcal{P} = P + \rho gz. \quad (\text{A.4})$$

Fracture flow is generally defined under the assumption of a steady-state, uniform pressure gradient implying that

$$\frac{\partial \mathbf{u}}{\partial t} = 0. \quad (\text{A.5})$$

Substitution (A.4) and (A.5) into (A.2) yields a simplified form of the Navier–Stokes equations:

$$\mu \nabla^2 \mathbf{u} - \rho (\mathbf{u} \cdot \nabla) \mathbf{u} = \nabla \mathcal{P}. \quad (\text{A.6})$$

The presence of the advective component of acceleration, $(\mathbf{u} \cdot \nabla) \mathbf{u}$, causes the equation to be nonlinear and not always amenable to analytical solution. In general, if the flow is very slow (i.e., $Re < 1$), the advective term may be considered negligible, affording an approximate solution. For the case of steady flow between parallel plates, the advective term vanishes identically because there is no flow in the y - or z -directions and the gradient of flow is normal to the z -direction (see Appendix B).

The final reduced form of the Navier–Stokes equations becomes

$$\mu \nabla^2 \mathbf{u} = \nabla \mathcal{P}. \quad (\text{A.7})$$

Appendix B

Derivation of the Parabolic Velocity Profile

The derivation of the parabolic velocity profile for laminar flow between parallel plates begins by assuming that there is a uniform pressure gradient within the plane of the fracture. The average pressure gradient, $\overline{\nabla P}$, is given as $(P_o - P_i)/L$ where P_o and P_i are the pressures at the outlet and inlet of the fracture, respectively, and L is the length of the fracture. The Cartesian coordinate system is defined so that x is parallel to ∇P , z is perpendicular to the fracture walls, and y is perpendicular to x in the plane of the fracture. The top and bottom walls of the fracture correspond to $z = \pm b/2$.

The pressure gradient lies entirely in the plane of the fracture and has no z component. If gravitational effects are considered, no change on the overall solution method will be affected as P may be defined as $p + \rho gz$. The velocity field has no component in the z -direction, necessitated by the no flow conditions at the boundary, $z = \pm b/2$. Because the geometry of the system is constant in x and y , the pressure gradient is uniform in the fracture. As such, the velocity vector can only be a function z . Consequently, the advective component of the Navier–Stokes equation, $(\mathbf{u} \cdot \nabla)\mathbf{u}$ can

be expressed as:

$$(\mathbf{u} \cdot \nabla) \mathbf{u} = (\mathbf{u} \cdot \nabla) (u_x, u_y, u_z) = [\mathbf{u} \cdot (\nabla u_x), \mathbf{u} \cdot (\nabla u_y), \mathbf{u} \cdot (\nabla u_z)] \quad (\text{B.1})$$

Because there are no velocity components in the y - and z -directions, and the velocity itself has only an x component, the dot products above are $\mathbf{0}$. This removes the nonlinearity from the Navier–Stokes equation (A.6) and reduces it to:

$$\mu \nabla^2 \mathbf{u}(z) = \nabla P. \quad (\text{B.2})$$

∇P has already been defined as:

$$\nabla P = \left(\frac{\partial P}{\partial x}, \frac{\partial P}{\partial y}, \frac{\partial P}{\partial z} \right) = (\overline{\nabla P}, 0, 0) \quad (\text{B.3})$$

Equating (B.2) and (B.3) indicates that the velocity components must satisfy:

$$\nabla^2 u_x(z) = \frac{\nabla P}{\mu}, \quad \nabla^2 u_y(z) = 0, \quad \nabla^2 u_z(z) = 0 \quad (\text{B.4})$$

The no slip boundary condition requires that $\mathbf{u} = 0$ when $z = \pm b/2$. Using these boundary conditions and integrating the preceding equations twice yields:

$$u_x(z) = \frac{\overline{\nabla P} b^2}{2\mu} \left[4 \left(\frac{z}{b} \right)^2 - 1 \right], \quad u_y(z) = 0, \quad u_z(z) = 0 \quad (\text{B.5})$$

If the velocity along the centerline of the system ($z = 0$) is called U_{\max} , then U_{\max} can be defined as $-\overline{\nabla P} b^2 / 2\mu$. Finally, this reduces to the standard Poiseuille equation:

$$u_x(z) = U_{\max} \left[1 - 4 \left(\frac{z}{b} \right)^2 \right]. \quad (\text{B.6})$$

Appendix C

Effective Parameters for Irreversible Sorption

Consider two-dimensional, unsteady, advection and diffusion of reactive particles within a uniform aperture fracture. The governing equation for polydisperse particle transport is given by:

$$\frac{\partial n_{d_p}(x, z, t)}{\partial t} = \mathcal{D}_{d_p} \left[\frac{\partial^2 n_{d_p}(x, z, t)}{\partial x^2} + \frac{\partial^2 n_{d_p}(x, z, t)}{\partial z^2} \right] - u_x(z) \frac{\partial n_{d_p}(x, z, t)}{\partial x}, \quad (\text{C.1})$$

where n_{d_p} is the temporally and spatially varying number density (concentration) of polydisperse particles with diameter d_p ; \mathcal{D}_{d_p} is the molecular diffusion coefficient; $u_x(z)$ is the flow profile within the fracture; x is the coordinate in the axial or flow direction; z is the coordinate perpendicular to the fracture wall; and t is time. Fully developed Poiseuille flow is assumed to exist within the semi-infinite, uniform aperture fracture created by the no-slip boundary conditions. Furthermore, it is assumed that the fluid density and dynamic viscosity are constant and that gravitational effects as well as particle-particle interactions are negligible.

One boundary condition imposed on the system is that the particles are neutrally buoyant, thereby eliminating the flux of particles across the fracture centerline,

$$\frac{\partial n_{d_p}(x, 0, t)}{\partial z} = 0. \quad (\text{C.2})$$

A second boundary condition states that there is a flux of particles at the fracture walls due to attachment expressed as

$$\mathcal{D}_{d_p} \frac{\partial n_{d_p}(x, \pm b/2, t)}{\partial z} = -k_f n_{d_p}(x, \pm b/2, t). \quad (\text{C.3})$$

The transverse average colloid concentration is defined by integrating the particle concentration across the fracture aperture and dividing by the aperture as follows

$$\bar{n}_{d_p}(x, t) = \frac{1}{b} \int_{-\frac{b}{2}}^{\frac{b}{2}} n_{d_p}(x, z, t) dz. \quad (\text{C.4})$$

Upon averaging equation (C.1) across the fracture and substituting the boundary condition (C.3) into the result, the governing transport equation becomes

$$\frac{\partial \bar{n}_{d_p}(x, t)}{\partial t} = \mathcal{D}_{d_p} \frac{\partial^2 \bar{n}_{d_p}(x, t)}{\partial x^2} - \int_{-\frac{b}{2}}^{\frac{b}{2}} u_x(z) \frac{\partial n_{d_p}(x, z, t)}{\partial x} dz - k_f \bar{n}_{d_p}(x, t). \quad (\text{C.5})$$

In constructing a dispersion approximation to equation (C.1), the primary goal is to transform the preceding equation into a form resembling

$$\frac{\partial \bar{n}_{d_p}(x, t)}{\partial t} = D_{\text{eff}} \frac{\partial^2 \bar{n}_{d_p}(x, t)}{\partial x^2} - U_{\text{eff}} \frac{\partial \bar{n}_{d_p}(x, t)}{\partial x} + K_{\text{eff}} \bar{n}_{d_p}(x, t), \quad (\text{C.6})$$

and in the process to identify the effective dispersion, advection, and reaction coefficients D_{eff} , U_{eff} , and K_{eff} , respectively.

For systems where transverse variation of colloid concentration is slight, the following approximation to the governing equation (C.1) may be entertained

$$\frac{\partial^2 n_{d_p}(x, z, t)}{\partial z^2} = \frac{1}{\mathcal{D}_{d_p}} \left[\frac{\partial \bar{n}_{d_p}(x, t)}{\partial t} - \mathcal{D}_{d_p} \frac{\partial^2 \bar{n}_{d_p}(x, t)}{\partial x^2} \right] + \frac{U_{\text{max}}}{\mathcal{D}_{d_p}} \left[1 - 4 \left(\frac{z}{b} \right)^2 \right] \frac{\partial \bar{n}_{d_p}(x, t)}{\partial x}, \quad (\text{C.7})$$

where $u_x(z)$ was replaced by the expression for the parabolic Poiseuille velocity profile. Integrating both sides of (C.7) with respect to z and assuming that all derivative terms are very nearly constant

with respect to z yields

$$\frac{\partial n_{d_p}(x, z, t)}{\partial z} = \frac{z}{\mathcal{D}_{d_p}} \left[\frac{\partial \bar{n}_{d_p}(x, t)}{\partial t} - \mathcal{D}_{d_p} \frac{\partial^2 \bar{n}_{d_p}(x, t)}{\partial x^2} \right] + \frac{U_{\max} b}{\mathcal{D}_{d_p}} \left[\frac{z}{b} - \frac{4}{3} \left(\frac{z}{b} \right)^3 \right] \frac{\partial \bar{n}_{d_p}(x, t)}{\partial x} + C, \quad (\text{C.8})$$

where C is an integration constant. Upon application of the non-dispersive flux boundary condition (C.2) across the centerline due to neutral particle buoyancy, the integration constant is eliminated.

A second integration of (C.7) yields

$$\begin{aligned} n_{d_p}(x, z, t) &= \frac{z^2}{2\mathcal{D}_{d_p}} \left[\frac{\partial \bar{n}_{d_p}(x, t)}{\partial t} - \mathcal{D}_{d_p} \frac{\partial^2 \bar{n}_{d_p}(x, t)}{\partial x^2} \right] \\ &\quad + \frac{U_{\max} b^2}{2\mathcal{D}_{d_p}} \left[\left(\frac{z}{b} \right)^2 - \frac{2}{3} \left(\frac{z}{b} \right)^4 \right] \frac{\partial \bar{n}_{d_p}(x, t)}{\partial x} + n_{\text{cl}}(x, t), \end{aligned} \quad (\text{C.9})$$

where $n_{\text{cl}}(x, t)$ is an integration constant representing the concentration at the centerline of the fracture.

Averaging the colloid concentration in (C.9) across the fracture aperture yields

$$\bar{n}_{d_p}(x, t) = \frac{b^2}{24\mathcal{D}_{d_p}} \left[\frac{\partial \bar{n}_{d_p}(x, t)}{\partial t} - \mathcal{D}_{d_p} \frac{\partial^2 \bar{n}_{d_p}(x, t)}{\partial x^2} \right] + \frac{3U_{\max} b^2}{80\mathcal{D}_{d_p}} \frac{\partial \bar{n}_{d_p}(x, t)}{\partial x} + n_{\text{cl}}(x, t). \quad (\text{C.10})$$

Rearranging (C.9) to solve for $n_{\text{cl}}(x, t)$ and substituting the result into (C.10) allows $n_{d_p}(x, t)$ to be expressed in terms of the average concentration across the fracture rather than the concentration at the centerline:

$$\begin{aligned} n_{d_p}(x, z, t) &= \frac{b^2}{2\mathcal{D}_{d_p}} \left[\left(\frac{z}{b} \right)^2 - \frac{1}{12} \right] \left[\frac{\partial \bar{n}_{d_p}(x, t)}{\partial t} - \mathcal{D}_{d_p} \frac{\partial^2 \bar{n}_{d_p}(x, t)}{\partial x^2} \right] \\ &\quad + \frac{U_{\max} b^2}{2\mathcal{D}_{d_p}} \left[\left(\frac{z}{b} \right)^2 - \frac{2}{3} \left(\frac{z}{b} \right)^4 - \frac{3}{40} \right] \frac{\partial \bar{n}_{d_p}(x, t)}{\partial x} + \bar{n}_{d_p}(x, t), \end{aligned} \quad (\text{C.11})$$

Substituting (C.11) into the boundary condition (C.3) and evaluating the entire expression at the fracture wall, $z = b/2$, results in a modified differential equation for average colloid concentration given by

$$\frac{\partial \bar{n}_{d_p}(x, t)}{\partial t} - \mathcal{D}_{d_p} \frac{\partial^2 \bar{n}_{d_p}(x, t)}{\partial x^2} = -U_{\max} \frac{4 + \frac{4}{5} Da}{6 + Da} \frac{\partial \bar{n}_{d_p}(x, t)}{\partial x} - \frac{12k_f}{b(6 + Da)} \bar{n}_{d_p}(x, t), \quad (\text{C.12})$$

where the Damköhler number, a dimensionless measure of the tendency for reaction versus the tendency for diffusive transport that is a function of particle size through \mathcal{D}_{d_p} , is defined as

$$Da = \frac{k_f b}{\mathcal{D}_{d_p}}. \quad (\text{C.13})$$

Note that for $k_f = 0$ the one-dimensional advection diffusion equation for average colloid concentration results

$$\frac{\partial \bar{n}_{d_p}(x, t)}{\partial t} = \mathcal{D}_{d_p} \frac{\partial^2 \bar{n}_{d_p}(x, t)}{\partial z^2} - \frac{2}{3} U_{\max} \frac{\partial \bar{n}_{d_p}(x, t)}{\partial x}. \quad (\text{C.14})$$

Eliminating $\partial \bar{n}_{d_p}(x, t) / \partial t - \mathcal{D}_{d_p} \partial^2 \bar{n}_{d_p}(x, t) / \partial z^2$ by equating the equations (C.11) and (C.12) yields the following expression for the colloid concentration

$$\begin{aligned} n_{d_p}(x, z, t) = & \left\{ 1 - \frac{6Da}{6 + Da} \left[\left(\frac{z}{b} \right)^2 - \frac{1}{12} \right] \right\} \bar{n}_{d_p}(x, t) \\ & + \left\{ \left(\frac{z}{b} \right)^2 - \frac{2}{3} \left(\frac{z}{b} \right)^4 - \frac{3}{40} - \frac{4 + \frac{4}{5}Da}{6 + Da} \left[\left(\frac{z}{b} \right)^2 - \frac{1}{12} \right] \right\} \frac{U_{\max} b^2}{2\mathcal{D}_{d_p}} \frac{\partial \bar{n}_{d_p}(x, t)}{\partial x}. \end{aligned} \quad (\text{C.15})$$

The preceding equation can be used to approximate all of the effective parameters in equation (C.6). In particular, using equation (C.15) to evaluate terms $-\int_{-b/2}^{b/2} u_x(z) [\partial n_{d_p}(x, z, t) / \partial x] dz - k_f n_{d_p}(x, \pm b/2, t)$ in (C.5) (ignoring higher order derivative terms) yields the following one-dimensional advection-diffusion equation with decay

$$\begin{aligned} \frac{\partial \bar{n}_{d_p}(x, t)}{\partial t} = & \left[\mathcal{D}_{d_p} + \frac{2}{945} \frac{U_{\max}^2 b^2}{\mathcal{D}_{d_p}} \left(1 - \frac{7}{10} \frac{Da}{6 + Da} \right) \right] \frac{\partial^2 \bar{n}_{d_p}(x, t)}{\partial x^2} \\ & - \frac{2}{3} U_{\max} \left(1 + \frac{3}{10} \frac{Da}{6 + Da} \right) \frac{\partial \bar{n}_{d_p}(x, t)}{\partial x} - \frac{12\mathcal{D}_{d_p}}{b^2} \frac{Da}{6 + Da} \bar{n}_{d_p}(x, t). \end{aligned} \quad (\text{C.16})$$

From the preceding equation the appropriate effective parameters are specified:

$$D_{\text{eff}} = \mathcal{D}_{d_p} + \frac{2}{945} \frac{U_{\max}^2 b^2}{\mathcal{D}_{d_p}} \left(1 - \frac{7}{10} \frac{Da}{6 + Da} \right), \quad (\text{C.17})$$

$$U_{\text{eff}} = \frac{2}{3} U_{\max} \left(1 + \frac{3}{10} \frac{Da}{6 + Da} \right), \quad (\text{C.18})$$

$$K_{\text{eff}} = \frac{12\mathcal{D}_{d_p}}{b^2} \frac{Da}{6 + Da}. \quad (\text{C.19})$$

Appendix D

Derivation of the Harmonic Mean

The harmonic mean equation is an exact expression for the equivalent hydraulic aperture corresponding to the pressure drop and flow between adjacent fracture aperture elements. Consider two elements of equal size $\Delta x \times \Delta y$ with aperture $b_{i,j}$ and $b_{i,j+1}$, respectively. Employing the Bousinesque or ‘cubic law’ equation to approximate the flow between these elements as linear flow between ‘equivalent’ parallel plates, the flow in the x -direction may be expressed as:

$$q = -\frac{\Delta P}{12\mu\Delta x} b_{\text{eq}}^3 \Delta y, \quad (\text{D.1})$$

where μ is the kinematic viscosity; $\Delta P = P_{i,j+1} - P_{i,j}$ is the pressure drop between adjacent element centers; and b_{eq} is the equivalent aperture. Conservation of mass states that the flow out of element i, j in the x -direction is equal to flow into adjacent element $i, j+1$. Applying the cubic law equation to element i, j produces:

$$q_{i,j} = -\frac{P_B - P_{i,j}}{12\mu\frac{\Delta x}{2}} b_{i,j}^3 \Delta y, \quad (\text{D.2})$$

where P_B is the pressure at the boundary of the adjacent elements. For element $i, j+1$, the flow is:

$$q_{i,j+1} = -\frac{P_{i,j+1} - P_B}{12\mu\frac{\Delta x}{2}} b_{i,j+1}^3 \Delta y, \quad (\text{D.3})$$

Conservation of mass requires that (D.2) and (D.3) be equal. Solving for P_B yields:

$$P_B = \frac{P_{i,j}b_{i,j}^3 + P_{i,j+1}b_{i,j+1}^3}{b_{i,j}^3 + b_{i,j+1}^3}. \quad (\text{D.4})$$

Substituting (D.4) into (D.2) yields an expression for the flow rate between cells

$$q_{i,j} = -\frac{\frac{P_{i,j}b_{i,j}^3 + P_{i,j+1}b_{i,j+1}^3}{b_{i,j}^3 + b_{i,j+1}^3} - P_{i,j}}{12\mu\frac{\Delta x}{2}}b_{i,j}^3\Delta y. \quad (\text{D.5})$$

Equation (D.5) may be simplified to

$$q_{i,j} = -\frac{P_{i,j+1} - P_{i,j}}{12\mu\Delta x} \frac{2b_{i,j}^3 b_{i,j+1}^3}{b_{i,j}^3 + b_{i,j+1}^3} \Delta y. \quad (\text{D.6})$$

Equation (D.6) is identical in form to (D.1) with the equivalent hydraulic aperture given by:

$$b_{\text{eq}} = \left(\frac{2b_{i,j}^3 b_{i,j+1}^3}{b_{i,j}^3 + b_{i,j+1}^3} \right)^{\frac{1}{3}}. \quad (\text{D.7})$$

Appendix E

Conformal Mapping

As most practical problems of interest have solutions over irregular domains, generation of a boundary-fitted coordinate system for the purpose of modeling systems with curved boundaries is an essential part of many finite difference numerical problems. In most partial differential systems the boundary conditions exert the dominant influence on the character of the solution, and the use of grid points not coincident with the boundaries places the most inaccurate difference representation in precisely the region of greatest sensitivity. The generation of a curvilinear coordinate system with coordinate lines coincident with all boundaries is a critical part of a general numerical solution of an irregularly shaped partial differential system.

The method of generating boundary-fitted coordinate systems begins by assuming that the curvilinear coordinates in (ξ, η) are solutions of an elliptic partial differential system in the physical plane with Dirichlet (constant value) boundary conditions on all boundaries. That is, ξ and η are specified as functions of x and y on all boundaries. This so-called conformal mapping transforms the irregularly shaped (x, y) domain into a rectangular (ξ, η) domain where gridlines are assigned according to the solution of the elliptical differential equations presented below. Control of the spacing of the coordinate lines on the original (x, y) domain is easily accomplished because these points are specified a priori. Typically these points are clustered (have higher density) near region

where large gradients in the solution are expected. In the case of bifurcating flow, the grid points should be grouped near the bifurcation itself.

The spacing of the coordinate lines in the transformed field may be controlled by varying the elliptic generating system for the coordinates. One method for controlling the (ξ, η) grid spacing is to add inhomogeneous terms, $P(\xi, \eta)$ and $Q(\xi, \eta)$, transforming the Laplace equations into Poisson equations, so that the generating system becomes,

$$\nabla^2 \xi = P(\xi, \eta), \quad (\text{E.1})$$

$$\nabla^2 \eta = Q(\xi, \eta). \quad (\text{E.2})$$

The numerical solutions of (E.1) and (E.2) map the coordinates (x, y) onto the gridpoints (ξ, η) . However, $\xi = \xi(x, y)$ and $\eta = \eta(x, y)$ are known while $x = x(\xi, \eta)$ and $y = y(\xi, \eta)$ are not. Because both coordinate systems are monotonically increasing, the Laplace equations (E.1) and (E.2) are invertible and can be transformed by the chain rule. Any function $f(x, y)$ may be represented as a function of ξ and η as follows

$$f(x, y) = f(x(\xi, \eta), y(\xi, \eta)) = f(\xi, \eta). \quad (\text{E.3})$$

The chain rule applied to $f(\xi, \eta)$ yields first derivative terms of

$$\frac{\partial f}{\partial \xi} = \frac{\partial f}{\partial x} \frac{\partial x}{\partial \xi} + \frac{\partial f}{\partial y} \frac{\partial y}{\partial \xi}, \quad (\text{E.4})$$

$$\frac{\partial f}{\partial \eta} = \frac{\partial f}{\partial x} \frac{\partial x}{\partial \eta} + \frac{\partial f}{\partial y} \frac{\partial y}{\partial \eta}. \quad (\text{E.5})$$

Solving these equations for $\partial f / \partial x$ and $\partial f / \partial y$ yields

$$\frac{\partial f}{\partial x} = \frac{1}{J} \left(\frac{\partial f}{\partial \xi} \frac{\partial y}{\partial \eta} - \frac{\partial f}{\partial \eta} \frac{\partial y}{\partial \xi} \right), \quad (\text{E.6})$$

$$\frac{\partial f}{\partial y} = \frac{1}{J} \left(\frac{\partial f}{\partial \eta} \frac{\partial x}{\partial \xi} - \frac{\partial f}{\partial \xi} \frac{\partial x}{\partial \eta} \right), \quad (\text{E.7})$$

where the quantity J is the Jacobian transformation given by

$$J = \frac{\partial x}{\partial \xi} \frac{\partial y}{\partial \eta} - \frac{\partial x}{\partial \eta} \frac{\partial y}{\partial \xi}. \quad (\text{E.8})$$

Similarly, the second derivatives of $f(x, y)$ are

$$\begin{aligned}
\frac{\partial^2 f}{\partial x^2} &= \frac{1}{J^2} \left[\left(\frac{\partial y}{\partial \eta} \right)^2 \frac{\partial^2 f}{\partial \xi^2} - 2 \frac{\partial y}{\partial \xi} \frac{\partial y}{\partial \eta} \frac{\partial^2 f}{\partial \xi \partial \eta} + \left(\frac{\partial y}{\partial \xi} \right)^2 \frac{\partial^2 f}{\partial \eta^2} \right] \\
&+ \frac{1}{J^3} \left\{ \left[\left(\frac{\partial y}{\partial \eta} \right)^2 \frac{\partial^2 y}{\partial \xi^2} - 2 \frac{\partial y}{\partial \xi} \frac{\partial y}{\partial \eta} \frac{\partial^2 y}{\partial \xi \partial \eta} + \left(\frac{\partial y}{\partial \xi} \right)^2 \frac{\partial^2 y}{\partial \eta^2} \right] \left(\frac{\partial x}{\partial \eta} \frac{\partial f}{\partial \xi} - \frac{\partial x}{\partial \xi} \frac{\partial f}{\partial \eta} \right) \right. \\
&+ \left. \left[\left(\frac{\partial y}{\partial \eta} \right)^2 \frac{\partial^2 x}{\partial \xi^2} - 2 \frac{\partial y}{\partial \xi} \frac{\partial y}{\partial \eta} \frac{\partial^2 x}{\partial \xi \partial \eta} + \left(\frac{\partial y}{\partial \xi} \right)^2 \frac{\partial^2 x}{\partial \eta^2} \right] \left(\frac{\partial y}{\partial \xi} \frac{\partial f}{\partial \eta} - \frac{\partial y}{\partial \eta} \frac{\partial f}{\partial \xi} \right) \right\} \quad (\text{E.9})
\end{aligned}$$

$$\begin{aligned}
\frac{\partial^2 f}{\partial y^2} &= \frac{1}{J^2} \left[\left(\frac{\partial x}{\partial \eta} \right)^2 \frac{\partial^2 f}{\partial \xi^2} - 2 \frac{\partial x}{\partial \xi} \frac{\partial x}{\partial \eta} \frac{\partial^2 f}{\partial \xi \partial \eta} + \left(\frac{\partial x}{\partial \xi} \right)^2 \frac{\partial^2 f}{\partial \eta^2} \right] \\
&+ \frac{1}{J^3} \left\{ \left[\left(\frac{\partial x}{\partial \eta} \right)^2 \frac{\partial^2 y}{\partial \xi^2} - 2 \frac{\partial x}{\partial \xi} \frac{\partial x}{\partial \eta} \frac{\partial^2 y}{\partial \xi \partial \eta} + \left(\frac{\partial x}{\partial \xi} \right)^2 \frac{\partial^2 y}{\partial \eta^2} \right] \left(\frac{\partial x}{\partial \eta} \frac{\partial f}{\partial \xi} - \frac{\partial x}{\partial \xi} \frac{\partial f}{\partial \eta} \right) \right. \\
&+ \left. \left[\left(\frac{\partial x}{\partial \eta} \right)^2 \frac{\partial^2 f}{\partial \xi^2} - 2 \frac{\partial x}{\partial \xi} \frac{\partial x}{\partial \eta} \frac{\partial^2 x}{\partial \xi \partial \eta} + \left(\frac{\partial x}{\partial \xi} \right)^2 \frac{\partial^2 f}{\partial \eta^2} \right] \left(\frac{\partial y}{\partial \xi} \frac{\partial f}{\partial \eta} - \frac{\partial y}{\partial \eta} \frac{\partial f}{\partial \xi} \right) \right\}. \quad (\text{E.10})
\end{aligned}$$

Replacing arbitrary function $f(x, y)$ with $\xi(x, y)$ in (E.9), and with $\eta(x, y)$ in (E.10) allows substitution of the preceding equations into the Laplace equations (E.1) and (E.2). Rearranging yields, in non-conservative form,

$$\alpha \frac{\partial^2 x}{\partial \xi^2} - 2\beta \frac{\partial^2 x}{\partial \xi \partial \eta} + \gamma \frac{\partial^2 x}{\partial \eta^2} + J^2 \left(P \frac{\partial x}{\partial \xi} + Q \frac{\partial x}{\partial \eta} \right) = 0, \quad (\text{E.11})$$

$$\alpha \frac{\partial^2 y}{\partial \xi^2} - 2\beta \frac{\partial^2 y}{\partial \xi \partial \eta} + \gamma \frac{\partial^2 y}{\partial \eta^2} + J^2 \left(P \frac{\partial y}{\partial \xi} + Q \frac{\partial y}{\partial \eta} \right) = 0, \quad (\text{E.12})$$

where

$$\alpha = \left(\frac{\partial x}{\partial \xi} \right)^2 + \left(\frac{\partial y}{\partial \xi} \right)^2, \quad (\text{E.13})$$

$$\beta = \frac{\partial x}{\partial \xi} \frac{\partial x}{\partial \eta} + \frac{\partial y}{\partial \xi} \frac{\partial y}{\partial \eta}, \quad (\text{E.14})$$

$$\gamma = \left(\frac{\partial x}{\partial \eta} \right)^2 + \left(\frac{\partial y}{\partial \eta} \right)^2. \quad (\text{E.15})$$

All derivatives in (E.11) and (E.12) are approximated by the following second-order central finite difference expressions with $\Delta\xi = \Delta\eta$:

$$\begin{aligned}
&\alpha_{i,j} (x_{i+1,j} - 2x_{i,j} + x_{i-1,j}) - \frac{1}{2}\beta_{i,j} (x_{i+1,j+1} - x_{i+1,j-1} - x_{i-1,j+1} + x_{i-1,j-1}) \\
&\quad + \gamma_{i,j} (x_{i,j+1} - 2x_{i,j} + x_{i,j-1}) \\
&\quad + J_{i,j}^2 [(x_{i+1,j} - x_{i-1,j}) P_{i,j} + (x_{i,j+1} - x_{i,j-1}) Q_{i,j}] = 0, \quad (\text{E.16})
\end{aligned}$$

$$\begin{aligned}
& \alpha_{i,j} (y_{i+1,j} - 2y_{i,j} + y_{i-1,j}) - \frac{1}{2}\beta_{i,j} (y_{i+1,j+1} - y_{i+1,j-1} - y_{i-1,j+1} + y_{i-1,j-1}) \\
& \quad + \gamma_{i,j} (y_{i,j+1} - 2y_{i,j} + y_{i,j-1}) \\
& \quad + J_{i,j}^2 [(y_{i+1,j} - y_{i-1,j}) P_{i,j} + (y_{i,j+1} - y_{i,j-1}) Q_{i,j}] = 0.
\end{aligned} \tag{E.17}$$

The second order accurate finite difference forms for the coefficients $\alpha_{i,j}$, $\beta_{i,j}$, $\gamma_{i,j}$, and $J_{i,j}$ for each grid element are,

$$\alpha_{i,j} = \frac{1}{4} [(x_{i+1,j} - x_{i-1,j})^2 + (y_{i+1,j} - y_{i-1,j})^2], \tag{E.18}$$

$$\beta_{i,j} = \frac{1}{4} [(x_{i+1,j} - x_{i-1,j})(x_{i,j+1} - x_{i,j-1}) + (y_{i+1,j} - y_{i-1,j})(y_{i,j+1} - y_{i,j-1})], \tag{E.19}$$

$$\gamma_{i,j} = \frac{1}{4} [(x_{i,j+1} - x_{i,j-1})^2 + (y_{i,j+1} - y_{i,j-1})^2], \tag{E.20}$$

$$J_{i,j} = \frac{1}{4} [(x_{i+1,j} - x_{i-1,j})(y_{i,j+1} - y_{i,j-1}) - (x_{i,j+1} - x_{i,j-1})(y_{i+1,j} - y_{i-1,j})]. \tag{E.21}$$

The finite difference forms of the Poisson equations, (E.16) and (E.17), are solved numerically on the grid $\xi = i, \eta = j$ for $i = 0, 1, \dots, I_{\max}$ and $j = 0, 1, \dots, J_{\max}$ after the one-to-one correspondence between (x, y) and (ξ, η) points is specified. The parameters, P and Q , that control the deformation of the grid in (ξ, η) are set to zero for this problem because such fine grid control is not necessary. The set of nonlinear simultaneous difference equations is solved by point successive overrelaxation (SOR) iteration [Press *et al.*, 1992, pg. 857]. SOR iteration is a modification to Gauss-Seidel iteration where an initial guess is chosen for the solutions to (E.16) and (E.17), and subsequent refined solutions are determined according to standard iteration equations [Hoffman, 1992, p. 57]. The locally optimized overrelaxation parameter is [Thompson *et al.*, 1977]:

$$\Omega_{i,j} = \frac{2}{1 + (1 - \tau_{i,j}^2)^{1/2}}, \tag{E.22}$$

where

$$\tau_{i,j} = \frac{\alpha_{i,j}}{\alpha_{i,j} + \gamma_{i,j}} \cos\left(\frac{\pi}{I_{\max} + 1}\right) + \frac{\gamma_{i,j}}{\alpha_{i,j} + \gamma_{i,j}} \cos\left(\frac{\pi}{J_{\max} + 1}\right). \tag{E.23}$$

For the bifurcating fracture, the system is divided into four regions as shown in Figure E.1. The geometry in the (x, y) plane is defined by assigning a value to the angle θ and by prescribing the lengths r , t , and u of JH, HF, and FE, respectively. In Figure E.1 AC is the line $y = 1$, CE is

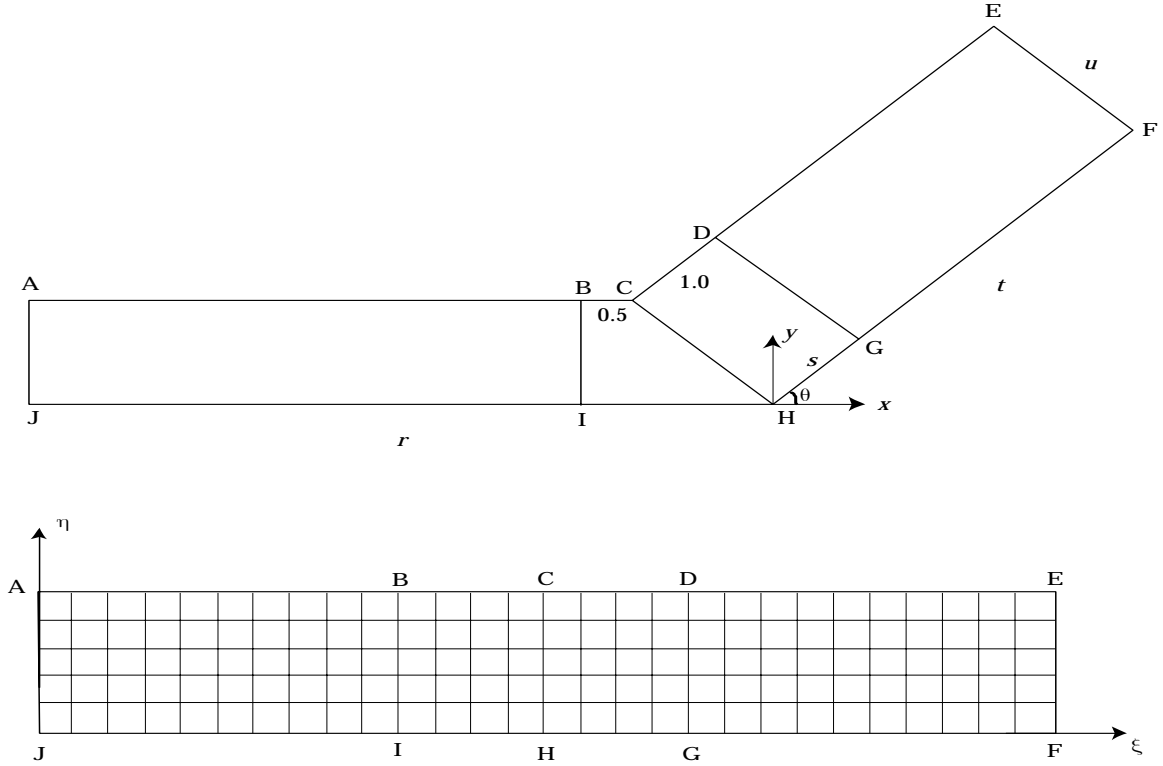


Figure E.1: Coordinate mapping of the bifurcating fracture considered in this study.

$y = x \tan \theta + u \sec \theta$, FE is $y = -x \cot \theta + t \csc \theta$. BC and CD are given lengths 0.5 and 1, respectively, and GH has length $s = \csc \theta - u \cot \theta + 1$ so that GD is parallel to FE. The parameters are selected such that $r = t = 10$ and $u = 1$.

The grid generation algorithm uses five prescribed integers to describe grid spacing: M_I , M_{II} , M_{III} , M_{IV} , and N . It is of note that $J_{\max} = N$ and $I_{\max} = M_I + M_{II} + M_{III} + M_{IV}$. Along JI and AB points are placed with separations $1/2M_{II} + \varrho, 1/2M_{II} + 2\varrho, \dots, 1/2M_{II} + M_I\varrho$ moving from BI to AJ, with ϱ chosen such that the sum of the widths of the M_I intervals is equal to the length of AB. The points on JI and AB provide nodal values at $\eta = 0$ and $\eta = J_{\max}$, respectively, for $\xi = i$, where $i = 0, 1, \dots, M_I - 1$. Along the grid boundary BC points are selected to form equally spaced intervals of width $1/2M_{II}$ and the positions of these points give x and y at the boundary nodes $\xi = i$ for $i = M_I, M_I + 1, \dots, M_I + M_{II}$, $\eta = J_{\max}$. Similarly, equally spaced points along

IH provide the values of x and y at the nodes $\xi = i$ for $i = M_I, M_I + 1, \dots, M_I + M_{II}$, $\eta = 0$. Along CD the points are selected to form M_{III} equally spaced intervals of width $1/M_{III}$. HG is also divided into M_{III} equally spaced intervals. On DE and GF points are selected with separations $1/M_{III} + \varsigma, 1/M_{III} + 2\varsigma, \dots, 1/M_{III} + M_{IV}\varsigma$, with ς chosen such that the sum of the widths of the M_{IV} intervals is equal to the length of GF. The upstream boundary AJ and the downstream boundary FE are divided into N equal subintervals to provide boundary values $\xi = 0$ and $\xi = I_{\max}$, respectively for $\eta = j, j = 0, 1, \dots, J_{\max}$.

To assign initial values to x and y at interior nodes for the SOR algorithm, suppose that for $i = 1, 2, \dots, I_{\max} - 1$ the points in Figure E.1 corresponding to $\xi = i, \eta = 0$ are joined by a straight line to the point that corresponds to $\xi = i, \eta = J_{\max}$. Initial values at $\xi = i, \eta = j$ for $j = 1, \dots, J_{\max} - 1$ are given by points on this line. For $i = 0, 1, \dots, M_I + M_{II}$ the points are the intersections of the straight line with the horizontal lines through boundary points on AJ and for $i = M_I + M_{II} + 1, M_I + M_{II} + 2, \dots, J_{\max}$ the points are the intersections of the straight line with lines of gradient $\tan \theta$ through the boundary points on FE.

To avoid singularities (infinite vorticity) at boundary locations with slope discontinuity, boundary fitted coordinates are used to remove the corner at C and the corner at H is replaced by a blunt stagnation point. To remove the corner at C, points are selected on BC and CD that are situated 0.2 units distant from C and a unique cubic polynomial is specified that matches position and boundary slope at each of these points. That is, the y component of a boundary node with a corresponding x location between the two points is replaced by the y value yielded when that x value is substituted into the cubic. To introduce a blunt nose at the branching point, H is moved from the origin to a location of $(0.2, 0)$. The line IH is then subdivided into M_{II} equally spaced intervals to give boundary values at $\eta = 0$, $\xi = i$ for $i = M_I, M_I + 1, \dots, M_I + M_{II}$. Boundary points corresponding to $\eta = 0$, $\xi > (M_I + M_{II})$ where $x < 0.4$ are replaced by points on the upper branch of the parabola $y^2 = 0.8(x - 0.2)\tan^2 \theta$. This parabola passes smoothly through the boundary

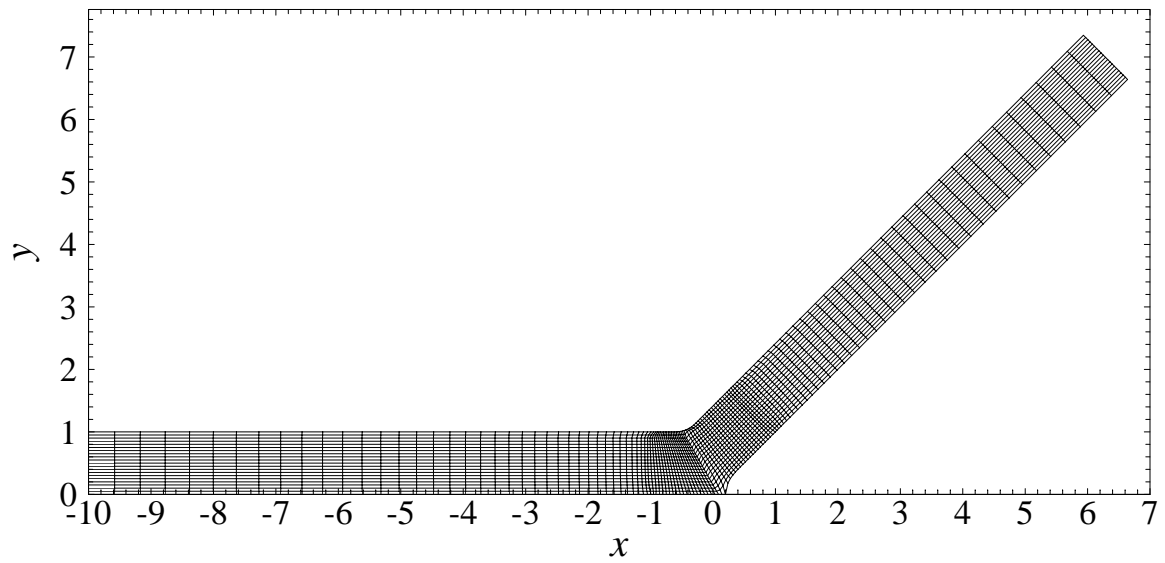


Figure E.2: Nodal mapping of the bifurcating fracture considered in this study. Here, $M_I = 40$, $M_{II} = 20$, $M_{III} = 20$, $M_{IV} = 40$, and $N = 20$.

point $(0.4, 0.4 \tan \theta)$ with gradient $\tan \theta$. A typical grid for this smoothed region, generated by the coordinate mapping algorithm is shown in Figure E.2.

Appendix F

Bifurcating Flow Equations

Finite difference forms of the Navier–Stokes equations are solved to specify the laminar flow field in a bifurcating fracture. Because of the symmetric nature of the system, only the top half of the fracture need be modeled as the bottom half has the mirror image flow field. The Navier–Stokes equations in two dimensions in a Cartesian coordinate system for incompressible flow are:

$$\rho \left(\frac{\partial u}{\partial t} + u \frac{\partial u}{\partial x} + v \frac{\partial u}{\partial y} \right) = \rho g_x - \frac{\partial P}{\partial x} + \mu \left(\frac{\partial^2 u}{\partial x^2} + \frac{\partial^2 u}{\partial y^2} \right) \quad (\text{F.1})$$

$$\rho \left(\frac{\partial v}{\partial t} + u \frac{\partial v}{\partial x} + v \frac{\partial v}{\partial y} \right) = \rho g_y - \frac{\partial P}{\partial y} + \mu \left(\frac{\partial^2 v}{\partial x^2} + \frac{\partial^2 v}{\partial y^2} \right), \quad (\text{F.2})$$

where ρ is the fluid density; u is the velocity in the x -direction; v is the velocity in the y -direction; g_x and g_y are the components of gravitational acceleration in the x - and y -directions, respectively; P is the pressure; and μ is the dynamic viscosity. Taking the derivative of (F.2) with respect to x and subtracting the derivative of (F.1) with respect to y eliminates the pressure and gravity terms in each and allows the recasting of these equations in terms of vorticity, ω , and stream function, ψ . Recall that the stream functions and vorticity are given by:

$$u = \frac{\partial \psi}{\partial y}, \quad (\text{F.3})$$

$$v = -\frac{\partial \psi}{\partial x}, \quad (\text{F.4})$$

$$\omega = \frac{\partial v}{\partial x} - \frac{\partial u}{\partial y}. \quad (\text{F.5})$$

The Navier–Stokes equations become:

$$\frac{\partial \omega}{\partial t} + \frac{\mu}{\rho} \left(\frac{\partial \psi}{\partial y} \frac{\partial \omega}{\partial x} - \frac{\partial \psi}{\partial x} \frac{\partial \omega}{\partial y} \right) = \nabla^2 \omega, \quad (\text{F.6})$$

Because there are two unknowns, ψ and ω , a second equation is necessary. Substituting (F.3) and (F.4) into (F.5) produces:

$$\nabla^2 \psi = -\omega. \quad (\text{F.7})$$

Equations (F.6) and (F.7) must be solved simultaneously to describe the flow field.

The strength of using boundary fitted coordinates lies in the ability to use coordinate mapping to transform a complex domain into a simple rectangular domain. Although this leads to more complex forms of the governing partial differential equations, it allows the use of traditional finite differencing to solve the problem in its entirety. Coordinate mapping was described in Appendix E. Instead of specifying the more complex (x, y) coordinates, coordinates in (ξ, η) are given. Furthermore, as there is a unique one to one correspondence between system points, conformal mapping produces $\xi = \xi(x, y)$ and $\eta = \eta(x, y)$. Because both coordinate values are monotonically increasing, these relationships are invertible and $x = x(\xi, \eta)$ and $y = y(\xi, \eta)$. Any value of a stream line at a point can therefore be written as a function of ξ and η as

$$\psi(x, y) = \psi(x(\xi, \eta), y(\xi, \eta)) = \psi(\xi, \eta). \quad (\text{F.8})$$

In Appendix E, the complex region in the (x, y) plane was mapped onto a rectangle, with boundaries that coincide with coordinate lines (see Figure E.1). However, the governing partial differential equations, (F.6) and (F.7), must be described in terms of ξ and η instead of x and y . Before the complete Navier–Stokes equations in terms of ξ and η are given, the individual derivative terms are presented. Using the chain rule to take derivatives of (F.8) produces

$$\frac{\partial \psi}{\partial \xi} = \frac{\partial \psi}{\partial x} \frac{\partial x}{\partial \xi} + \frac{\partial \psi}{\partial y} \frac{\partial y}{\partial \xi} \quad (\text{F.9})$$

$$\frac{\partial \psi}{\partial \eta} = \frac{\partial \psi}{\partial x} \frac{\partial x}{\partial \eta} + \frac{\partial \psi}{\partial y} \frac{\partial y}{\partial \eta}. \quad (\text{F.10})$$

Solving these equations for $\partial\psi/\partial x$ and $\partial\psi/\partial y$ yields

$$\frac{\partial\psi}{\partial x} = \frac{1}{J} \left(\frac{\partial\psi}{\partial\xi} \frac{\partial y}{\partial\eta} - \frac{\partial\psi}{\partial\eta} \frac{\partial y}{\partial\xi} \right) \quad (\text{F.11})$$

$$\frac{\partial\psi}{\partial y} = \frac{1}{J} \left(\frac{\partial\psi}{\partial\eta} \frac{\partial x}{\partial\xi} - \frac{\partial\psi}{\partial\xi} \frac{\partial x}{\partial\eta} \right), \quad (\text{F.12})$$

where the quantity J is the Jacobian transformation given by (E.8). Similarly the second derivatives are given by

$$\begin{aligned} \frac{\partial^2\psi}{\partial x^2} &= \frac{1}{J^2} \left[\left(\frac{\partial y}{\partial\eta} \right)^2 \frac{\partial^2\psi}{\partial\xi^2} - 2 \frac{\partial y}{\partial\xi} \frac{\partial y}{\partial\eta} \frac{\partial^2\psi}{\partial\xi\partial\eta} + \left(\frac{\partial y}{\partial\xi} \right)^2 \frac{\partial^2\psi}{\partial\eta^2} \right] \\ &+ \frac{1}{J^3} \left\{ \left[\left(\frac{\partial y}{\partial\eta} \right)^2 \frac{\partial^2 y}{\partial\xi^2} - 2 \frac{\partial y}{\partial\xi} \frac{\partial y}{\partial\eta} \frac{\partial^2 y}{\partial\xi\partial\eta} + \left(\frac{\partial y}{\partial\xi} \right)^2 \frac{\partial^2 y}{\partial\eta^2} \right] \left(\frac{\partial x}{\partial\eta} \frac{\partial\psi}{\partial\xi} - \frac{\partial x}{\partial\xi} \frac{\partial\psi}{\partial\eta} \right) \right. \\ &\left. + \left[\left(\frac{\partial y}{\partial\eta} \right)^2 \frac{\partial^2 x}{\partial\xi^2} - 2 \frac{\partial y}{\partial\xi} \frac{\partial y}{\partial\eta} \frac{\partial^2 x}{\partial\xi\partial\eta} + \left(\frac{\partial y}{\partial\xi} \right)^2 \frac{\partial^2 x}{\partial\eta^2} \right] \left(\frac{\partial y}{\partial\xi} \frac{\partial\psi}{\partial\eta} - \frac{\partial y}{\partial\eta} \frac{\partial\psi}{\partial\xi} \right) \right\}, \quad (\text{F.13}) \end{aligned}$$

$$\begin{aligned} \frac{\partial^2\psi}{\partial x\partial y} &= \frac{1}{J^2} \left[\left(\frac{\partial x}{\partial\xi} \frac{\partial y}{\partial\eta} + \frac{\partial x}{\partial\eta} \frac{\partial y}{\partial\xi} \right) \frac{\partial^2\psi}{\partial\xi\partial\eta} - \frac{\partial x}{\partial\xi} \frac{\partial y}{\partial\xi} \frac{\partial^2\psi}{\partial\eta^2} - \frac{\partial x}{\partial\eta} \frac{\partial y}{\partial\eta} \frac{\partial^2\psi}{\partial\xi^2} \right] \\ &+ \left[\frac{1}{J^3} \left(\frac{\partial x}{\partial\xi} \frac{\partial^2 y}{\partial\eta^2} - \frac{\partial x}{\partial\eta} \frac{\partial^2 y}{\partial\xi\partial\eta} \right) + \frac{1}{J^3} \left(\frac{\partial x}{\partial\eta} \frac{\partial y}{\partial\eta} \frac{\partial J}{\partial\xi} - \frac{\partial x}{\partial\xi} \frac{\partial y}{\partial\eta} \frac{\partial J}{\partial\eta} \right) \right] \frac{\partial\psi}{\partial\xi} \\ &+ \left[\frac{1}{J^2} \left(\frac{\partial x}{\partial\eta} \frac{\partial^2 y}{\partial\xi^2} - \frac{\partial x}{\partial\xi} \frac{\partial y}{\partial\eta\xi} \right) + \frac{1}{J^3} \left(\frac{\partial x}{\partial\xi} \frac{\partial y}{\partial\eta} \frac{\partial J}{\partial\eta} - \frac{\partial x}{\partial\eta} \frac{\partial y}{\partial\xi} \frac{\partial J}{\partial\xi} \right) \right] \frac{\partial\psi}{\partial\eta}, \quad (\text{F.14}) \end{aligned}$$

$$\begin{aligned} \frac{\partial^2\psi}{\partial y^2} &= \frac{1}{J^2} \left[\left(\frac{\partial x}{\partial\eta} \right)^2 \frac{\partial^2\psi}{\partial\xi^2} - 2 \frac{\partial x}{\partial\xi} \frac{\partial x}{\partial\eta} \frac{\partial^2\psi}{\partial\xi\partial\eta} + \left(\frac{\partial x}{\partial\xi} \right)^2 \frac{\partial^2\psi}{\partial\eta^2} \right] \\ &+ \frac{1}{J^3} \left\{ \left[\left(\frac{\partial x}{\partial\eta} \right)^2 \frac{\partial^2 y}{\partial\xi^2} - 2 \frac{\partial x}{\partial\xi} \frac{\partial x}{\partial\eta} \frac{\partial^2 y}{\partial\xi\partial\eta} + \left(\frac{\partial x}{\partial\xi} \right)^2 \frac{\partial^2 y}{\partial\eta^2} \right] \left(\frac{\partial x}{\partial\eta} \frac{\partial\psi}{\partial\xi} - \frac{\partial x}{\partial\xi} \frac{\partial\psi}{\partial\eta} \right) \right. \\ &\left. + \left[\left(\frac{\partial x}{\partial\eta} \right)^2 \frac{\partial^2\psi}{\partial\xi^2} - 2 \frac{\partial x}{\partial\xi} \frac{\partial x}{\partial\eta} \frac{\partial^2\psi}{\partial\xi\partial\eta} + \left(\frac{\partial x}{\partial\xi} \right)^2 \frac{\partial^2\psi}{\partial\eta^2} \right] \left(\frac{\partial y}{\partial\xi} \frac{\partial\psi}{\partial\eta} - \frac{\partial y}{\partial\eta} \frac{\partial\psi}{\partial\xi} \right) \right\}. \quad (\text{F.15}) \end{aligned}$$

The transformed Laplace equation for the stream function in non-conservative form is:

$$\begin{aligned} \nabla^2\psi &= \frac{1}{J^2} \left[\left(\frac{\partial x^2}{\partial\eta} + \frac{\partial y^2}{\partial\eta} \right) \frac{\partial^2\psi}{\partial\xi^2} - 2 \left(\frac{\partial x}{\partial\xi} \frac{\partial x}{\partial\eta} + \frac{\partial y}{\partial\xi} \frac{\partial y}{\partial\eta} \right) \frac{\partial^2\psi}{\partial\xi\partial\eta} + \left(\frac{\partial x^2}{\partial\xi} + \frac{\partial y^2}{\partial\xi} \right) \frac{\partial^2\psi}{\partial\eta^2} \right] \\ &+ \nabla^2\xi \frac{\partial\psi}{\partial\xi} + \nabla^2\eta \frac{\partial\psi}{\partial\eta}. \quad (\text{F.16}) \end{aligned}$$

Recall that the Laplacians of ξ and η were set to zero in the grid generation step as described in Appendix E thereby eliminating the terms involving $\nabla^2\xi$ and $\nabla^2\eta$.

The governing equations, (F.6) and (F.7), may now be expressed on the transformed rectangular grid as:

$$\frac{\partial \omega}{\partial t} + \frac{1}{J} \left(\frac{\partial \psi}{\partial \eta} \frac{\partial \omega}{\partial \xi} - \frac{\partial \psi}{\partial \xi} \frac{\partial \omega}{\partial \eta} \right) = \frac{\nu}{J^2} \left(\alpha \frac{\partial^2 \omega}{\partial \xi^2} - 2\beta \frac{\partial^2 \omega}{\partial \xi \partial \eta} + \gamma \frac{\partial^2 \omega}{\partial \eta^2} \right), \quad (\text{F.17})$$

$$\frac{1}{J^2} \left(\alpha \frac{\partial^2 \psi}{\partial \xi^2} - 2\beta \frac{\partial^2 \psi}{\partial \xi \partial \eta} + \gamma \frac{\partial^2 \psi}{\partial \eta^2} \right) = -\omega, \quad (\text{F.18})$$

respectively, where α , β , and γ are defined by (E.13), (E.14), and (E.15), respectively.

In addition to the preceding governing equations, boundary conditions must be specified for both ψ and ω on all four sides of the (ξ, η) grid. There is half-parabolic inflow at $\xi = 0$ and parabolic outflow at $\xi = I_{\max}$. The stream function and vorticity at the inflow boundary take the forms [Bramley and Dennis, 1984; Bramley and Sloan, 1987; Lonsdale et al., 1988]:

$$\psi_{0,j} = \frac{1}{2} \left(\frac{j}{J_{\max}} \right) \left[3 - \left(\frac{j}{J_{\max}} \right)^2 \right], \quad (\text{F.19})$$

$$\omega_{0,j} = \left(\frac{12b^2}{d^2} \right) \left(\frac{j}{J_{\max}} \right). \quad (\text{F.20})$$

Along the outflow boundary the stream function and vorticity are:

$$\psi_{I_{\max},j} = \left(\frac{j}{J_{\max}} \right)^2 \left[3 - 2 \left(\frac{j}{J_{\max}} \right) \right], \quad (\text{F.21})$$

$$\omega_{I_{\max},j} = \frac{6}{d^2} \left[2 \left(\frac{j}{J_{\max}} \right) - 1 \right]. \quad (\text{F.22})$$

As seen in Figure E.1, $0.5b = 1$ is the half-aperture of the parent fracture and $d = u$ is the aperture of the daughter fractures.

Along $\eta = 0$, the stream function is assigned a value of $\psi = 0$ and along $\eta = J_{\max}$, the stream function has a value of $\psi = 1$. Further, all order derivatives of the stream function in the ξ direction are zero along solid boundaries as are first derivatives in the η direction.

At the lower wall given by $\eta = 0$ there is no vorticity before the bifurcation. After this point, along $\eta = 0$ and for the whole of the length of $\eta = J_{\max}$ the no-slip boundary condition is enforced. The vorticity at solid boundaries is determined by first rewriting the stream function in a

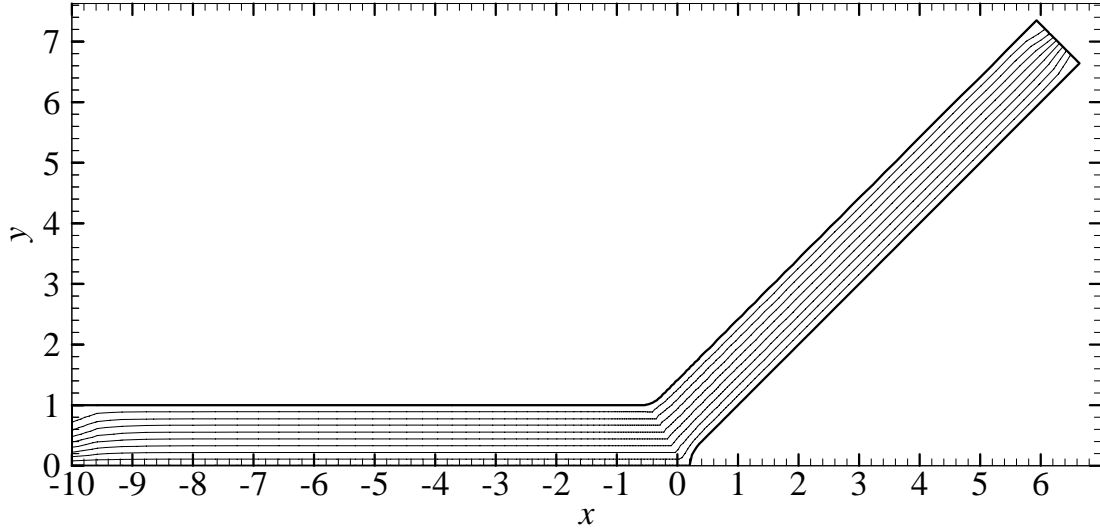


Figure F.1: Contour plot of the streamlines in a bifurcating fracture.

Taylor Series Expansion (TSE) from the boundary into the fracture. The TSE about $\eta = 0$ in the positive η direction is:

$$\psi_{i,0} = \psi_{i,1} + \Delta\eta \frac{\partial\psi_{i,1}}{\partial\eta} + \frac{(\Delta\eta)^2}{2} \frac{\partial^2\psi_{i,1}}{\partial\eta^2} + O(\Delta\eta)^3. \quad (\text{F.23})$$

Recalling that derivatives terms of ψ with respect to ξ are zero, using (F.7) the vorticity at the wall can be rewritten as

$$\omega_{i,0} = \frac{1}{J^2} \left[\left(\frac{\partial^2 x}{\partial \xi^2} \right)^2 + \left(\frac{\partial^2 y}{\partial \xi^2} \right)^2 \right] \frac{\partial^2 \psi}{\partial \eta^2}. \quad (\text{F.24})$$

Using the fact that $\partial\psi/\partial\xi = \partial\psi^2/\partial\xi^2 = \partial\psi/\partial\eta = 0$ at the wall and substituting $\partial^2\psi_{i,1}/\partial\eta^2$ from (F.23) yields the following boundary vorticity

$$\omega_{i,0} = \frac{2}{J^2} \left[\left(\frac{\partial^2 x}{\partial \xi^2} \right)^2 + \left(\frac{\partial^2 y}{\partial \xi^2} \right)^2 \right] (\psi_{i,0} - \psi_{i,1}), \quad (\text{F.25})$$

for the bottom wall after the bifurcation and by a similar expression for the whole of the top wall of the fracture where $\eta = J_{\max}$.

The coupled partial differential equations (F.17) and (F.18) are solved for ψ and ω . Vorticity is initially assumed to be zero everywhere in the system and (F.18) is solved subject to the previously defined boundary conditions using a fully implicit compact matrix solver [Press et al., 1992, p. 1020].

The stream functions obtained from the solution (F.18) are used in an explicit scheme marching in time to solve for the vorticity in (F.17). The vorticity is then substituted back into (F.18) and the process is repeated until a steady state is reached for the vorticity. The resulting streamlines for the top half of a bifurcating fracture are shown in Figure F.1.

Bibliography

- Abdel-Salam, A., Modeling of contaminant/colloid transport and unsaturated flow in fractured media, Ph.D. thesis, Univ. Calif. Irvine, 1995.
- Abdel-Salam, A., and C. V. Chrysikopoulos, Analytical solutions for one-dimensional colloid transport in saturated fractures, *Adv. Water Resour.*, *17*, 283–296, 1994.
- Abdel-Salam, A., and C. V. Chrysikopoulos, Analysis of a model for contaminant transport in fractured media in the presence of colloids, *J. Hydrol.*, *165*, 261–281, 1995a.
- Abdel-Salam, A., and C. V. Chrysikopoulos, Modeling of colloid and colloid-facilitated contaminant transport in a two-dimensional fracture with spatially variable aperture, *Transp. Porous Media*, *20*, 197–221, 1995b.
- Abdel-Salam, A., and C. V. Chrysikopoulos, Unsaturated flow in a quasi-three-dimensional fractured medium with spatially variable aperture, *Water Resour. Res.*, *32*, 1531–1540, 1996.
- Abelin, H., Migration in a single fracture: An in situ experiment in a natural fracture, Ph.D. thesis, R. Inst. of Tech., Stockholm, 1986.
- Adamczyk, Z., and T. G. M. van de Ven, Deposition of particles under external forces in laminar flow through parallel-plate and cylindrical channels, *J. Colloid Interface Sci.*, *80*, 340–356, 1980.
- Adamczyk, Z., T. Dabros, J. Czarnecki, and T. G. M. van de Ven, Kinetics of particle accumulation

- at collector surfaces I. Approximate analytical solutions, *Adv. Colloid Interface Sci.*, *19*, 183–252, 1983.
- Adamczyk, Z., B. Siwek, and M. Zembala, Kinetics of localized adsorption of particles on homogeneous surfaces, *J. Colloid and Interface Sci.*, *151*, 351–367, 1991.
- Adamczyk, Z., B. Siwek, and M. Zembala, Reversible and irreversible adsorption of particles on homogeneous surfaces, *Colloids and Surfaces*, *62*, 119–130, 1992a.
- Adamczyk, Z., B. Siwek, M. Zembala, and P. Weroński, Kinetics of localized adsorption of colloid particles, *Langmuir*, *8*, 2605–2610, 1992b.
- Adamczyk, Z., B. Siwek, M. Zembala, and P. Weroński, Influence of polydispersity on random sequential adsorption of spherical particles, *J. Colloid Interface Sci.*, *185*, 236–244, 1997.
- Ahlstrom, S. W., H. P. Foote, R. C. Arnett, C. R. Cole, and R. J. Serne, Multicomponent mass transport model: Theory and numerical implementation (discrete–parcel–random–walk version), *Tech. rep.*, Atlantic Richfield Hanford Company, Richland, Washington, 1977.
- Ang, A. H.-S., and W. H. Tang, *Probability Concepts in Engineering Planning and Design*, Wiley, 1975.
- Aris, R., On the dispersion of a solute in a fluid flowing through a tube, *Proc. R. Soc. London A*, *235*, 67–77, 1956.
- Atteia, O., and R. Kozel, Particle size distributions in waters from a karstic aquifer: From particle to colloids, *J. Hydrol.*, *201*, 102–119, 1997.
- Bales, R. C., C. P. Gerba, G. H. Grondin, and S. L. Jensen, Bacteriophage transport in a sandy soil and fractured tuff, *Appl. Env. Microbio.*, *55*, 2061–2067, 1989.
- Banks, J., J. S. C. II, and B. L. Nelson, *Discrete–event System Simulation*, 2 ed., Prentice Hall, 1996.

- Barenblatt, G. I., L. P. Zheltov, and I. N. Kochina, Basic concepts in the theory of seepage of homogeneous liquids in fissured rocks, *J. Appl. Math. Mech.*, *24*, 852–864, 1960.
- Bear, J., *Dynamics of Fluids in Porous Media*, Elsevier, 1972.
- Bear, J., and A. Verruijt, *Modeling Groundwater Flow and Pollution*, Reidel, 1987.
- Bensabat, J., Q. Zhou, and J. Bear, An adaptive pathline-based particle tracking algorithm for the Eulerian–Lagrangian method, *Adv. Water Resour.*, *23*, 383–397, 2000.
- Bergendahl, J., and D. Grasso, Prediction of colloid detachment in a model porous media: Hydrodynamics, *Chem. Eng. Sci.*, *55*, 1523–1532, 2000.
- Berkowitz, B., and J. Zhou, Reactive solute transport in a single fracture, *Water Resour. Res.*, *32*, 901–913, 1996.
- Bird, R. B., W. E. Stewart, and E. N. Lightfoot, *Transport Phenomena*, John Wiley and Sons, 1960.
- Bowen, D. D., and N. Epstein, Fine particle deposition in smooth parallel plate channels, *J. Colloid Interface Sci.*, *72*, 81–97, 1979.
- Bradbury, M. H., and A. Green, Investigations into the factors influencing long range matrix diffusion rates and pore space accessibility at depth in granite, *J. Hydrol.*, *89*, 123–139, 1986.
- Bramley, J. S., and S. C. R. Dennis, The numerical solution of two-dimensional flow in a branching channel, *Computers Fluids*, *12*, 339–355, 1984.
- Bramley, J. S., and D. M. Sloan, Numerical solution for the two-dimensional flow in a branching channel using boundary fitted coordinates, *Computers Fluids*, *15*, 297–311, 1987.
- Brenner, H., A general theory of Taylor dispersion phenomena, *Physicochem. Hydrodynam.*, *1*, 91–123, 1980.
- Brenner, H., A general theory of Taylor dispersion phenomena II: An extension, *Physicochem. Hydrodynam.*, *3*, 133–157, 1982.

- Brenner, H., and D. A. Edwards, *Macrotransport processes*, Butterworth–Heinemann, 1993.
- Brown, S. R., Fluid flow through rock joints: The effect of surface roughness, *J. Geophys. Res.*, *92*, 1337–1347, 1987.
- Brown, S. R., Simple mathematical model of a rough fracture, *J. Geophys. Res.*, *100*, 5941–5952, 1995.
- Brown, S. R., H. W. Stockman, and S. J. Reeves, Applicability of the Reynolds equation for modeling fluid flow between rough surfaces, *Geophys. Res. Letters*, *22*, 2537–2540, 1995.
- Buckley, R. I., and S. K. Loyalka, Radionuclide migration in fractured media: Numerical studies of advection/diffusion in a fracture and diffusion in the surrounding rock matrix, *Ann. Nuc. Energy*, *20*, 701–718, 1993.
- Buckley, R. I., and S. K. Loyalka, Numerical studies of solute transport in a fracture surrounded by rock matrix: Effect of lateral diffusion and chemical reactions on the overall dispersion, *Ann. Nuc. Energy*, *21*, 461–494, 1994.
- Buddemeier, R. W., and J. R. Hunt, Transport of colloidal contaminants in groundwater radionuclide migration at the Nevada test site, *Applied Geochemistry*, *3*, 535–548, 1988.
- Butt, J. B., *Reaction kinetics and reactor design*, Prentice–Hall, 1980.
- Cacas, M. C., E. Ledoux, G. de Marsily, and B. Tillie, Modeling fracture flow with a stochastic discrete fracture network: calibration and validation, I: The flow model, *Water Resour. Res.*, *26*, 479–489, 1990a.
- Cacas, M. C., E. Ledoux, G. de Marsily, and B. Tillie, Modeling fracture flow with a stochastic discrete fracture network: calibration and validation, II: The transport model, *Water Resour. Res.*, *26*, 491–500, 1990b.
- Carslaw, H. S., and J. C. Jaeger, *Conduction of heat in solids*, 2 ed., University Press, Oxford, 1988.

- Champ, D. R., and J. Schroeter, Bacterial transport in fractured rock: A field-scale tracer test at the Chalk River Nuclear Laboratories, *Water Sci. Technol.*, *20*, 81–87, 1988.
- Chiou, C. T., R. L. Malcom, T. I. Brinton, and D. E. Kile, Water solubility enhancement of some organic pollutants and pesticides by dissolved humic and fulvic acids, *Env. Sci. Technol.*, *20*, 502–508, 1986.
- Chrysikopoulos, C. V., Effective parameters for flow in saturated heterogeneous porous media, *J. Hydrol.*, *170*, 181–198, 1995.
- Chrysikopoulos, C. V., and A. Abdel-Salam, Modeling colloid transport and deposition in saturated fractures, *Colloids Surfaces A: Physicochem. Eng. Aspects*, *121*, 189–202, 1997.
- Chrysikopoulos, C. V., and Y. Sim, One-dimensional virus transport in homogeneous porous media with time dependent distribution coefficient, *J. Hydrol.*, *185*, 199–219, 1996.
- Chrysikopoulos, C. V., P. K. Kitanidis, and P. V. Roberts, Generalized Taylor–Aris moment analysis of the transport of sorbing solutes through porous media with spatially-periodic retardation factor, *Transp. Porous Media*, *7*, 163–185, 1992.
- Contardi, J. S., D. R. Turner, and T. M. Ahn, Modeling colloid transport for performance assessment, *J. Contam. Hydrol.*, *47*, 323–333, 2001.
- Corapcioglu, M. Y., and S. Jiang, Colloid facilitated groundwater contaminant transport, *Water Resour. Res.*, *29*, 2215–2226, 1993.
- Cormenzana, J., Transport of a two-member decay chain in a single fracture: Simplified analytical solution for two radionuclides with the same transport properties, *Water Resour. Res.*, *36*, 1339–1346, 2000.
- Dagan, G., Analysis of flow through heterogeneous random aquifers, 2: Unsteady flow in confined formations, *Water Resour. Res.*, *18*, 1571–1585, 1982.

- de Marsily, G., *Quantitative Hydrogeology: Groundwater Hydrology for Engineers*, Academic Press, 1986.
- DeGance, A. E., and L. E. Johns, On the dispersion coefficients for Poiseuille flow in a circular cylinder, *Appl. Sci. Res.*, *34*, 227–258, 1978.
- di Federico, V., Non-Newtonian flow in a variable aperture fracture, *Transp. Porous Media*, *30*, 75–86, 1998.
- Dijk, P., and B. Berkowitz, Precipitation and dissolution of reactive solutes in fractures, *Water Resour. Res.*, *34*, 457–470, 1998.
- Dijk, P., B. Berkowitz, and P. Bendel, Investigation of flow in water-saturated rock fractures using nuclear magnetic resonance imaging (NMRI), *Water Resour. Res.*, *35*, 347–360, 1999.
- Domenico, P. A., and F. W. Schwartz, *Physical and Chemical Hydrogeology*, Wiley, 1990.
- Drever, J. I., *The Chemistry of Weathering*, Reidel, Dordrecht, 1985.
- Elimelech, M., J. Gregory, X. Jia, and R. Williams, *Particle Deposition & Aggregation: Measurement, Modeling and Simulation*, Butterworth-Heinemann, 1995.
- Enfield, C. G., and G. Bengtsson, Macromolecular transport of hydrophobic contaminants in aqueous environments, *Ground Water*, *26*, 64–70, 1988.
- Fox, R. W., and A. T. McDonald, *Introduction to Fluid Mechanics*, 4 ed., John Wiley and Sons, 1992.
- Gavrilenko, P., and Y. Guéguen, Flow in fractured media: A modified renormalization method, *Water Resour. Res.*, *34*, 177–191, 1998.
- Ge, S., A governing equation for fluid flow in rough fractures, *Water Resour. Res.*, *33*, 53–61, 1997.
- Gelhar, L., and C. L. Axness, Three-dimensional stochastic analysis of macrodispersion in aquifers, *Water Resour. Res.*, *19*, 161–180, 1983.

- Goldman, A. J., R. G. Cox, and H. Brenner, Slow viscous motion of a sphere parallel to a plane wall I: Motion through quiescent fluid, *Chem. Eng. Sci.*, *22*, 637–651, 1967.
- Grindrod, P., The impact of colloids on the migration and dispersal of radionuclides within fractured rock, *J. Contam. Hydrol.*, *13*, 167–181, 1993.
- Grindrod, P., and A. J. Lee, Colloid migration in symmetrical non-uniform fractures: Particle tracking in three dimensions, *J. Contam. Hydrol.*, *27*, 157–175, 1997.
- Gringarten, A. C., J. H. J. Ramey, and R. Raghaven, Unsteady-state pressure distributions created by a well with a single infinite conductivity vertical fracture, *Soc. Pet. Eng. J.*, *14*, 347–360, 1974.
- Grisak, G. E., and J. A. Cherry, Hydrologic characteristics and response of fractured till and clay confining a shallow aquifer, *Canadian Geotechnical J.*, *12*, 23–43, 1975.
- Grisak, G. E., and J. F. Pickens, An analytical solution for solute transport through fractured media with matrix diffusion, *J. Hydrol.*, *52*, 47–57, 1981.
- Grolimund, D., and M. Borkovec, Long-term release kinetics of colloidal particles from natural porous media, *Env. Sci. Tech.*, *33*, 4–54–4060, 1999.
- Gutjahr, A. L., Fast Fourier Transform for Random Field Generation, *Project report for los alamos grant, contract 4-r58-2690r*, New Mexico Institute of Mining and Technology, Socorro, New Mexico, 1989.
- Haber, S., and H. Brenner, Effect of entrained colloidal particles in enhancing the transport of adsorbable chemical contaminants, *J. Colloid and Interface Sci.*, *155*, 226–246, 1993.
- Haldeman, W. R., Y. Chuang, T. C. Rasmussen, and D. D. Evans, Laboratory analysis of fluid flow and solute transport through a fracture embedded in porous tuff, *Water Resour. Res.*, *27*, 53–65, 1991.

- Happel, J., and H. Brenner, *Low Reynolds Number Hydrodynamics with Special Applications to Particulate Media*, Prentice-Hall, 1965.
- Harvey, R. W., L. H. George, R. L. Smith, and D. R. LeBlanc, Transport of fluorescent microsphere and indigenous bacteria through a sandy aquifer: Results of natural- and forced-gradient tracer experiment, *Env. Sci. and Technol.*, *23*, 51-56, 1989.
- Hasegawa, E., and H. Izuchi, On steady flow through a channel consisting of an uneven wall and a plane wall I: Case of no relative motion in two walls, *Bull. Jpn. Soc. Mech. Eng.*, *26*, 514-520, 1983.
- Hinrichsen, E. L., J. Feder, and T. Jossang, Random packing of disks in two dimensions, *Physical Rev. A*, *41*, 4199-4209, 1990.
- Hoffman, J. D., *Numerical Methods for Engineers and Scientists*, McGraw-Hill, 1992.
- Ibaraki, M., and E. A. Sudicky, Colloid-facilitated contaminant transport in discretely fractured porous media 1. Numerical formulation and sensitivity analysis, *Water Resour. Res.*, *31*, 2945-2960, 1995.
- James, S. C., and C. V. Chrysikopoulos, Transport of polydisperse colloid suspensions in a single fracture, *Water Resour. Res.*, *35*, 707-718, 1999.
- James, S. C., and C. V. Chrysikopoulos, Polydisperse colloid transport through a variable aperture fracture, *Water Resour. Res.*, *36*, 1457-1466, 2000.
- James, S. C., and C. V. Chrysikopoulos, Analytical solutions for the transport of monodisperse and polydisperse particle suspensions in a uniform fracture, *Proc. R. Soc. London A*, *000*, 2001a.
- James, S. C., and C. V. Chrysikopoulos, Effective velocity and effective dispersion coefficient for finitely sized particles flowing in a uniform fracture, *Water Resour. Res.*, *000*, 2001b.

- Johns, L. E., and A. E. DeGance, Dispersion approximations to the multicomponent convective diffusion equation for chemically active systems, *Chem. Eng. Sci.*, *30*, 1065–1067, 1975.
- Johns, R. A., and P. V. Roberts, A solute transport model for channelized flow in a fracture, *Water Resour. Res.*, *27*, 1797–1808, 1991.
- Johns, R. A., J. S. Steade, L. M. Costanier, and P. V. Roberts, Nondestructive measurements of fracture aperture in crystalline rock cores using X-ray computed tomography, *J. Geophys. Res.*, *98*, 1889–1900, 1993.
- Johnson, R., S. Ning, and M. Elimelech, Colloid transport in geochemically heterogeneous porous media: Modeling and measurements, *Env. Sci. Technol.*, *30*, 3284–3293, 1996.
- Keller, A. A., High resolution non-destructive measurement and characterization of fracture apertures, *Int. J. Rock Mech. Min. Sci.*, *35*, 1037–1050, 1998.
- Keller, A. A., P. V. Roberts, and M. J. Blunt, Effect of fracture aperture variations on the dispersion of contaminants, *Water Resour. Res.*, *35*, 55–63, 1999.
- Kinzelbach, W., *Groundwater Flow and Quality Modeling*, chap. The random walk method in pollutant transport simulation, pp. 227–245, Reidel, Dordrecht, 1988.
- Kirkpatrick, S., Percolation and conduction, *Rev. Modern. Phys.*, *45*, 574–588, 1973.
- Kitanidis, P. K., Particle-tracking equations for the solution of the advection–dispersion equation with variable coefficients, *Water Resour. Res.*, *30*, 3225–3227, 1994.
- Krishnamoorthy, T. M., R. N. Nair, and T. P. Sarma, Migration of radionuclides from a granite repository, *Water Resour. Res.*, *28*, 1927–1934, 1992.
- Kumar, S., R. W. Zimmerman, and G. S. Bodvarsson, Permeability of a fracture with cylindrical asperities, *Fluid Dyn. Res.*, *7*, 131–137, 1990.

- Lægdsmand, M., K. G. Villholth, M. Ullum, and K. H. Jensen, Processes of colloid mobilization and transport in macroporous soil monoliths, *Geoderma*, *93*, 33–59, 1999.
- Lartiges, B. S., S. Deneux-Mustin, G. Villemin, C. Mustin, O. Barrès, M. Chamerois, B. Gerard, and M. Babut, Composition, structure and size distribution of suspended particulates from the Rhine River, *Water Ter.*, *35*, 808–816, 2001.
- Ledin, A., S. Karlsson, A. Düker, and B. Allard, Measurements in situ of concentration and size distribution of colloidal matter in deep groundwater by photon correlation spectroscopy, *Water Res.*, *28*, 1539–1545, 1994.
- Lieser, K. H., A. Ament, R. Hill, R. N. Singh, U. Stingl, and B. Thybusch, Colloids in groundwater and their influence on migration of trace elements and radionuclides, *Radiochimica Acta*, *49*, 83–100, 1990.
- Liu, H. H., G. S. Bodvarsson, and L. Pan, Determination of particle transfer in random walk particle methods for fractured porous media, *Water Resour. Res.*, *36*, 707–713, 2000.
- Long, J. C., and P. A. Witherspoon, The relationship of the degree of interconnection to permeability of fracture networks, *J. Geophys. Res.*, *90*, 3087–3098, 1985.
- Lonsdale, G., J. S. Bramley, and D. M. Sloan, A nonlinear multigrid algorithm and boundary-fitted coordinates for the solution of a two-dimensional flow in a branching channel, *J. Comp. Phys.*, *78*, 1–14, 1988.
- Lowell, R. P., Contaminant transport in a single fracture: Periodic boundary and flow conditions, *Water Resour. Res.*, *25*, 774–780, 1989.
- Lu, N., A semianalytical method of path line computation for transient finite-difference groundwater flow models, *Water Resour. Res.*, *30*, 2449–2459, 2000.
- McCarthy, J. F., and J. M. Zachara, Subsurface transport of contaminants, *Env. Sci. and Technol.*, *23*, 1989.

- McDowell-Boyer, L. M., J. R. Hunt, and N. Sitar, Particle transport through porous media, *Water Resour. Res.*, *22*, 1901–1921, 1986.
- McTigue, D. F., R. C. Gilver, and J. W. Nunziato, Rheological effects of nonuniform particle distributions in dilute suspensions, *J. Rheology*, *30*, 1053–1076, 1986.
- Michalak, A. M., and P. K. Kitanidis, Macroscopic behavior and random-walk particle tracking of kinetically sorbing solutes, *Water Resour. Res.*, *36*, 2133–2146, 2000.
- Mills, W. B., S. Liu, and F. K. Fong, Literature review and model (COMET) for colloid/metals transport in porous media, *Ground Water*, *29*, 199–208, 1991.
- Moreno, L., Y. W. Tsang, C. F. Tsang, F. V. Hale, and I. Neretnieks, Flow and tracer transport in a single fracture: A stochastic model and its relation to some field observations, *Water Resour. Res.*, *24*, 2033–2048, 1988.
- Moreno, L., B. Gylling, and I. Neretnieks, Solute transport in fractured media — the important mechanisms for performance assessment, *J. Contam. Hydrol.*, *25*, 283–298, 1997.
- Moulin, V., and G. Ouzounian, Role of colloids and humic substances in the transport of radioelements through the geosphere, *Applied Geochemistry*, *1*, 179–186, 1992.
- Neretnieks, I., A note on fracture flow dispersion mechanisms in the ground, *Water Resour. Res.*, *23*, 561–570, 1983.
- Neretnieks, I., T. Eriksen, and P. Tahtinen, Tracer movement in a single fissure in granitic rock: Some experimental results and their interpretation, *Water Resour. Res.*, *18*, 849–858, 1982.
- Neuzil, C. E., and J. V. Tracy, Flow through fractures, *Water Resour. Res.*, *17*, 191–199, 1981.
- Novakowski, K. S., G. V. Evans, D. A. Lever, and K. Raven, A field example of measuring hydrodynamic dispersion in a single fracture, *Water Resour. Res.*, *21*, 1165–1174, 1985.

- Novakowski, K. S., P. A. Lapcevic, J. Voralek, and G. Bickerton, Preliminary interpretation of tracer experiments conducted in a discrete rock fracture under conditions of natural flow, *Geophys. Res. Lett.*, *22*, 1417–1420, 1995.
- Oron, A. P., and B. Berkowitz, Flow in rock fractures: The local cubic law assumption reexamined, *Water Resour. Res.*, *34*, 2811–2825, 1998.
- Pezzullo, J. C., <http://members.aol.com/johnp71/nonlin.html>, 2000.
- Press, W. H., S. A. Teukolsky, W. T. Vetterling, and B. P. Flannery, *Numerical Recipes in FORTRAN*, Cambridge University Press, 1992.
- Puls, R. W., and R. M. Powell, Transport of inorganic colloids through natural aquifer material: Implications for contaminant transport, *Env. Sci. and Technol.*, *26*, 614–621, 1992.
- Puls, R. W., C. J. Paul, and D. A. Clark, Surface chemical effects on colloid stability and transport through natural porous media, *Colloids and Surfaces A*, *73*, 287–300, 1993.
- Rajagopalan, R., and R. Q. Chu, Dynamics of adsorption of colloidal particles in packed beds, *J. Colloid Interface Sci.*, *86*, 299–317, 1981.
- Rasmuson, A., Analysis of hydrodynamic dispersion in discrete fracture networks using the method of moments, *Water Resour. Res.*, *21*, 1677–1683, 1985.
- Rasmuson, A., and I. Neretnieks, Radionuclide transport in fast channels in crystalline rock, *Water Resour. Res.*, *22*, 1247–1256, 1986.
- Raven, K. G., K. S. Novakowski, and P. A. Lapeciv, Interpretation of field tracer tests of a single fracture using a transient solute storage model, *Water Resour. Res.*, *24*, 2019–2032, 1988.
- Rehmann, L. C., C. C. Welty, and R. W. Harvey, Stochastic analysis of virus transport in aquifers, *Water Resour. Res.*, *35*, 1987–2006, 1999.

- Reimus, P. W., The use of synthetic colloids in tracer transport experiments in saturated rock fracture, Ph.D. thesis, Los Alamos National Laboratory, 1995, LA-13004-T.
- Reimus, P. W., B. A. Robinson, and R. J. Glass, Aperture characteristics, saturated fluid-flow, and tracer-transport calculations for a natural fracture, in *High-level radioactive waste management*, pp. 2009-2016, 1993.
- Robinson, N. I., J. M. S. Jr., and I. Kreisel, Contaminant transport in sets of parallel finite fractures with skins, *J. Contam. Hydrol.*, *31*, 83-109, 1998.
- Robinson, P. C., Connectivity of fracture systems: A percolation theory approach, *J. Phys. and Math. Gen.*, *16*, 605-614, 1983.
- Rubin, H., D. Jansen, C. Forkel, and J. Köngeter, Simulation of contaminant transport in fractured permeable formations by multiporosity modeling, *J. Hydrol.*, *223*, 107-130, 1999.
- Sankarasubramanian, R., and W. N. Gill, Unsteady convective diffusion with interphase mass transfer, *Proc. R. Soc. London A*, *333*, 115-132, 1974, (correction, *Proc. R. Soc. London A*, *341*, 407-408).
- Schaaf, P., and J. Talbot, Surface exclusion effects in adsorption processes, *J. Chem. Phys.*, *7*, 1989.
- Schrauf, T. W., and D. D. Evans, Laboratory studies of gas flow through a single natural fracture, *Water Resour. Res.*, *22*, 1038-1050, 1986.
- Schwartz, F. W., L. Smith, and A. S. Crowe, A stochastic analysis of macroscopic dispersion in fractured media, *Water Resour. Res.*, *19*, 1253-1265, 1983.
- Shapiro, A. M., and J. R. Nicholas, Estimating the statistical properties of fracture aperture using field scale hydraulic and tracer tests: Theory and application, *Water Resour. Res.*, *25*, 817-828, 1989.

- Shapiro, M., and H. Brenner, Taylor dispersion of chemically reactive species: Irreversible first-order reactions in bulk and on boundaries, *Chem. Eng. Sci.*, *41*, 1417–1433, 1986.
- Shapiro, M., and H. Brenner, Chemically reactive generalized Taylor dispersion phenomena, *AIChE J.*, *33*, 1155–1167, 1987.
- Shapiro, M., and H. Brenner, Dispersion of a chemically reactive solute in a spatially periodic model of a porous medium, *Chem. Eng. Sci.*, *43*, 551–571, 1988.
- Skjetne, E., A. Hansen, and J. S. Gudmundsson, High-velocity flow in a rough fracture, *J. Fluid Mech.*, *383*, 1–28, 1999.
- Small, H., Hydrodynamic chromatography: A technique for size analysis of colloidal particles, *J. Colloid Interface Sci.*, *48*, 147–161, 1974.
- Smith, L., and F. W. Schwartz, Mass transport I: A stochastic analysis of macrodispersion, *Water Resour. Res.*, *16*, 303–313, 1980.
- Smith, P. A., and C. Degueldre, Colloid-facilitated transport of radionuclides through fractured media, *J. Contam. Hydrol.*, *13*, 143–166, 1993.
- Song, L., and M. Elimelech, Transient deposition of colloidal particles in heterogeneous porous media, *J. Colloid Interface Sci.*, *167*, 301–313, 1994.
- Stumm, W., Chemical interaction in particle separation, *Env. Sci. and Technol.*, *11*, 1066–1070, 1977.
- Sudicky, E. A., and E. O. Frind, Contaminant transport in fractured media: Analytical solutions for a system of parallel fractures, *Water Resour. Res.*, *18*, 1634–1642, 1982.
- Sudicky, E. A., and E. O. Frind, Contaminant transport in fractured porous media: Analytical solutions for a two-member decay chain in a single fracture, *Water Resour. Res.*, *20*, 1021–1029, 1984.

- Tang, D. H., E. O. Frind, and E. A. Sudicky, Contaminant transport in fractured porous media: Analytical solution for a single fracture, *Water Resour. Res.*, *17*, 555–564, 1981.
- Taylor, G. I., Dispersion of soluble matter in solvent flowing slowly through a tube, *Proc. R. Soc. London A*, *219*, 186–203, 1953.
- Thompson, A. F. B., Numerical simulation of chemical migration in physically and chemically heterogeneous porous media, *Water Resour. Res.*, *29*, 3709–3726, 1993.
- Thompson, A. F. B., and D. E. Dougherty, Particle–grid methods for reacting flows in porous media with application to Fisher’s equation, *Appl. Math. Mod.*, *16*, 374–383, 1992.
- Thompson, A. F. B., and L. W. Gelhar, Numerical simulation of solute transport in three-dimensional, randomly heterogeneous porous media, *Water Resour. Res.*, *26*, 2541–2562, 1990.
- Thompson, A. F. B., A. L. Schafer, and R. W. Smith, Impact of physical and chemical heterogeneity on cocontaminant transport in a sandy porous medium, *Water Resour. Res.*, *32*, 801–818, 1996.
- Thompson, J. F., F. C. Thames, and C. W. Mastin, Boundary–fitted curvilinear coordinate systems for solution of partial differential equations on fields containing any number of arbitrary two–dimensional bodies, *J. Comput. Phys.*, *24*, 274–298, 1977.
- Toran, L., and A. V. Palumbo, Colloid transport through fractured and unfractured laboratory sand columns, *J. Contam. Hydrol.*, *9*, 289–303, 1992.
- Torok, J., L. P. Buckley, and B. L. Woods, The separation of radionuclide migration by solution and particle transport in soil, *J. Contam. Hydrol.*, *6*, 185–203, 1990.
- Tory, E. M., Stochastic sedimentation and hydrodynamic diffusion, *Chem. Eng. J.*, *80*, 81–89, 2000.
- Tsang, Y. W., and C.-F. Tsang, Channel model of flow through fractured media, *Water Resour. Res.*, *23*, 467–479, 1987.

- Tsang, Y. W., and C.-F. Tsang, A particle-tracking method for advective transport in fractures with diffusion into finite matrix blocks, *Water Resour. Res.*, *37*, 831–835, 2001.
- Uffink, G. J. M., Modeling of solute transport with the random walk method, in *Groundwater Flow and Quality Modeling*, pp. 247–265, 1988.
- Uffink, G. J. M., *Application of Kolmogorov's backward equation in random walk simulations of groundwater contaminant transport*, pp. 283–289, Balkema, Rotterdam, 1989.
- Valocchi, A. J., and H. A. M. Quinodoz, Application of the random walk method to simulate the transport of kinetically adsorbing solutes, in *Groundwater Contamination*, no. 185 in Proceeding of the Symposium held during the Third IAHS Scientific Assembly, pp. 35–42, 1989.
- van de Ven, T. G. M., *Colloidal Hydrodynamics*, Academic Press, London, 1989.
- van der Lee, J., E. Ledoux, and G. de Marsily, Modeling of colloidal uranium transport in a fractured medium, *J. Hydrol.*, *139*, 135–158, 1992.
- van Genuchten, M. T., and W. J. Alves, Analytical solutions of the one-dimensional convective-dispersive solute transport equations, *Technical Bulletin 1661*, U.S. Department of Agriculture, 1982.
- Witherspoon, P. A., J. S. Y. Wang, K. Iwai, and J. E. Gale, Validity of cubic law for fluid flow in a deformable rock fracture, *Water Resour. Res.*, *16*, 1016–1024, 1980.
- Yamashita, R., and H. Kimura, Particle-tracking techniques for nuclide decay chain: Transport in fractured porous media, *J. Nuclear Sci. Technol.*, *27*, 1041–1049, 1990.
- Zimmerman, R. W., and G. S. Bodvarsson, Hydraulic conductivity of rock fractures, *Transp. Porous Media*, *23*, 1–30, 1996.